

UNIVERSITY OF TECHNOLOGY, SYDNEY

**Spectroscopic Studies of
Hydrogen Dopants in
ZnO Crystals**

by

Laurent Olivier LEE CHEONG LEM

A thesis submitted in partial fulfillment for
the degree of Doctor of Philosophy

in the

School of Physics and Advanced Materials
Faculty of Science

2013

Declaration of Authorship

I, Laurent Olivier LEE CHEONG LEM, declare that this thesis titled, ‘Spectroscopic Studies of Hydrogen Dopants in ZnO Crystals’ and the work presented in it are my own. I confirm that:

- This work was done wholly or mainly while in candidature for a research degree at this University.
- Where any part of this thesis has previously been submitted for a degree or any other qualification at this University or any other institution, this has been clearly stated.
- Where I have consulted the published work of others, this is always clearly attributed.
- Where I have quoted from the work of others, the source is always given. With the exception of such quotations, this thesis is entirely my own work.
- I have acknowledged all main sources of help.
- Where the thesis is based on work done by myself jointly with others, I have made clear exactly what was done by others and what I have contributed myself.

Signed:

Date:

Abstract

ZnO is a semiconductor with a direct band gap of 3.37 eV and an exciton binding energy of 60 meV at room temperature. These properties make it an attractive material for optoelectronic devices across a wide range of applications. Significant obstacles preventing the wide scale usage of ZnO include the lack of reliable *p*-type doping and high uncertainty surrounding the nature of its defects. Moreover, as-grown ZnO is intrinsically *n*-type and it is thought that hydrogen is the cause for the high *n*-type character.

The aim of this thesis is therefore to elucidate the role of hydrogen with respect to the optical and electrical properties of ZnO as well as its interaction with native defects and impurities.

During this work, hydrogen was introduced in ZnO single crystals through an RF plasma source. Hydrogen incorporation was confirmed by XPS measurements which showed an increase in hydrogenated oxygen states. Hydrogen also modified the near-surface region of the crystals only and not the bulk.

Hydrogen doped ZnO showed significant increases in the carrier concentration as well as in the near band edge (NBE) luminescence. This is attributed to hydrogen introducing new shallow donors. The green luminescence, whose origin is attributed to V_{Zn} , was quenched after hydrogen incorporation, indicating formation of neutral $V_{Zn}-H_2$ complexes. The yellow luminescence in the as-received crystal is identical to that in Li doped ZnO and was assigned to recombinations involving Li_{Zn} .

Hydrogen doped ZnO also exhibits a negative thermal quenching (NTQ) of the NBE luminescence where the intensity of the luminescence increases with increasing temperature. Q-DLTS measurements detected new electronic states being created following hydrogen incorporation. A model involving the H-related state

at 11 meV releasing electrons to form free excitons is proposed to explain the NTQ behaviour.

XANES studies of H-doped ZnO showed that hydrogen interacted with oxygen states only but not zinc. This suggests that most of the hydrogen dopants introduced by plasma sit at the oxygen anti-bonding site.

The recombination kinetics of the various luminescence was investigated. While the kinetics of the NBE luminescence followed the expected behaviour for excitonic type recombination, the green and yellow luminescences showed high temperature dependencies and is explained in terms of different recombination mechanisms.

Finally, it was found that hydrogen is stable under normal SEM excitation conditions.

Acknowledgements

I would like to thank my supervisors Dr. Cuong Ton-That and Prof. Matthew Phillips for allowing me to work in their research group and for all their support, guidance and help they have offered me during my time as a student at the University of Technology, Sydney.

I would also like to extend my gratitude to Geoff McCredie for his help with the plasma chamber and also the staff of the MAU for their help with sample preparation and data collection, acquisition and analysis.

To Mark Lockrey and Trevor Manning for their help with using and developing the CL system.

To Christian Nenstiel for his help with the PL measurements.

To my fellow research students and colleagues in the MAU for their insightful discussions and ideas and for contributing to a cheerful and pleasant atmosphere. You have made my time at UTS not only successful, but enjoyable.

To my family and friends for their understanding and support during this daunting and important endeavour.

Contents

| | |
|-----------------------------------------------------------------------------|-------------|
| Declaration of Authorship | i |
| Abstract | ii |
| Acknowledgements | iv |
| List of Publications | viii |
| List of Figures | ix |
| List of Tables | xii |
| List of Acronyms | xiii |
| 1 Introduction to Zinc Oxide | 1 |
| 1.1 Zinc Oxide as an Optoelectronic Material | 1 |
| 1.2 Motivation of the Research | 3 |
| 1.3 Aim and Objectives of This Dissertation | 4 |
| 1.4 Thesis Structure | 5 |
| 2 Defects and Hydrogen Impurities in ZnO: A Review of Current Status | 6 |
| 2.1 Physical Properties | 6 |
| 2.2 Crystal Structure | 6 |
| 2.3 Band Structure of ZnO | 8 |
| 2.4 Crystallographic defects | 10 |
| 2.4.1 Vacancies | 11 |
| 2.4.2 Interstitials | 14 |
| 2.4.3 Antisites | 14 |
| 2.4.4 Impurities | 15 |
| 2.4.5 Formation Energies of Native Defects | 15 |

| | | |
|----------|----------------------------------------------------------|-----------|
| 2.5 | Optical Processes in ZnO | 17 |
| 2.5.1 | Exciton Formation | 18 |
| 2.5.2 | Recombination of electron-hole pairs | 20 |
| 2.5.3 | Radiative Recombination | 20 |
| 2.5.3.1 | Near Band Edge Emission | 20 |
| 2.5.3.2 | Deep Level Emission | 22 |
| 2.5.3.3 | Green Luminescence | 23 |
| 2.5.3.4 | Yellow Luminescence | 24 |
| 2.5.3.5 | Red Luminescence | 25 |
| 2.5.3.6 | Summary | 25 |
| 2.5.4 | Non-Radiative Recombination | 26 |
| 2.5.4.1 | Non-Radiative via Deep Level | 26 |
| 2.5.4.2 | Auger Recombination | 26 |
| 2.5.4.3 | Surface Recombination | 27 |
| 2.6 | Hydrogen in ZnO | 27 |
| 2.6.1 | Hydrogen as a Donor | 28 |
| 2.6.2 | Location of Hydrogen in the Lattice | 30 |
| 2.6.3 | Interaction of Hydrogen With Defects | 31 |
| 3 | Experimental Details | 33 |
| 3.1 | ZnO Crystal Specimen | 33 |
| 3.2 | Sample Cleaning and Preparation | 35 |
| 3.3 | Hydrogen Doping | 35 |
| 3.4 | Scanning Electron Microscopy (SEM) | 36 |
| 3.5 | Cathodoluminescence Spectroscopy | 38 |
| 3.5.1 | CL System Calibration | 40 |
| 3.6 | Monte Carlo Simulations (CASINO) | 42 |
| 3.7 | Electrical Measurements | 45 |
| 3.7.1 | Resistivity Measurement | 45 |
| 3.7.2 | Hall Measurement | 46 |
| 3.8 | Synchrotron Light Experiments | 47 |
| 3.8.1 | X-Ray Photoelectron Spectroscopy | 47 |
| 3.8.2 | X-Ray Absorption Near Edge Spectroscopy | 49 |
| 3.9 | Raman Spectroscopy | 50 |
| 3.10 | Charge-based Deep Level Transient Spectroscopy | 52 |
| 3.11 | Other Characterisation Techniques | 54 |
| 4 | Hydrogen Doped ZnO | 55 |
| 4.1 | Introduction | 55 |
| 4.2 | Crystal Morphology and Structure | 56 |
| 4.3 | Electrical Properties of Hydrogen Doped ZnO | 59 |
| 4.4 | Optical Properties of Hydrogen doped ZnO | 60 |

| | | |
|----------|----------------------------------------------------------------|------------|
| 4.4.1 | Effects of Hydrogen on the NBE luminescence | 62 |
| 4.4.2 | Effects of Hydrogen on the DLE | 65 |
| 4.4.3 | Effects of Temperature on Hydrogen Incorporation | 66 |
| 4.4.4 | Deconvolution of the Deep-Level Luminescence Band | 69 |
| 4.4.5 | Depth Distribution of Luminescence Centres | 72 |
| 4.4.5.1 | Simulations of CL Interaction Volumes in ZnO | 73 |
| 4.4.5.2 | Distribution of Luminescence Centres in H-doped ZnO | 75 |
| 4.4.6 | Effect of Plasma Exposure Time on the Luminescence | 78 |
| 4.5 | Raman Spectroscopy | 81 |
| 4.6 | Synchrotron Light Measurements | 85 |
| 4.6.1 | X-Ray Photoelectron Spectroscopy | 85 |
| 4.6.2 | X-Ray Absorption Near Edge Spectroscopy | 92 |
| 4.7 | Summary | 101 |
| 5 | Hydrogen States and Recombination Kinetics in ZnO | 103 |
| 5.1 | Introduction | 103 |
| 5.2 | Temperature Dependence of the Luminescence | 104 |
| 5.3 | Negative Thermal Quenching of the NBE Luminescence | 112 |
| 5.4 | Shallow Carrier Traps in ZnO | 117 |
| 5.5 | Recombination Kinetics | 123 |
| 5.6 | Characteristics of the Yellow Luminescence | 130 |
| 5.7 | Stability of Hydrogen Under the Electron Beam in ZnO | 132 |
| 5.8 | Summary | 140 |
| 6 | Conclusions and Future Directions | 142 |
| 6.1 | Conclusions | 142 |
| 6.2 | Future Directions | 145 |
| 6.3 | Closing Remarks | 146 |
| | Bibliography | 147 |

List of Publications

Refereed Journal Publications

Lee Cheong Lem, L., Ton-That, C., and Phillips, M.R. Distribution of visible luminescence centers in hydrogen-doped ZnO, *Journal of Material Research*, 26(23):2912, 2011.

Oral Presentations

Lee Cheong Lem, L., Ton-That, C., and Phillips, M.R. Investigations of hydrogen dopants in H-doped ZnO.
Australian Microbeam Analysis Society XII, Sydney. February 2013.

Lee Cheong Lem, L., Ton-That, C., and Phillips, M.R. Temperature dependence of cathodoluminescence of hydrogen doped zinc oxide.
ACCM 22 / APMC 10 / ICONN 2012, Perth, February 2012.

Lee Cheong Lem, L., Ton-That, C., and Phillips, M.R. Distribution of green and yellow luminescence centres in H-doped ZnO.
Australian Microbeam Analysis Society XI, Canberra. February 2011.

List of Figures

| | | |
|------|-------------------------------------------------------------------------|----|
| 2.1 | Unit cells for common ZnO structures. | 8 |
| 2.2 | Band structure and splitting of the valence band in ZnO | 9 |
| 2.3 | Point defects in ZnO. | 12 |
| 2.4 | Formation energies of oxygen vacancies | 13 |
| 2.5 | Formation energies of native defects in ZnO. | 17 |
| 2.6 | Typical luminescence spectrum of ZnO | 18 |
| 2.7 | Thermal ionisation of excitons in ZnO and GaN | 19 |
| 2.8 | Radiative recombination channels | 21 |
| 2.9 | The H_i^+/H_i^- transition level for various semiconductors | 28 |
| 2.10 | Formation energies of interstitial hydrogen in ZnO | 29 |
| 2.11 | Model for H_i in ZnO | 30 |
| | | |
| 3.1 | Photograph of ZnO crystal | 34 |
| 3.2 | Plasma Chamber | 36 |
| 3.3 | Schematic diagram showing key parts of a typical SEM. | 37 |
| 3.4 | Processes induced by electron bombardment. | 37 |
| 3.5 | CL setup | 39 |
| 3.6 | CL intensity calibration | 41 |
| 3.7 | CL wavelength calibration | 41 |
| 3.8 | Influence of carrier diffusion on interaction volume | 44 |
| 3.9 | Van der Pauw setup | 45 |
| 3.10 | X-ray photoionisation cross sections | 48 |
| 3.11 | Optical Raman modes in ZnO | 51 |
| 3.12 | Q-DLTS band diagram | 53 |
| 3.13 | DLTS setup | 53 |
| | | |
| 4.1 | X-ray diffraction patterns for ZnO | 57 |
| 4.2 | AFM images of as-received and H-doped ZnO | 58 |
| 4.3 | CL spectrum of as-received ZnO | 60 |
| 4.4 | CL spectrum of as-received ZnO at 10 K | 62 |
| 4.5 | CL comparison after H-doping | 63 |
| 4.6 | PL spectra of as-received and H-doped ZnO | 64 |
| 4.7 | CL on H-doped ZnO performed at different temperatures | 67 |

| | | |
|------|-------------------------------------------------------------------|-----|
| 4.8 | Normalised bound exciton emission | 68 |
| 4.9 | XPS spectrum of Li doped ZnO | 70 |
| 4.10 | Lithium doped ZnO spectrum | 71 |
| 4.11 | Deconvolution of the DLE peak | 72 |
| 4.12 | CASINO simulated electron energy loss curves | 74 |
| 4.13 | CL generation depth | 74 |
| 4.14 | Distribution of luminescence centres | 76 |
| 4.15 | Time dependent CL | 79 |
| 4.16 | Distribution of luminescence centres as a function of plasma time | 80 |
| 4.17 | Raman modes in ZnO | 82 |
| 4.18 | Raman spectra for as-received and H-doped ZnO | 84 |
| 4.19 | XPS survey spectrum of ZnO | 86 |
| 4.20 | Inelastic mean free path of electrons | 89 |
| 4.21 | O 1s XPS spectrum of ZnO at different X-ray photon energies . . | 90 |
| 4.22 | Valence-band photoemission spectra | 92 |
| 4.23 | X-ray attenuation length in ZnO | 93 |
| 4.24 | XANES experimental geometry | 94 |
| 4.25 | O K-edge XANES | 96 |
| 4.26 | Zn L-edge XANES for as-received ZnO | 99 |
| 4.27 | Band structure of ZnO | 100 |
| | | |
| 5.1 | Temperature dependent CL | 105 |
| 5.2 | Energy position of the phonon replica | 107 |
| 5.3 | Temperature dependent of the FX and phonon replica | 108 |
| 5.4 | Temperature dependence FX and bound exciton | 110 |
| 5.5 | Temperature dependence of the NBE peak intensities | 111 |
| 5.6 | Temperature dependence of the DLE | 112 |
| 5.7 | NTQ fits to find activation energies | 115 |
| 5.8 | $I - V$ characteristics of Au Schottky contacts | 117 |
| 5.9 | Q-DLTS spectra of as-received ZnO | 119 |
| 5.10 | Q-DLTS spectra of H-doped ZnO | 120 |
| 5.11 | Temperature dependence of the Y line | 121 |
| 5.12 | Mechanism for the NTQ effect | 122 |
| 5.13 | DLE emission at low and high beam power | 125 |
| 5.14 | Power density plots | 126 |
| 5.15 | CL spectra at 300 K | 128 |
| 5.16 | Temperature dependence of the FWHM of the YL peak | 131 |
| 5.17 | LEEBI spectra on H-doped ZnO | 133 |
| 5.18 | Time resolved irradiation on H-doped ZnO | 134 |
| 5.19 | LEEBI spectra on as-received ZnO | 136 |
| 5.20 | Time resolved irradiation on as-received ZnO | 137 |
| 5.21 | Time resolved irradiation of NBE at 10 K and 300 K | 138 |

| | |
|---------------------------------------------------------|-----|
| 5.22 Time resolved irradiation of DLE at 10 K | 139 |
|---------------------------------------------------------|-----|

List of Tables

| | | |
|-----|--------------------------------------------------------------------|-----|
| 1.1 | Comparison of different optoelectronic materials | 2 |
| 2.1 | Compilation of some physical properties of ZnO. | 7 |
| 2.2 | Summary of bound exciton lines in ZnO at low temperature | 22 |
| 2.3 | Summary of deep level emissions in ZnO | 25 |
| 3.1 | ZnO single crystal substrate supplied by MTI Corporation. | 34 |
| 3.2 | CASINO simulation parameters for depth approximations. | 44 |
| 4.1 | Hall measurements on as-received and H-doped ZnO | 59 |
| 4.2 | Fit parameters for yellow and green luminescences | 71 |
| 4.3 | Assignment of XPS peaks | 87 |
| 4.4 | Summary of XANES peaks | 98 |
| 5.1 | Varshni fit parameters | 109 |
| 5.2 | Coefficients of the excitation density fits | 129 |

List of Acronyms

| | |
|--------|-----------------------------------------------------|
| A^0X | Neutral acceptor bound exciton |
| AFM | Atomic force microscopy |
| ASF | Atomic sensitivity factor |
| | |
| BX | Bound exciton |
| | |
| C-DLTS | Capacitance-based deep level transient spectroscopy |
| CB | Conduction band |
| CCD | Charge-coupled device |
| CVD | Chemical vapour deposition |
| CL | Cathodoluminescence |
| | |
| D^+X | Ionised donor bound exciton |
| D^0X | Neutral donor bound exciton |
| DAP | Donor-acceptor pair |
| DFT | Density functional theory |
| DLE | Deep level emission |
| DLTS | Deep level transient spectroscopy |
| DRCL | Depth-resolved cathodoluminescence |
| | |
| EPR | Electron paramagnetic resonance |
| | |
| FTIR | Fourier transform infrared spectroscopy |
| FWHM | Full width at half maximum |
| FX | Free exciton |
| | |
| IMFP | Inelastic mean free path |
| | |
| LED | Light emitting diode |
| LO | Longitudinal optical |
| LVM | Local vibration mode |
| | |
| NBE | Near band edge |

| | |
|--------|------------------------------------------------|
| PL | Photoluminescence |
| Q-DLTS | Charge based deep level transient spectroscopy |
| sccm | standard cubic centimetres per minute |
| SEM | Scanning electron microscopy |
| SIMS | Secondary ion mass spectrometry |
| TES | Two-electron satellite |
| UV | Ultra-violet |
| UV-Vis | Ultra-violet visible |
| VB | Valence band |
| XANES | X-ray absorption near edge spectroscopy |
| XPS | X-ray photoelectron spectroscopy |
| XRD | X-Ray diffraction |

Chapter 1

Introduction to Zinc Oxide

Zinc oxide (ZnO) has been a subject of research for over five decades owing to its unique properties and possible applications in commercial devices. Its strong ultraviolet (UV) light absorbing, anti-bacterial and anti-fungal properties have led to a variety of applications. ZnO powders have been used as pigments in dyes and paints, or as an active UV absorbing agent in sunscreen to protect against sunburn and other damage to the skin caused by UV light [1, 2]. It is also being used as a source of zinc in dietary supplements.

Recently, there has been an increased interest in ZnO being used as a high efficiency optoelectronic material due to its unique physical and optical properties. Such applications include thin film transistors [3, 4], transparent conducting electrodes and high efficiency light emitting diodes [5, 6] and lasers [7, 8].

1.1 Zinc Oxide as an Optoelectronic Material

ZnO is a direct wide bangap ($E_g = 3.37$ eV at room temperature) and has a high exciton binding energy of 60 meV. Devices based on ZnO could be more efficient than ones based on silicon or gallium compounds and would work at elevated

temperatures. These properties, combined with the ability to engineer the band gap by alloying [9–11], make ZnO an attractive material for the fabrication of efficient light emitting devices.

ZnO has been studied as a semiconductor for decades now with reported research from Fuller [12] dating from 1929 who reported a way to determine lattice parameters [13]. Along with germanium and silicon, ZnO was one of the first semiconductors to be grown with high levels of purity necessary for intensive characterisation measurements. While initially studied for its piezoelectric properties, it is the use of direct wide band gap semiconductors for optoelectronic devices that has generated a renewed interest in ZnO in recent times. Table 1.1 gives a brief overview of optical properties and similarities of ZnO to materials that are currently being used in optoelectronic devices.

Currently, GaN based devices are considered the leading candidates for current and future optoelectronic devices because of the relative ease of achieving both *n* and *p*-type doping. ZnO however has an appealing property over GaN for use in UV LEDs and lasers. The large exciton binding energy of ZnO means that a lower number of excitons will be ionised at room temperature and above which allows for intense excitonic emission. Room temperature lasing has already been observed in ZnO-based structures [7, 14, 15]. Moreover, ZnO has a high quantum efficiency with reports of 85 % being achieved in nanolasers [16].

Table 1.1: Comparison of different optoelectronic materials

| Material | Structure | Lattice constant | | Band Gap (eV at RT) | Exciton Binding Energy (meV) |
|----------|------------|------------------|-------|------------------------|---------------------------------|
| | | a (Å) | c (Å) | | |
| ZnO | Wurtzite | 3.25 | 5.207 | 3.37 | 60 |
| GaN | Wurtzite | 3.19 | 5.185 | 3.39 | 21 |
| ZnS | Wurtzite | 3.82 | 6.261 | 3.80 | 36 |
| ZnSe | Sphalerite | 5.67 | - | 2.7 | 20 |
| GaAs | Sphalerite | 5.65 | - | 1.43 | 4.2 |
| 6H-SiC | Wurtzite | 3.08 | 15.12 | 3.00 | - |

ZnO also has a high level of radiation resistance [17, 18] which lends ZnO to development of space application such as transparent conducting oxides for solar panel uses [19, 20]. Chemical etching, in both acids and alkalis, provides an opportunity for mass production of small ZnO-based devices. The similarities between the lattice parameters and structure of ZnO and GaN also suggest that ZnO can be used as a substrate for high quality epitaxial growth of GaN films. All these properties make ZnO an attractive material for ultra high efficiency light emitting sources.

1.2 Motivation of the Research

Despite all the theoretical advantages of ZnO over currently used optical materials, some fundamental problems still exist. Undoped ZnO is highly *n*-type. The origin of this inherent *n*-type conductivity is still not fully understood. The origin of this *n*-type conductivity has been thought to be from native defects, but recently it is widely believed that accidental incorporation of hydrogen during growth to be the cause of this *n*-type conductivity. Furthermore, achieving stable *p*-type ZnO has not been reported yet.

In addition, the luminescence of ZnO typically consists of two emission regions, one in the UV which is the result of excitonic recombination and one in the visible which is due to recombination involving deep levels. The visible luminescence is undesirable for optical materials and also competes with the excitonic emission.

The origin of the broad yellow-green peak often observed in ZnO is typically attributed to point defects, however the identification of the nature of the defects involved has been subject to considerable debate for the past 60 years.

Understanding the role of hydrogen as a donor in ZnO and its interaction with native defects would give more insights into the intrinsic *n*-type conductivity of

ZnO, the origin of the deep level emission and also the ability to control those luminescence centres.

1.3 Aim and Objectives of This Dissertation

The overall aim of this research project is to elucidate the role of hydrogen as a shallow donor and defect passivator in ZnO. The introduction of hydrogen donors in ZnO will be investigated with respect to changes in the physical, optical, chemical and electronic properties when compared to reference samples.

The key objectives of this research work are summarised below:

- Investigate the effects of hydrogen on the luminescence and electronic properties of ZnO.
- Investigate the origin of the deep level emission, specially the origin of the green luminescence.
- Investigate the interaction of hydrogen with native defects and impurities.
- Investigate the spatial distribution of luminescence centres and defect related emissions in ZnO.
- Investigate possible shallow carrier traps introduced by plasma.
- Investigate the stability of hydrogen in ZnO.

1.4 Thesis Structure

This thesis focuses on the study and analysis of the optical and electronic properties of single crystal ZnO samples. This thesis can be divided into three sections:

- Introduction and background on ZnO - Chapters 1 and 2.
- Experimental details - Chapter 3
- Experimental results - Chapters 4 and 5.
- Conclusions - Chapter 6.

Chapter 1 provides a brief overview in favour of using ZnO for optoelectronic materials and provided the background to place the work in context. Chapter 2 introduces a comprehensive review of the current knowledge and issues surrounding the nature of intrinsic defects and impurities and their effects on the optical properties of ZnO. Chapter 3 describes the various experimental and sample preparation techniques used throughout this work. Chapter 4 focuses on the effects of introducing hydrogen impurities in ZnO, specifically on the optical properties of H-doped ZnO and the chemical state and location of the hydrogen impurities. Chapter 5 examines the temperature dependence of the luminescence of ZnO, the possible creation of shallow carrier traps and the stability of hydrogen in ZnO. Chapter 6 offers a summary of the conclusions and suggestions for future research directions.

Chapter 2

Defects and Hydrogen Impurities in ZnO: A Review of Current Status

This chapter will give an outline of the physical, electronic and optical properties of ZnO. A detailed review of defects and impurities in ZnO as well as their effects on the optical properties will be given.

2.1 Physical Properties

ZnO is a II-VI direct wide bandgap semiconductor. A compilation of physical properties of ZnO is summarised in Table 2.1.

2.2 Crystal Structure

ZnO exists predominantly in the hexagonal wurtzite structure at room temperature and pressure [21]. In this wurtzite structure, zinc ions are tetrahedrally

Table 2.1: Compilation of some physical properties of ZnO.

| Physical Properties | Value |
|-------------------------------------|--------------------------------------------------------------------------------------------------------|
| Lattice constant | |
| a | 3.2496 Å |
| c | 5.2065 Å |
| Molar mass | 81.408 g/mol |
| Density | 5.606 g/cm ⁻³ |
| Melting point | 1975 °C (decomposes) |
| Energy gap | 3.37 eV (at 300 K) |
| Exciton binding energy | 60 meV |
| Intrinsic carrier concentration | <10 ⁶ cm ⁻³ (max n-type doping >10 ²⁰ cm ⁻³) electrons |
| Electron effective mass | $m_e^* = 0.24 m_e$ |
| Hole effective mass | $m_h^* = 0.59 m_e$ |
| Hall mobility of electrons at 300 K | 200 cm ² /V s |

co-ordinated to four oxygen ions as shown in Figure 2.1 (a). The wurzite structure actually consists of successive planes composed of tetrahedrally coordinated Zn²⁺ and O²⁻ ions stacked along the c -axis. In this wurzite structure, the unit cell has a lattice constant of $a = 3.296$ Å and $c = 5.207$ Å [22]. In addition to the wurzite structure, ZnO can also exist in two other crystallographic structures, the cubic zinblende or rocksalt structures (see Figure 2.1).

There are four surfaces of interest in ZnO, the nonpolar m (10 $\bar{1}$ 0), the semipolar a (11 $\bar{2}$ 0), and the polar (0001)-Zn and (000 $\bar{1}$)-O surfaces. These polar surfaces result in spontaneous polarisation along the c -axis and lead to the piezoelectric properties of ZnO. Surface reconstruction or faceting to stabilise polar surfaces has not been reported in ZnO. Instead the polar c surfaces are atomically flat and stable surfaces without any reconstruction [23]. Surface reconstruction will imply breaking of Zn-O bonds and rearrangement of ions on the surface, which is energetically unfavourable due to the strong Zn-O bond energy [24].

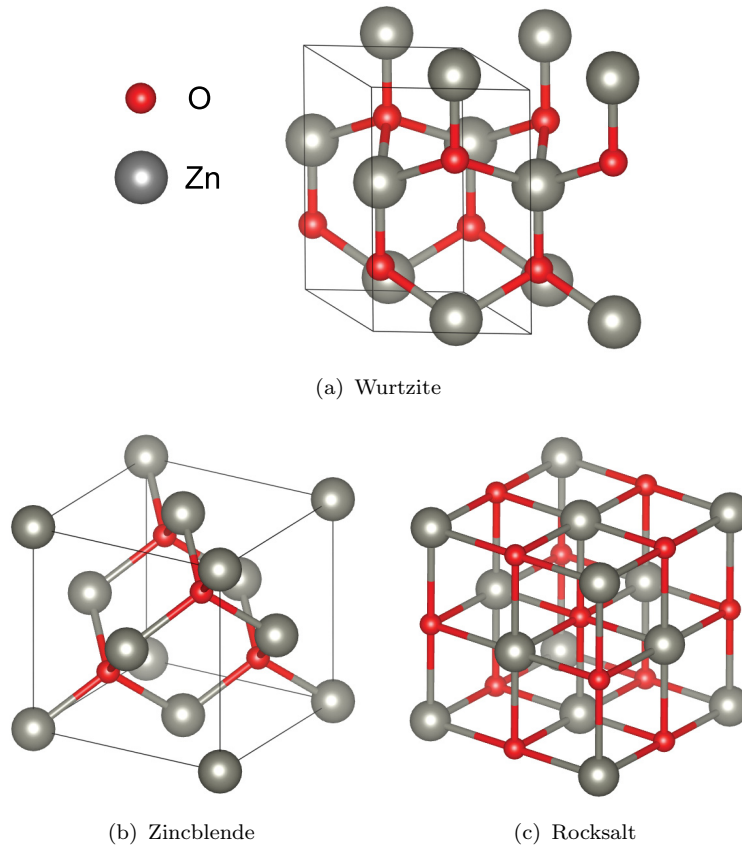


Figure 2.1: Unit cells for common ZnO structures. Grey spheres represent zinc atoms while red spheres represent oxygen atoms. The wurtzite and zincblende structure are both terminated by the Zn-0001 face.

2.3 Band Structure of ZnO

ZnO is a wide band-gap semiconductor ($E_g \approx 3.37$ eV with a high exciton binding energy of $E_b = 60$ meV). As a direct semiconductor, its highest valence and lowest conduction band are both located at the Γ -point of the Brillouin zone as shown in Figure 2.2(a). The conduction band is s-like two-fold degenerated and comprises of the empty zinc 4s orbital. The valence band is p-like caused by the fully occupied oxygen 2p orbitals in ZnO [25]. Its 6-fold degeneracy is lifted due to spin-orbit interaction and due to the crystal field splitting caused by the anisotropy of the wurtzite structure. Three topmost valence bands are observed. The assignment of the symmetries to these three bands is still under discussion

in literature, but the valence band order $\Gamma_7\text{--}\Gamma_9\text{--}\Gamma_7$ corresponding to a negative Δ_{so} has recently become widely accepted [26]. Regardless of the actual valence band order, the bands are labelled A, B and C with increasing distance to the conduction band as shown in Figure 2.2(b). This denomination is also used for the excitons related to these bands. The energetic differences are $\Delta_{AB} = 4.9$ meV and $\Delta_{BC} = 43.7$ meV [27].

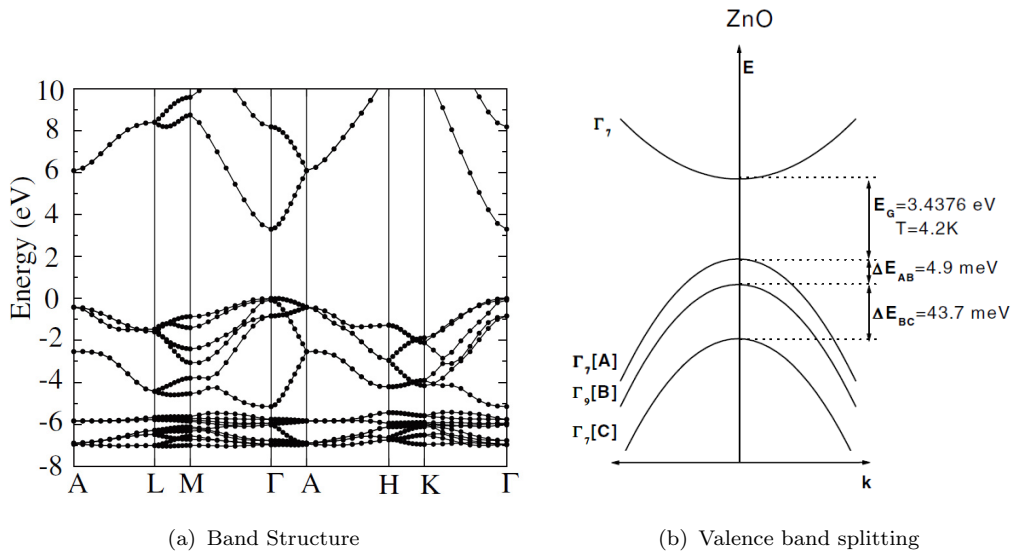


Figure 2.2: Calculated band structure of ZnO using the HSE hybrid functional in (a) (taken from [28]). Splitting of the valence band into the A, B, and C sub-bands caused by the combined effects of crystal-field splitting and spin-orbit coupling in (b) (taken from [27]).

The temperature dependence of the bandgap can be described up to room temperature by the Varshni model [29]:

$$E_g(T) = E_g(0) - \frac{\alpha T^2}{T + \beta} \quad (2.1)$$

where $E_g(T)$ is the energy gap at temperature T , $E_g(0)$ is the energy gap at 0 K, α and β are empirically measured constants with values of 5×10^{-4} eV/K and 900 K respectively [30].

2.4 Crystallographic defects

Crystalline solids, like ZnO, are prone to a variety of defects or imperfections in the crystal's lattice. These defects are of importance because they can affect the material's properties significantly. Defects in materials can be grouped in the following categories:

Bulk defects

Bulk defects occur as voids in the crystal lattice where a cluster of atoms are missing. Bulk defects can also manifest in the form of impurities clustering together to form regions of different phase.

Planar defects

Planar defects can appear in many forms. Grain boundaries which occur when the crystallographic direction of the lattice abruptly changes. This is common in crystal growth when two crystals which grow initially separately then meet, forming an interface between the two crystallites. Stacking faults are considered as planar defects. These occur if the stacking pattern of a closed pack structure is interrupted. Considering the stacking sequence ABCABCABC being interrupted by one or two layers, this is known as a stacking fault (ABCABABCAB).

Line defects

There are two types of line defects, edge dislocation and screw dislocation. Dislocations combining both edge and screw dislocations are also common. An edge dislocation occurs when one plane of atoms terminates in the middle of a crystal. This causes the adjacent planes to not be straight, but instead bend around the edge of the terminating plane. This happens to preserve the ordering of crystal planes on both sides of the terminating plane. Screw dislocations are similar, but a helical path is created instead of an edge. Dislocations often result in lattice distortions. The direction and

magnitude of such distortion is expressed in terms of a Burgers vector. For an edge dislocation, the Burgers vector is perpendicular to the dislocation line, whereas in the case of the screw dislocation it is parallel. Dislocations can move if the atoms from one of the surrounding planes break their bonds and rebond with the atoms at the terminating edge. This leads to the malleability of materials.

Point defects

Point defects are defects that occur at only one or around one lattice point.

Common point defects are:

- Vacancy

The absence of atom A at its designated position in the lattice, V_A . e.g. zinc vacancy - V_{Zn} . Figure 2.3 (a).

- Interstitial

An atom A located between lattice sites, A_i e.g. zinc interstitial Zn_i . Figure 2.3 (b).

- Antisite

An atom A being on the lattice spot of atom B, and both A and B belong to the host material, e.g. O_{Zn} or Zn_O . Figure 2.3 (c).

- Substitutional

An external atom C being in the lattice site of another host atom, e.g. Li_{Zn} . Figure 2.3 (d).

Point defects are important in semiconductors because they are often identified as being the cause of various electronic and optical properties.

2.4.1 Vacancies

Vacancies in ZnO, such as zinc (V_{Zn}) or oxygen (V_O) vacancies, are sites in the lattice which are usually occupied by an atom, but which is left empty. Vacancies

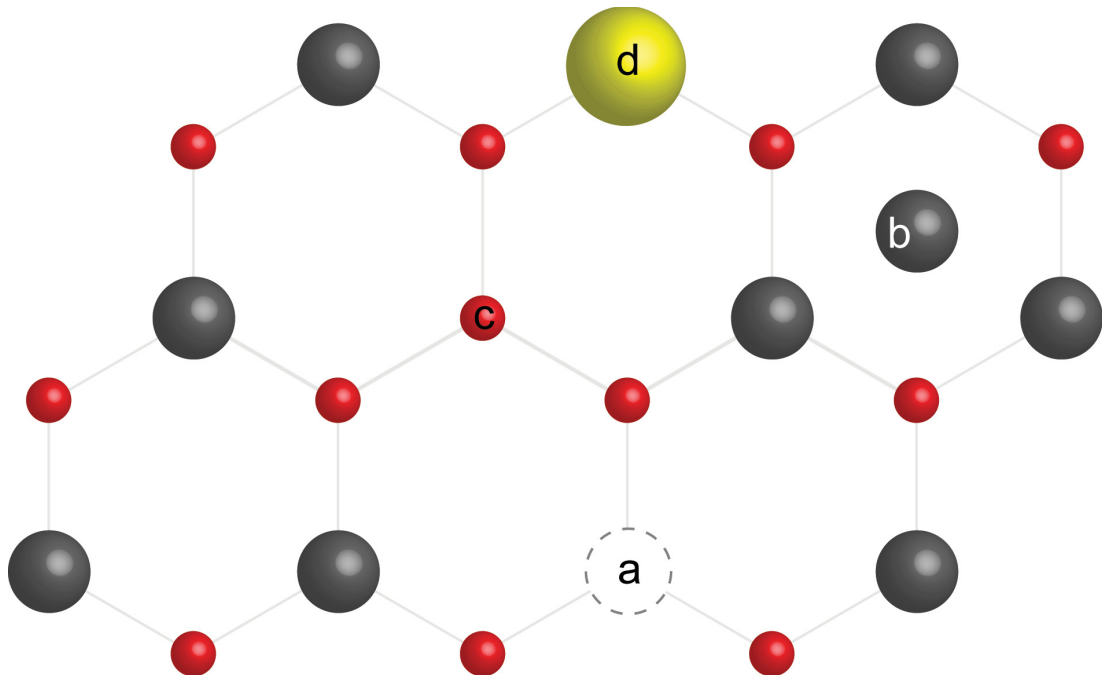


Figure 2.3: Example of point defects in ZnO where grey spheres are zinc atoms and red spheres are oxygen atoms. (a) a zinc vacancy V_{Zn} , (b) a zinc interstitial Zn_i , (c) an oxygen antisite O_{Zn} , (d) a substitutional impurity at a zinc site e.g. Li_{Zn} .

can propagate through the lattice when neighbouring atoms move to fill the vacancy. The stability of the surrounding crystal structure ensures the vacancy does not collapse.

In ZnO, first-principle calculations have consistently shown that V_O is a deep defect donor, where the $1+$ charge state is thermodynamically unstable [31]. The formation energy of V_O^+ is calculated to be higher than that of V_O^0 and V_O^{2+} for all values of the Fermi level as shown in Figure 2.4. Evidence of this “negative U” behaviour of V_O^+ has been reported experimentally by Pfisterer et al. through DLTS experiments [32]. The stable charge state of the vacancy depends on the position of the Fermi energy level in the band gap. The vacancy is found in the $+2$ charge state if the Fermi level is below the $0/2+$ transition level or is in the neutral charge state if the Fermi level is above the $0/2+$ transition level. First principle calculations place this $0/2+$ transition level to be around $0.5-0.8\text{eV}$ above the valence band maximum [33, 34]. Calculations that allow band gap estimation

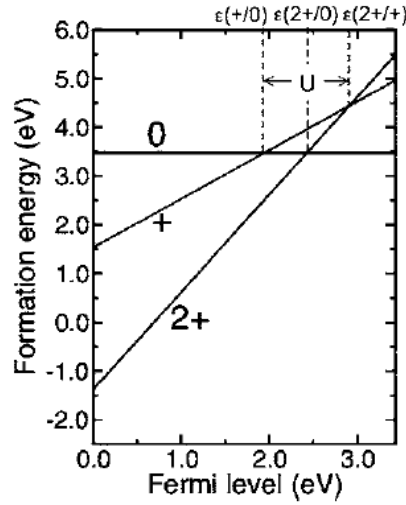


Figure 2.4: Formation energies of oxygen vacancies in the 0, 1+ and 2+ charge states under zinc rich conditions. The formation energy of the 1+ charge state is always highest irrespective of Fermi level, indicating that the 1+ state is thermodynamically not favoured. Taken from [31]

error of local density approximation have estimated the 0/2+ transition level to be 1-2 eV below the conduction band minimum [35–37]. Calculations disagree on whether V_O should be formed in *n*-type ZnO, with Lany and Zunger claiming defect concentration of 10^{17} cm^{-3} [38] while Janotti and Van de Walle predict the formation energy of V_O to be too high for significant defect concentration to be present at equilibrium conditions even in zinc rich conditions [39]. V_O has commonly been attributed as the source of the ubiquitous green luminescence band centred around 2.4-2.5 eV (approximately 510 nm) [31, 40, 41] due to an excited-to-ground state transition [42].

A zinc vacancy, V_{Zn} , is a double acceptor with first principle calculations placing the 0/1- and 1-/2- transition levels at respectively 0.1-0.2 and 0.9-1.2 eV above the valence band maximum [39, 43, 44]. Janotti and Van de Walle [37] propose that the transition from a shallow donor level to the 1-/2- acceptor level associated with V_{Zn} could result in luminescence around 2.5 eV. Their suggestion is supported by the observation that hydrogen plasma treated ZnO samples

show a reduced green luminescence intensity, consistent with V_{Zn} passivation by hydrogen [45].

2.4.2 Interstitials

Interstitial defects occur when an atom occupies a site in the crystal structure at which an atom would not usually be found. In ZnO, zinc interstitials (Zn_i) are shallow donors that have a high formation energy in *n*-type ZnO [39]. They also have a migration barrier that can be as low as 0.57 eV, resulting in instability and high mobility at room temperatures [35]. Being mobile, Zn_i can form complexes with impurities such as nitrogen and exist as stable shallow donors [46]. The formation of Zn_i is favoured in *p*-type conditions so this defect is another source of charge compensation in *p*-type doping [47].

Oxygen interstitials (O_i) can occupy the octahedral or tetrahedral interstitial sites or form split interstitials [48]. The octahedral position is unstable and spontaneously relaxes into a split-interstitial configuration in which O_i shares a lattice site with one of the nearest oxygen atoms [39]. Oxygen interstitials occupying the octahedral sites are electrically active and introduce levels in the band gap that can accept two electrons. Transition levels for the 0/1- and 1-/2- charge states are at 0.72 and 1.59 eV above the valence band maximum from first principle calculations [39].

2.4.3 Antisites

Oxygen (O_{Zn}) and zinc (Zn_{O}) antisites have high formation energies under all conditions and are unlikely to form in significant concentrations. Zn_{O} is a double donor with transitions located within the conduction band. O_{Zn} on the other hand forms deep acceptors with the 0/1- and 1-/2- transition levels at 1.53 eV and 1.77 eV above the valence band maximum [39].

2.4.4 Impurities

Impurities are elements introduced in the lattice which are not atoms of the host material. Impurities occur as either a substitutional or an interstitial defect. These impurities can sometimes have different charges compared to the host atoms and a charge compensation mechanism occurs to keep the overall charge of the crystal neutral.

Unintentional doping can change the properties of the material by creating donor or acceptor levels in the band gap of the material. Meyer et al. summarised some of those defects and the energy levels they create in the band gap [27]. The additional photoluminescence peaks found at liquid helium temperature were associated to excitons bound to impurities such as hydrogen, gallium, indium and aluminium (See Table 2.2). The broad visible luminescence centered around 2.4 eV is often attributed to copper impurities which show a distinct fine structure in the luminescence [49]. The yellow-orange luminescence centered at 2.1 eV has been attributed to excitons bound to lithium impurities at a zinc substitutional site [50].

2.4.5 Formation Energies of Native Defects

Understanding the formation energies and processes for defects allows us to make predictions about the concentration of such defects during growth and processing. Kohan et al. [43] and Van de Walle [51] have used first principle calculations to determine the formation energies and electronic structure of the native point defects in ZnO. In their work, the concentration of a defect within a crystalline structure depends upon its formation energy (E_f) as shown in Equation 2.2, where N_{sites} represents the concentration of crystal sites where the defect can occur. The lower the formation energy of a particular defect, the higher its

equilibrium concentration.

$$c = N_{sites} \exp\left(-\frac{E^f}{k_B T}\right) \quad (2.2)$$

The formation energy of a point defect in a given charge state (q) is given by Equation 2.3 where $E^{tot}(q)$ represents the total energy loss of a system consisting of N_{Zn} and N_O , which represent the number of zinc and oxygen atoms respectively, μ_{Zn} and μ_O are the chemical potentials for zinc and oxygen, and E_F is the Fermi energy.

$$E^f(q) = E^{tot}(q) - N_{Zn}\mu_{Zn} - N_O\mu_O + qE_F \quad (2.3)$$

The chemical potentials for this relationship rely on the environment conditions during growth. Under zinc rich and oxygen rich growth conditions, it is possible to assign bulk chemical potentials to the system ($\mu_O = \mu_{O(bulk)}$ and $\mu_{Zn} = \mu_{Zn(bulk)}$). For intermediate ratios where the system is not particularly zinc or oxygen rich, $\mu_O < \mu_{O(bulk)}$ and $\mu_{Zn} < \mu_{Zn(bulk)}$, however the chemical potentials for both zinc and oxygen are in equilibrium with ZnO: $\mu_{Zn} + \mu_O < \mu_{ZnO}$.

Native point defects in materials are responsible for the intrinsic electronic and optical properties. Point defects are most commonly investigated because several intrinsic defects have low formation energies and tend to form readily during growth processes. Native defects tend to occur as deep level defects; V_O being a deep donor and V_{Zn} being a deep acceptor. Figure 2.5 represents a way to visualise the location of defects and the probability of them occurring. The formation energies and charge transition levels were obtained from first principle calculations [39].

The stable charge state of the defect is dependent on the position of the Fermi level as well as the growth conditions. Donor type defects growth will be favoured in zinc rich environments while acceptor type defects will be favoured in oxygen rich growth environments. Undoped ZnO is normally grown in zinc rich environments which favour the formation of donors [46].

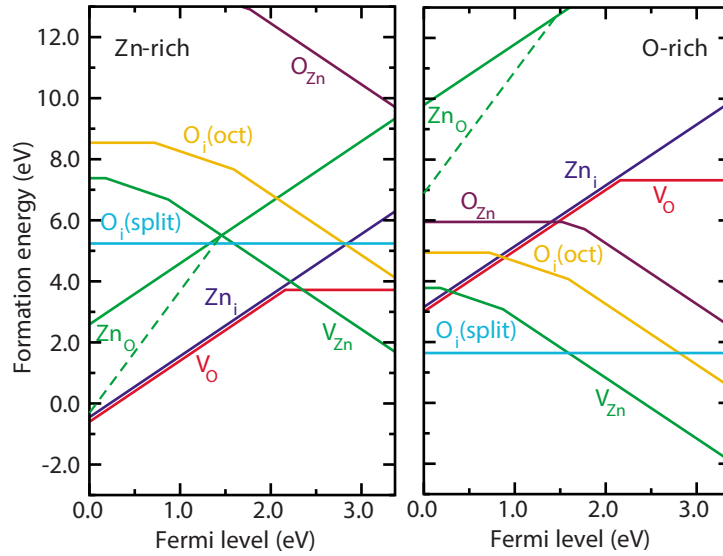


Figure 2.5: Formation energies of native defects in ZnO in zinc and oxygen rich environments based on LDA and LDA+U calculations. Slope changes show charge transition levels. From Janotti and Van de Walle [39]

2.5 Optical Processes in ZnO

Luminescence is the term used to describe radiative emission from a material following excitation from external energy sources. Luminescence properties in materials are useful because they give information about defects and defect levels. Luminescence techniques are usually non-destructive. While there are a variety of luminescence mechanism, it is worth focusing on two for ZnO. Photoluminescence (PL) and cathodoluminescence (CL), which differ in the form of excitation. PL uses photons while CL uses electrons.

Zinc oxide has a characteristic emission spectra comprising of two main peaks: the NBE emission at 3.3 eV and the broad defect related band occurring at 2.4 eV as shown in Figure 2.6. The NBE is dominated by FX and D⁰X emission, along with LO phonon replicas while the green DLE is attributed usually to native defect or impurity related recombination mechanisms.

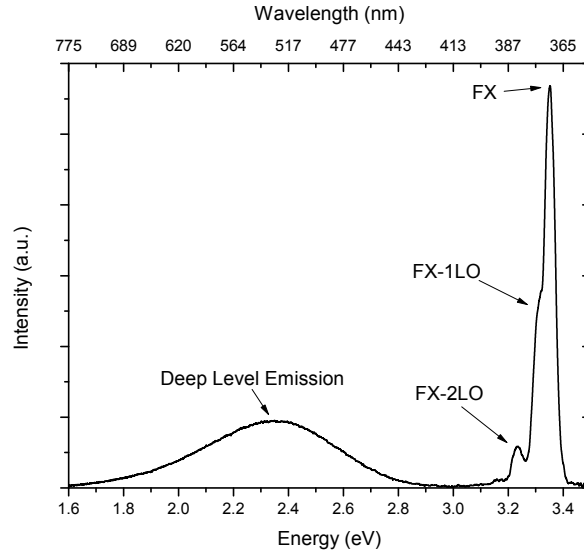


Figure 2.6: Typical luminescence spectrum of ZnO at 80 K showing the free exciton peak (FX), the first and second phonon replica of FX (FX-1LO and FX-2LO) and the broad deep level emission.

2.5.1 Exciton Formation

When an electron is excited from the valence band to the conduction band, it leaves behind a hole. The electron and hole can interact to form a quasiparticle called the exciton. This exciton can then travel through the lattice without net charge disruption. The excited electron and hole are attracted through electrostatic Coulomb forces, this attractive force is defined as the binding energy (E_X) of the exciton. The binding energy of an exciton exhibits hydrogen like quantised states (defined by the quantum number n) and is given by [52]:

$$E_X = \frac{m_r^* e^4}{2\hbar^2 \epsilon^2 n^2} \quad (2.4)$$

where m_r^* is the reduced mass of the electron-hole pair, e is the elementary charge, \hbar is the reduced Planck's constant and ϵ is the dielectric constant.

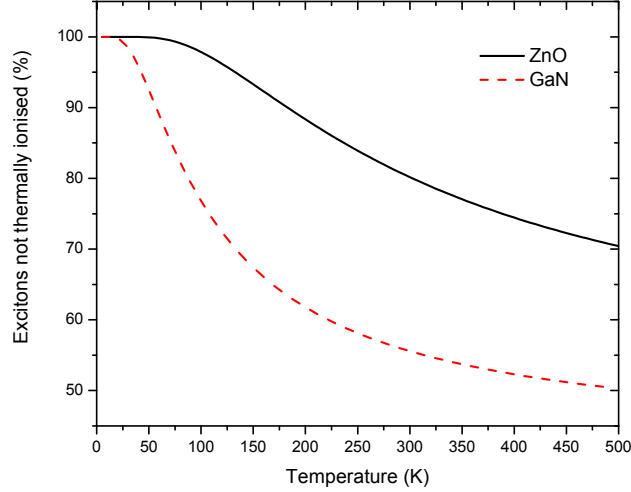


Figure 2.7: Thermal ionisation of excitons in ZnO and GaN as a function of temperature from Equation 2.5. At room temperature, 80% of excitons formed are still bound in ZnO compared to 55% in GaN.

The number of exciton formed is dependent on the exciton binding energy, E_X , in the material and the temperature according to the Saha equation [53]:

$$\frac{n_{eh}^2}{n_X} = \frac{k_B T}{2\pi \hbar^2} \mu e^{-E_X/k_B T} \quad (2.5)$$

where n_X is the number of excitons, n_{eh} is the number of free carriers and μ is the reduced effective mass of the electron-hole pair.

Comparing ZnO to GaN, with exciton binding energies of 60 meV and 21 meV respectively, ZnO would have a substantially higher percentage of exciton at room temperature and above as shown in Figure 2.7. The switch to ZnO based devices from those using GaN would lead to higher emission efficiency.

The excitons created in ZnO correspond to the three levels of the valence band which is split under crystal field and spin-orbit effects [54]. The excitons corresponding to each level are thus identified as A-, B- and C-excitons in order of increasing energy gap. The A- and B-excitons are polarised perpendicular to the c-axis while the C-exciton is polarised parallel to the c-axis [55, 56]. The A- and

B-excitons are separated by 4.9 meV while the B- and C-exciton separation is 43.7 meV (See Section 2.2).

2.5.2 Recombination of electron-hole pairs

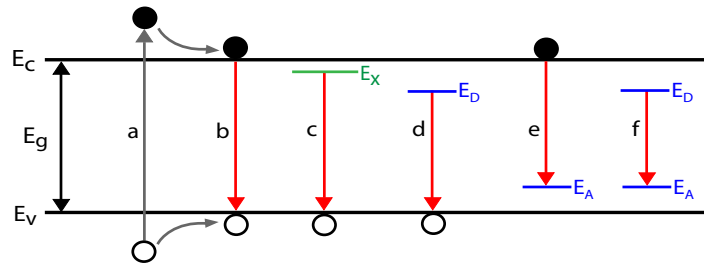
In semiconductors there are two types of transitions involving electron-hole pairs recombination. Radiative recombination during which the electron-hole pair recombines and the energy is emitted by a single photon. Non-radiative recombination is also possible during which photons are not emitted but the energy is dissipated through quantised lattice vibrations known as phonons.

2.5.3 Radiative Recombination

When an electron is excited from the valence band, it leaves behind a hole. The electron-hole pair can then recombine radiatively in a number of ways as shown in Figure 2.8. Once an exciton has formed, it can propagate through the crystal where it can potentially be trapped by a defect at low temperatures or scattered by phonons, typically LO phonons. Radiative emission from excitons in ZnO will only reach the surface of the material if it recombines near the surface due to self absorption effects.

2.5.3.1 Near Band Edge Emission

The Near Band Edge (NBE) emission in ZnO is radiation emitted in the UV region. Band to band recombination occurs when a free electron drops from its excited state in the conduction band to fill an empty free hole state in the valence band. This results in emission of a photon with an energy equal to that of the band gap (Figure 2.8 a).



| Recombination channel | Notation | Energy of transition |
|-----------------------|---------------------------|----------------------------------------------------------------------------|
| a | Excitation | |
| b | Band to band | E_g |
| c | Bound and free exciton | $[D^0X], [A^0X], [FX]$ $E_g - E_X$ |
| d | Donor to free hole | $[D^0, h]$ $E_g - E_D$ |
| e | Free electron to acceptor | $[e, A^0]$ $E_g - E_A$ |
| f | Donor-acceptor pair | $[D^0, A^0]$ $E_g - E_D - E_A + \frac{q^2}{4\pi\epsilon_0\epsilon_r r}$ |

Figure 2.8: Schematic diagram of the radiative recombination channels possible as a result of an excitation of an electron-hole pair along with the energy of the transition.

While band to band transitions are the simplest recombination mechanism for an electron hole pair, they are not necessarily the preferential method resulting in radiative emission. As seen in Figure 2.8, the recombination energy gap can be reduced by the Coulombic force arising between an electron-hole pair in an exciton. This can be further reduced through donor or acceptor bound excitons, reducing the emitted energy from the recombination noticeably. This reduction in the emission energy gives rise to the NBE peaks observed in opto-electronic materials such as ZnO.

At liquid helium temperatures, it is possible to separate the narrow NBE band into individual components, allowing for identification of different impurities and bound defects. The most prominent lines are labeled as I lines, with I_n where $n = 0, 1, 2, \dots$ in order of decreasing energy, following the notation used in early work on the subject [57]. As the temperature increases, these peaks broaden and merge, until at room temperature the NBE peak typically only exists as a single

Table 2.2: Summary of bound exciton lines in ZnO at low temperature

| Line | Photon energy (eV) | Identified impurity |
|----------|--------------------|---------------------|
| F^X | 3.3767 | - |
| I_0 | 3.3724 | Al |
| I_1 | 3.3711 | Ga |
| I_{1a} | 3.3691 | - |
| I_2 | 3.3677 | Li, Na |
| I_3 | 3.3664 | - |
| I_{3a} | 3.3654 | Zn_i |
| I_4 | 3.3629 | H |
| I_5 | 3.3614 | - |
| I_6 | 3.3605 | Al |
| I_{6a} | 3.3604 | - |
| I_7 | 3.3600 | - |
| I_8 | 3.3597 | Ga |
| I_{8a} | 3.3593 | - |
| I_9 | 3.3564 | In |
| I_{10} | 3.3530 | - |
| I_{11} | 3.3483 | - |

Adapted from Meyer et al. [27]

broad emission centred at an energy just below the fundamental band gap. This is also influenced by the thermal ionisation of the various bound excitons.

There is a considerable amount of controversy regarding the assignment of the I lines as found in Table 2.2 to various donor or acceptor bound excitons. There is general consensus, however, that I_3 - I_8 are due to D^0X , while I_9 - I_{11} have been suggested as either due to D^0X [27] or A^0X [58]. The I_0 - I_2 lines have been attributed to D^0X [58, 59] or excitons bound to ionised donors [27]. The study of bound excitonic luminescence provides information regarding the identity of the impurities, as well as their relative concentrations, in a given ZnO sample.

2.5.3.2 Deep Level Emission

The emission spectra of ZnO crystals in the visible range is dominated by a broad luminescence band between 2.9 eV (427 nm) and 1.5 eV (828 nm) with a maximum

around 2.35 eV (527 nm). A variety of models have been proposed to explain the deep level emission from ZnO. This luminescence is found in the visible range with green, yellow and red luminescences being reported. It is widely accepted that the emission occurs as the result of either native defects or unintentional impurities, with point defects such as V_O , V_{Zn} , or Zn_i , along with Cu interstitials or Li on a substitutional Zn site being investigated thoroughly. However, there is still no conclusive result to identify the origin of the emission.

2.5.3.3 Green Luminescence

The green luminescence in ZnO was first reported in 1938 by Ewles [60]. Early studies explicitly attributed the broad green peak to copper impurities [49], however more recent evidence has suggested the defect was more likely to be related to intrinsic defects such as V_O or V_{Zn} . Both defect mechanisms offer plausible arguments, and it has been further proposed that there are two nearly similar, but fundamentally different, emission characteristics in this region of the spectrum as a result of both defect models. Experimental evidence shows that copper impurities tend to result in a fine structure within photoluminescence spectra at liquid helium temperatures. The transition from (Cu^+, h) to the $Cu^{2+} T_2$ state results in a photon with the zero-phonon line of the emission at 2.86 eV [61]. Phonon replicas of this peak, separated by 72 meV (consistent with the longitudinal-optical phonon mode in ZnO), are responsible for the fine structure of the band centered at 2.4 eV. In the case of native point defects (V_O or V_{Zn}) the emission is a structureless band at the same position with a similar width.

Kohan et al. [43] have calculated the defect formation energy for a variety of native point defects in ZnO as a function of the Fermi level. Their work concluded that the two most common defects in ZnO are likely to be vacancies of oxygen or zinc. The oxygen vacancies have lower formation energy than zinc interstitials,

and so are more likely to form in zinc rich growth conditions, while oxygen rich conditions should yield zinc vacancies.

Other work from Vanheusden et al. has also shown correlations between the concentrations of free electrons and V_O defects with the intensity of the green band through EPR measurements [40, 62]. Through annealing experiments under both oxidizing and reducing environments, strong evidence was provided supporting V_O as the mechanism supporting the origin of the green defect band. This interpretation of the results has come under scrutiny however as the electron paramagnetic resonance signal ($g=1.96$) used by Vanheusden to identify the oxygen vacancies was in fact subsequently found to be related to an isotropic shallow donor level [63].

More recently, both theoretical and experimental work have been attributing the structureless green luminescence to native zinc vacancies. V_{Zn} has a low formation energy and hence its concentration in undoped ZnO is expected to be significant. Calculations also place the $-1/-2$ transition level of V_{Zn} at ≈ 0.9 eV above the valence band maximum [39, 43, 64]. A transition involving a free electron in the conduction band or an electron at a shallow donor to a hole bound to the singly ionised V_{Zn}^- would lead to emission of a photon with an energy of 2.4 eV, consistent with the green luminescence. An increase in the intensity of the green luminescence was observed after ZnO was annealed in an oxidising atmosphere [65]. This is again consistent with the formation of V_{Zn} .

2.5.3.4 Yellow Luminescence

In addition to the green luminescence at 2.4 eV, ZnO also exhibits a yellow luminescence centered at 2.1-2.2 eV. This yellow luminescence has been observed in PL studies of nominally undoped ZnO and has been attributed to excess oxygen in the samples [66], specifically oxygen interstitials (O_i) during hydrothermal growth processes [67–69]. Other work has attributed the yellow luminescence to

lithium impurities [50, 70]. Lithium in the form of LiOH is used as a mineraliser during hydrothermal growth of ZnO crystals [71–74]. Lithium occupies a zinc site (Li_{Zn}), forming a deep acceptor level 0.8 eV above the valence band maximum [75]. It is believed that the yellow luminescence is due to a donor-acceptor pair type transition from a shallow donor to the Li_{Zn} acceptor [76]. All hydrothermally grown ZnO is expected to exhibit this yellow luminescence owing to the use of LiOH to dissolve the precursors.

2.5.3.5 Red Luminescence

The red luminescence in ZnO is often associated to excess zinc due its appearance after annealing ZnO in zinc vapour at 1100°C [77–79]. It has also been reported that the red luminescence appears after annealing in atmospheres containing phosphorous, titanium, iron, nickel or cobalt [79–82]. Recent work shows that hydrogen may be involved in the red luminescence. Annealing in zinc vapour in the presence of hydrogen leads to the appearance of the red luminescence, which is reversible with removal of hydrogen [83]. This suggests that the red luminescence is a consequence of the interaction between oxygen vacancies and hydrogen.

2.5.3.6 Summary

The reported origin of the deep level emission are summarised in Table 2.3.

Table 2.3: Summary of deep level emissions in ZnO and frequent assignments of its origin

| Emission | Peak Energy (eV) | Origin |
|----------|------------------|--------------------------------------------------------------------|
| Green | 2.4 - 2.6 | $\text{V}_{\text{Zn}}, \text{V}_{\text{O}}, \text{Cu}_{\text{Zn}}$ |
| Yellow | 2.0 - 2.1 | $\text{Li}_{\text{Zn}}, \text{O}_{\text{i}}$ |
| Red | 1.7 - 1.9 | $\text{V}_{\text{O-H}}, \text{TM}_{\text{Zn}}$ |

2.5.4 Non-Radiative Recombination

After an electron is excited from the valence band to higher energy levels, the electron can then return to its ground state emitting the excess energy. The excess energy not emitted in the form of photons is called non-radiative recombination. There are three main physical methods with which non-radiative recombination can occur: non-radiative via deep level, Auger recombination and surface recombination. Due to a high degree of coupling to lattice vibrations non-radiative recombination processes are typically thermally activated and can dominate carrier relaxation at elevated temperatures.

2.5.4.1 Non-Radiative via Deep Level

Defects in the crystal structure are the most common cause resulting in non-radiative recombination. Point defects such as impurities, vacancies, interstitials and antisites introduce new energy levels in the band gap of semiconductors and can alter the electronic properties of a semiconductor. These energy levels can act as efficient recombination centres. These levels are often referred to as traps or luminescence killers owing to their promotion of the non-radiative processes. Rather than releasing the energy gained through the recombination of the electron hole pair in the form of light, these defects instead can produce quantised vibrational quasiparticles known as phonons. These phonons vibrate through the lattice, dispersing the released energy as heat to the material and surrounding environment.

2.5.4.2 Auger Recombination

Energy from the recombination can be given to a third carrier which is then excited to a higher energy level without shifting to another energy band. This third carrier then normally loses the excess energy to thermal vibrations in the

semiconductor. Owing to the need to have a third particle present, Auger recombination is significant only in conditions where the carrier density is very high. The generation process itself is not easily produced as the third particle would have to start in the unstable high-energy state.

2.5.4.3 Surface Recombination

A surface is a disruption in the periodicity of the crystal lattice which can then lead to a change in the band structure at the surface of semiconductors when compared to the bulk band structure. Atoms at the surface do not have the same bonding structure as bulk atoms due to the absence of neighbouring atoms. The surface atoms normally have dangling bonds due to partially unfilled electron orbitals. It is these dangling bonds that can act as non-radiative centres producing phonons rather than photons. It is also however possible to passivate the surface effects of semiconductors through methods such as shallow doping or growth of a capping layer on top of the surface.

2.6 Hydrogen in ZnO

Studying the effects of hydrogen in ZnO is important because hydrogen is present in nearly all crystal growth methods. Hydrogen is present in the form of water in hydrothermal growth methods and as residual water vapour in CVD chambers. Hydrogen being a small element and being mobile can easily be incorporated into the ZnO lattice during growth [84, 85]. It has been suggested that hydrogen donors unintentionally incorporated during growth could be the cause of the strong *n*-type behaviour of ZnO [86–88]. Several post-growth methods of introducing hydrogen in ZnO have been reported with the most popular ones being annealing in a hydrogen atmosphere [89, 90], implantation [91, 92] and exposure to a hydrogen plasma [45, 85, 93].

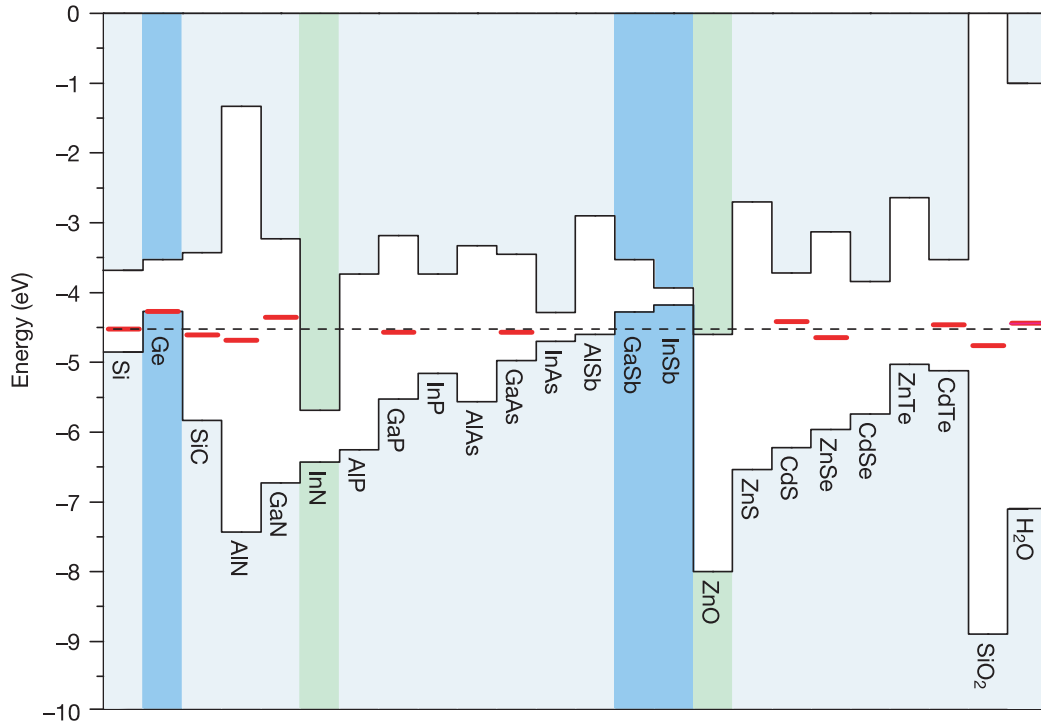


Figure 2.9: The H_i^+/H_i^- electronic transition level in various semiconductors. H_i acts as an acceptor if E_F is above E_t or as a donor if E_F is below. In ZnO E_t is above the CBM showing that hydrogen is a shallow donor under all conditions and only present as ionized H_i^+ . From Van de Walle [94].

2.6.1 Hydrogen as a Donor

Interstitial hydrogen (H_i) is an amphoteric impurity in most semiconductors. Hydrogen forms donors (H_i^+) in p -type materials and acceptors (H_i^-) in n -type materials. Figure 2.9 shows the H_i^+/H_i^- energy level for several semiconductors and shows the amphoteric nature of hydrogen. Hydrogen however only forms donors in ZnO. First principle calculations predict the formation energy of H_i^+ to be the most energetically favourable state of hydrogen across the whole band gap (Figure 2.10) [86]. The main reason for this behaviour is the large strength of the O–H bond, which drives the formation energy of H_i^+ down. This energy is low enough to allow for a large solubility of hydrogen and becomes even lower for Fermi-level positions lower in the band gap as in p -type material.

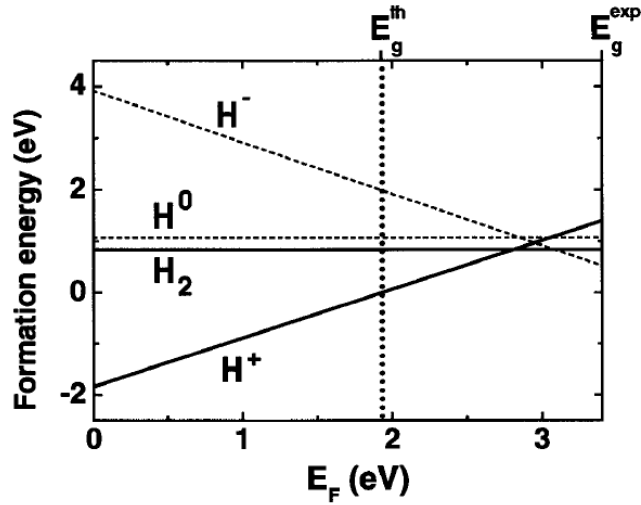


Figure 2.10: Formation energies of interstitial hydrogen in ZnO, as a function of Fermi level, obtained from DFT-LDA calculations. The formation energy of H^+ is the lowest at every position in the band gap. From Van de Walle [86].

There has been experimental evidence of the donor behaviour of hydrogen through electrical measurement and infrared absorption spectroscopy. Hall measurement showed an increase of carrier concentration in ZnO crystals by at least one order of magnitude after having been exposed to a hydrogen plasma [85, 95]. Ion implantation of hydrogen showed an increase in the carrier concentration by four orders of magnitude when compared to the unimplanted one [96]. Annealing in a hydrogen atmosphere showed a LVM of the O-H bond in ZnO at 3336 cm^{-1} through infrared absorption spectroscopy [97–99]. The intensity of this absorption peak increased with annealing time. Electron paramagnetic resonance (EPR) measurements by Hoffmann et al. [87] exhibited two donor resonances, with one of the two related to interstitial hydrogen and determined the ionisation energy of the H_i level to be 35 meV.

Photoluminescence experiments reported the appearance or enhancement of a luminescence peak at 3.363 eV after hydrogen doping [89, 93, 95, 98, 100, 101]. This luminescence peak, called the I_4 line, is often associated with an excitonic recombination involving hydrogen shallow donors (see Section 2.5.3.1).

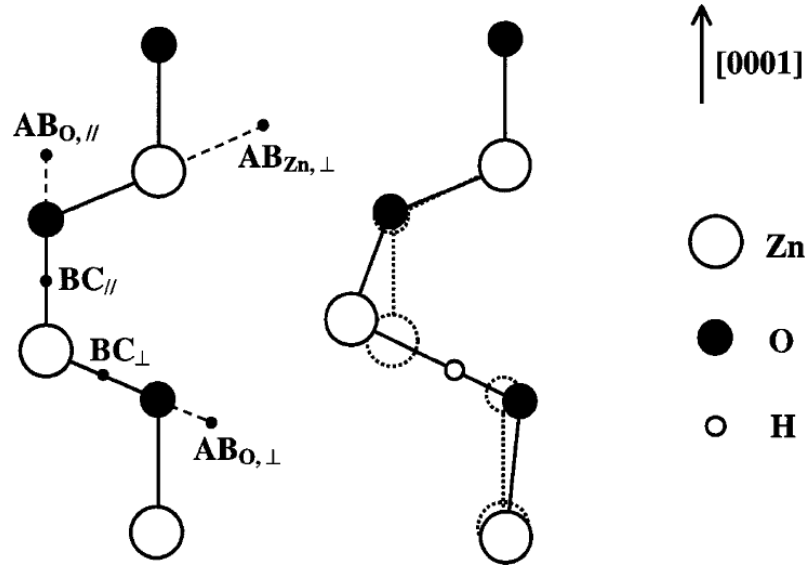


Figure 2.11: Model for H_i in ZnO. Left: ZnO wurtzite structure sites at which H_i can incorporate. Right: Anti-Bonding configuration (AB). From Van de Walle [86]

2.6.2 Location of Hydrogen in the Lattice

The position of hydrogen donors in the lattice is still a matter of controversy with different locations and forms being proposed [102]. Van de Walle [86] proposed two models for H_i donors shown in Figure 2.11. In one model, H is in the anti-bonding (AB_{\perp}) orientation, attached to a host O atom and pointing away from the Zn–O bond. Another model is the bond-centered (BC_{\parallel}) configuration, where H sits between the hosts Zn and O. Also possible is the H at the anti-bonding position of the Zn atom, with the H atom pointing away from the Zn–O bond.

Evidence of these interstitial positions have been found through infrared absorption measurements. The LVM found at 3336 cm^{-1} [97, 98, 103] and 3611 cm^{-1} [98, 99] in hydrogenated ZnO correlate to first principle calculations and have been assigned to both the AB_{\perp} and BC_{\parallel} configurations respectively. Muon implantation experiments performed by Shimomura et al. [104] found that the BC_{\parallel} configuration to be the more stable configuration. This is in agreement with first principle calculations [51]. The migration energy barrier of H_i has been found to

range from 30 meV to 0.5 eV, implying that H_i is mobile at room temperature [105, 106].

In addition to H_i , other configurations have been studied. Recently, DFT calculations predict the possibility of H_O , hydrogen sitting at an oxygen vacancy site [37]. The migration energy barrier of H_O was calculated to be 1.7 eV [105]. There is little experimental evidence for this donor, but the high stability of the D^0X emission weeks after hydrogen doping suggests the formation of H_O since H_i is too mobile at room temperature.

The “hidden” hydrogen in ZnO has also been investigated. Shi et al. [98] performed annealing experiments on hydrogen doped ZnO crystals and found that annealing at temperatures below 300 °C causes the carrier concentration to decrease. Upon annealing at higher temperatures, the carrier concentration recovered. This was attributed to dissociation of hidden H_2 molecules to H_i . Raman spectroscopy showed a LVM at 4145 cm^{-1} which has been attributed to H_2 molecules being formed from migration and recombination of H_i [90].

2.6.3 Interaction of Hydrogen With Defects

In addition to forming shallow donors in ZnO, hydrogen can also interact with defects. Hall measurements showed an increase in both the carrier concentration and carrier mobility after hydrogen doping [107, 108]. Higher carrier concentration usually leads to a strong carrier scattering and the mobility would be decreased because of the increasing carrier scattering. The observed increase in both mobility and carrier concentration suggests that a substantial fraction of the incorporated hydrogen passivates defects at grain boundaries and/or acceptor impurities.

Luminescence measurements done on hydrogen doped ZnO showed a decrease in the deep level luminescence which is associated to recombination at defect centres

after hydrogen doping. CL and PL measurements done on hydrogen doped ZnO crystals showed a quenching of the green luminescence as well as an enhancement of the NBE emission after doping [45, 95, 101, 109]. It has been suggested that hydrogen passivates defects that are responsible for the green luminescence, namely V_{Zn} , by forming neutral $V_{Zn}-H_2$ complexes, thereby quenching the green luminescence.

Evidence of such a complex was reported by Lavrov et al. through infrared absorption spectroscopy [99]. Two absorption lines at 3349.6 cm^{-1} and 3312 cm^{-1} appeared after hydrogen doping which corresponds to the O–H bond vibrational modes. These lines were associated to a defect that contains two hydrogen atoms, one in an O–H bond roughly aligned with the c -axis, and the other in an O–H that forms an angle of 100° with the c -axis. These observations matched first-principles calculations for a hydrogenated Zn vacancy ($V_{Zn}-H_2$).

Chapter 3

Experimental Details

This chapter briefly describes the key experimental techniques used in this project to modify and characterise ZnO. Electronic grade ZnO crystals obtained from the MTI Corporation were used in this project. The crystals were then doped with hydrogen through a hydrogen plasma exposure. The as-received and hydrogen doped samples were characterised by complimentary techniques which study the morphology, optical, electronic and chemical properties of the ZnO crystals.

3.1 ZnO Crystal Specimen

ZnO crystals cut in the a -(11 $\bar{2}$ 0) plane and polished on both sides were obtained from the MTI Corporation, USA. Crystals from this manufacturer were chosen because of their common hydrothermal growth method which yields crystals with high crystallinity and low impurity levels. Figure 3.1 shows a photograph of the as-received crystals. Manufacturer specifications for the crystals are listed in Table 3.1.

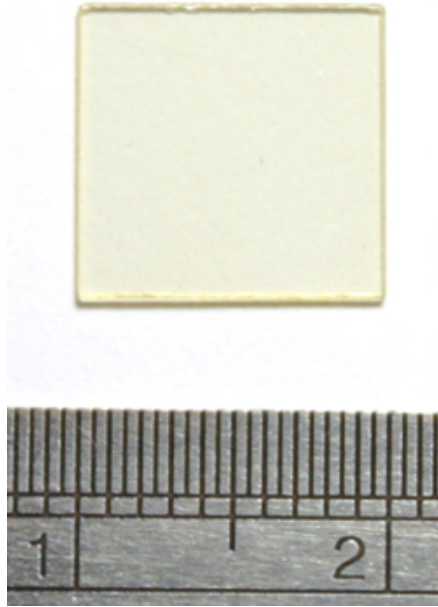


Figure 3.1: Photograph of *a*-plane ZnO crystal obtained from MTI Corporation. Also shown is a ruler showing the 10 × 10 mm dimensions of the crystal.

Table 3.1: ZnO single crystal substrate supplied by MTI Corporation.

| | |
|-------------------------|--------------------------------------------------------------------------------------------------------------------------|
| Purity wt% | >99.99 |
| Impurity wt% | Li: 0.0001 – 0.001; Mg: <0.0005; Al: <0.0030; Si: 0.0030; Ti: 0.0010; Cu: <0.0030; Fe: <0.0050; Ca: <0.0005; Ag: <0.0002 |
| Crystal structure | Hexagonal: $a=3.252 \text{ \AA}$, $c=5.313 \text{ \AA}$ |
| Growth method | Hydrothermal |
| Hardness | 4 (Mohs scale) |
| Density | 5.7 g/cm^3 |
| Melt point | $1975 \text{ }^\circ\text{C}$ |
| Specific heat | 0.125 cal/g |
| Thermoelectric constant | 1200 mV/K at $300 \text{ }^\circ\text{C}$ |
| Thermal conductivity | 0.006 cal/cm/K |
| Thermal expansion | $2.90 \times 10^{-6} / \text{K}$ |
| Transmission range | $0.4 - 0.6 \text{ m} > 50\%$ at 2 mm |
| Dislocation density | $\langle 0001 \rangle$ plane $< 100 / \text{cm}^2$ |

3.2 Sample Cleaning and Preparation

The ZnO crystals were cut to the required size using a diamond pen. The smaller pieces were cleaned in the following way :

- 15 minutes ultrasonic bath in acetone
- 15 minutes ultrasonic bath in isopropyl alcohol
- 15 minutes ultrasonic bath in deionised water
- Nitrogen gas blow dry

Annealing of ZnO crystals was done in a Lindberg/Blue single zone tube furnace. The furnace allows annealing at temperatures up to 1100°C under vacuum or controlled gaseous environments.

3.3 Hydrogen Doping

Hydrogen plasma treatment was done through an R.F plasma. A custom built plasma reactor was assembled for doping ZnO. The basic setup is illustrated in Figure 3.2. Hydrogen gas is flown into the evacuated chamber moderated using an Apex mass flow controller. A constant pressure is monitored with a Lam research series capacitance diaphragm gauge. Plasma is generated using an AG 0202-HV OS high voltage plasma generator from T&C Power Conversion, Inc. Hydrogen gas is ionised creating energetic radicals which penetrate into the sample and diffuse. The sample was heated during treatment to encourage diffusion of hydrogen.

It was found that hydrogen can be incorporated in ZnO in the range of 25°C to 450°C and in a time as low as 10s. Optimal parameters for the plasma cycle consisted of heating the clean ZnO sample in an evacuated chamber (10^{-1} Torr) to 200°C. RF power of 15 W was used with 10 sccm H₂ flow rate to create hydrogen radicals. After plasma treatments the sample was cooled in a hydrogen atmosphere to room temperature before removal from the chamber for analysis.

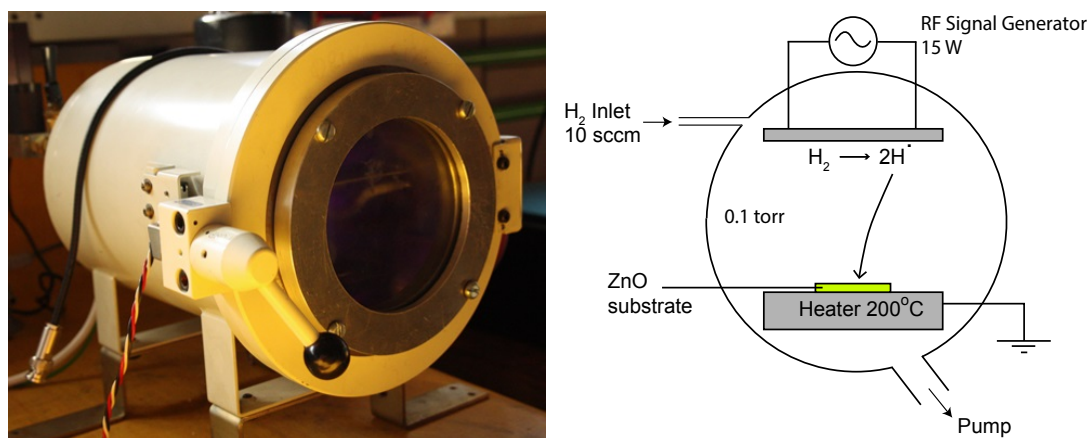


Figure 3.2: Photograph (left) and schematic (right) of the plasma chamber used for H-doping of ZnO crystals identifying key features.

3.4 Scanning Electron Microscopy (SEM)

Scanning electron microscopy (SEM) has been used to assess the morphology of the samples before optical and electrical characterisation as well as any possible surface damage caused by the doping procedure.

In a typical SEM (Figure 3.3), electrons are emitted from a heated filament and accelerated towards the anode with energy ranging from 100 eV to 30 keV. The electron beam is then focused by the condenser and objective lens to form a narrow beam with a diameter of the order of nanometres on the sample surface. This beam passes through scanning coils which deflect the beam in a raster pattern over an area of the sample surface.

Interaction of the primary beam with matter in an SEM can lead to a series of scattering processes. High energy electrons interacting with matter can lead to the generation of backscattered electrons, secondary electrons, X-rays, or light (Figure 3.4). Each emission gives information about the sample, e.g. secondary electrons give a topographical image of the sample surface, backscattered electrons give spatial information dependent on compositions, X-rays give the chemical composition and concentration of elements, while the light emitted gives

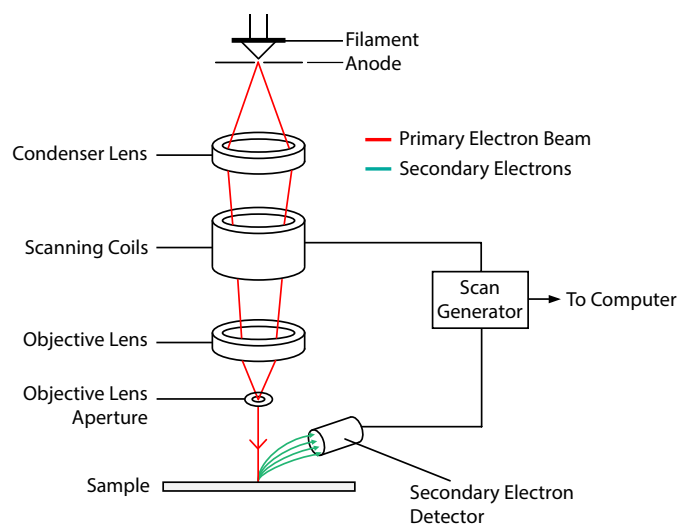


Figure 3.3: Schematic diagram showing key parts of a typical SEM.

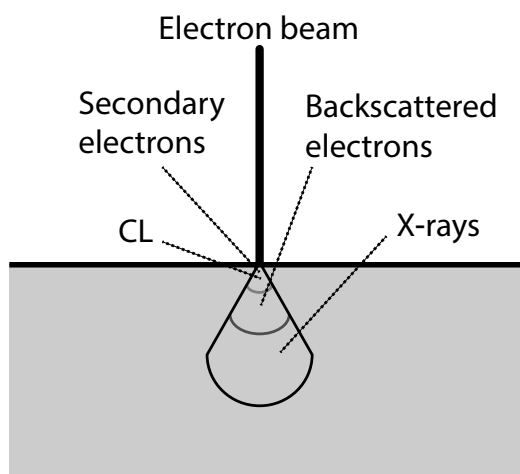


Figure 3.4: Processes induced by electron bombardment.

information about defects in the sample.

In this work an FEI Quanta 200 ESEM was used for electron beam analysis of ZnO. The spatial resolution of the microscope is 3.0 nm at 30 keV or 10 nm at 3 keV. The operating pressure inside the microscope chamber was $<10^{-5}$ Torr. Beam current was measured by using a Faraday cup. The Faraday cup consisted of a hole drilled in the specimen holders. The beam is focused into the aperture and the cavity under the aperture absorbs virtually all electrons from the main

beam. The stage is then connected to an ammeter to measure and display the absorbed current.

3.5 Cathodoluminescence Spectroscopy

Cathodoluminescence (CL) is the light emitted through the recombination of electron-hole pairs following excitement by a focused electron beam. CL occurs through the radiative recombination of electron-hole pairs produced after irradiation from an electron beam (See Section 2.5.3 for a detailed description of the generation and recombination processes). CL is a powerful investigative tool that can examine the optical properties of materials in a non-invasive manner. CL can obtain resolution below that of the diffraction limit of light. The technique can be used to characterise the composition and defects of a material.

The spatial resolution of CL is strongly determined by the interaction volume of the electrons incident on the material. In this volume, the electrons undergo a series of elastic and inelastic scattering events, which can result in electron-hole pair generation leading to CL. The maximum range (R_e) for an electron can be approximated by using the Kanaya and Okayama equation [110]:

$$R_e(\mu\text{m}) = \frac{0.0276AE_b^{1.67}}{\rho Z_e^{0.889}} \quad (3.1)$$

where E_b is the accelerating voltage of the electron beam in keV, A is the atomic weight of the material in g/mol, ρ is the material density in g/cm³ and Z_e is the effective atomic number. Z_e can be calculated by using a weighted average of the atomic numbers of the constituent atoms such as:

$$\begin{aligned} Z_e &= \frac{A_{Zn}}{A_{ZnO}} \times Z_{Zn} + \frac{A_O}{A_{ZnO}} \times Z_O \\ &= \frac{65.38}{81.39} \times 30 + \frac{16.01}{81.39} \times 8 \\ &= 25.67 \end{aligned} \quad (3.2)$$

Electron-hole pair generation by electrons is different to the one by photon. A photon can generate only one electron-hole pair while an electron can generate thousands of electron-hole pairs in the interaction volume. The generation rate, G , of electron-hole pairs can be described by:

$$G = \frac{E_b I_b Q (1 - \gamma)}{e E_g} \quad (3.3)$$

where I_b is the beam current, e is the charge on an electron, γ is the backscatter coefficient of the material, E_g is the band gap energy and Q is the quantum efficiency for electron-hole pair generation.

It is possible to obtain a high spatial resolution using CL spectroscopy, with resolutions below 10 nm under ideal conditions. It is also possible to use both depth and power resolved analysis techniques with this method, simply by varying the beam operating parameters.

In this project, CL was collected inside an FEI Quanta 200 ESEM. Figure 3.5 shows the experimental setup used. Light emitted from the sample was collected by a parabolic mirror and then guided through optical fibers to be analysed by a detector. Two detectors were used in this project on the CL system. An Ocean Optics QE65000 detector was used to collect full range CL spectra of ZnO. The QE65000 consists of a 1024×54 active pixel area with acquisition range of 200 to 1100 nm with a spectral resolution of 5 nm. High resolution CL, of mainly

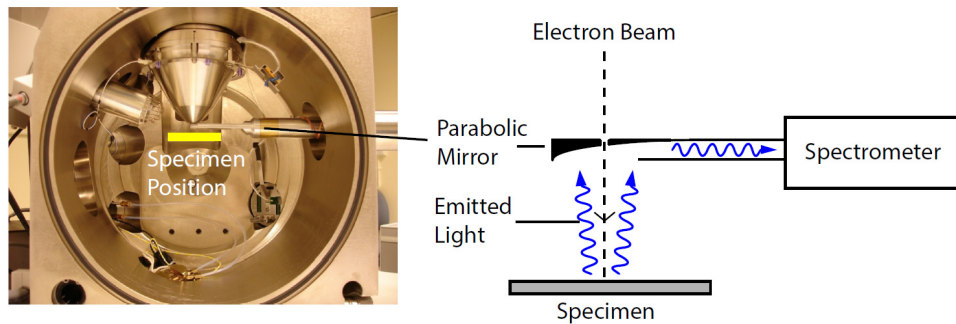


Figure 3.5: Photograph of the experimental setup for collecting CL (left) with a schematic identifying the main parts (right).

the near band edge region of ZnO, was collected with a Hamamatsu S7011-1007 CCD sensor which consists of 1044×124 active pixels. The sensor was housed inside a Hamamatsu C7021 detector head. The light was dispersed in an Oriel MS 257 $\frac{1}{4}$ m monochromator by a 1200 lines/mm grating. This setup allowed for a spectral resolution of 0.1 nm over a 53 nm range.

Temperature dependent CL was achieved using three SEM cooling/heating stages. A Gatan C1002 liquid nitrogen cold stage was used for cooling samples down to 80 K and a Gatan CF302 continuous flow liquid helium cold stage for cooling to 5 K. High temperature CL up to 500 °C was performed on a custom built heater stage.

3.5.1 CL System Calibration

All CL spectra taken were calibrated for the response of the system in both intensity and wavelength. An Oriel 63355 200 W QTH calibrated lamp of known spectral profile was used for intensity calibration. The correction curve was obtained according to the following equation:

$$\text{Correction curve} = \frac{\text{Normalised reference intensity}}{\text{Normalised measured intensity}} \quad (3.4)$$

Figure 3.6 shows the measured intensity as a function of wavelength as well as the reference emission spectrum of the lamp provided by Oriel and the calculated correction curve. The peaks in the correction curve at 400 nm and above 900 nm are caused by absorption of the light by the optical fiber.

Calibration for high resolution CL spectral analysis (resolution of 0.1 nm) was achieved by measuring atomic spectral lines of mercury or neon immediately after the acquisition of the ZnO spectra. Figure 3.7 shows CL spectra of a mercury and a neon lamp as well as the calculated wavelength calibration curve. The

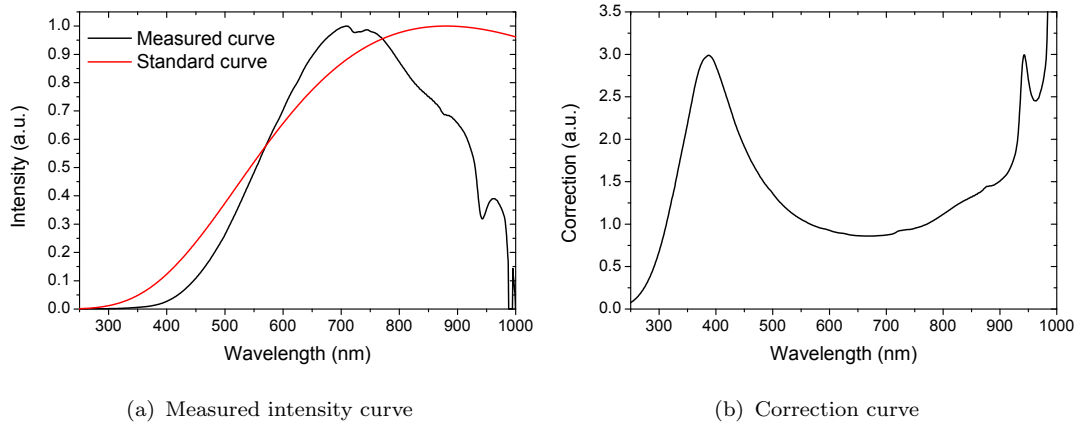


Figure 3.6: (a) CL spectrum of the lamp taken through the CL system using the Ocean Optics QE65000 detector and the emission spectrum of the lamp. (b) The correction curve obtained according to Equation 3.4.

calibrated wavelength was converted into electron volts using the relation:

$$\text{Photon energy (eV)} = \frac{1239.841856}{\lambda \text{ (nm)}} \quad (3.5)$$

Since the spectrometers measure photons per sec in a Δnm interval in λ , $I(\lambda)$ the measured intensity in eV, $I(\text{eV})$ needs to be corrected to have equal steps in ΔeV by multiplying $I(\lambda)$ by λ^2 .

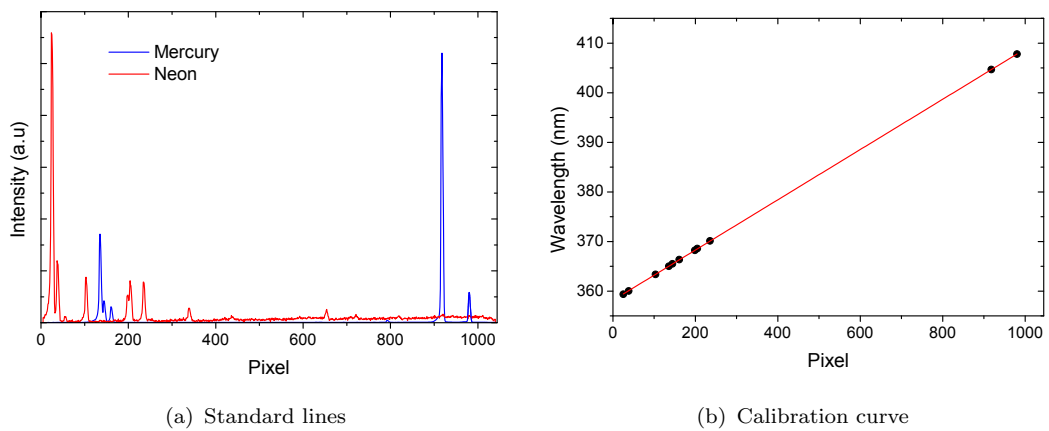


Figure 3.7: (a) Mercury and neon spectral lines and (b) wavelength calibration curve.

3.6 Monte Carlo Simulations (CASINO)

The electron range in a solid can be determined from Equation 3.1. This is however an approximation and it is more useful to consider the overall interaction volume of electrons with the material. One method is to use a Monte Carlo simulation package such as CASINO (monte CARlo SIMulation of electroN trajectory in sOlids) to determine the actual interaction volume and hence penetration range of electrons [111]. CASINO is a single scattering Monte Carlo simulation specifically developed for low electron energy beam interactions (0.1 to 30 keV). It can generate various signals produced in normal SEM operation such as X-ray generation, backscattered and secondary electrons as well as CL signals.

CASINO implements Monte Carlo methods in which elastic scattering events are modeled explicitly using random numbers generated with weighting factors to produce an appropriate statistical distribution of scattering events. The first step in the simulation of an elastic collision is to determine which atomic species is involved. This is calculated based on the atomic fraction and experimentally determined cross-section of each element in the material.

$$Random > \sum_{i=1}^n \frac{F_i \sigma_i}{\sum_{j=1}^n F_j \sigma_j} \quad (3.6)$$

where *Random* is a random number uniformly distributed between 0 and 1, σ_i is the cross section of element *i*, F_i is the atomic fraction of element *i* and *n* is the number of elements in the region. When the inequality above is true, the element responsible for the collision is element *i*. The scattering angle and distance travelled between collisions are calculated based on material properties and randomly generated numbers. Inelastic scattering is not simulated explicitly, instead a continuous slowing down approximation is applied in which an electron gradually loses energy over the distance travelled between collisions (*L*). Using

this approach, the energy of a simulated electron at a given position is

$$E_i = E_{i-1} + \frac{dE}{dS} \times L \quad (3.7)$$

where E_i and E_{i-1} are the respective energies at the current and previous collisions and dE/dS is the rate of energy loss measured in keV/nm. The rate of energy loss is material dependent and represents an averaging of inelastic scattering events over the distance travelled.

CASINO is also able to take minority carrier diffusion into account which has a significant effect on the size of the interaction volume, specially at low beam energies ($E_b < 15$ keV) where the carrier diffusion length is of the order of the electron penetration depth. For ZnO, the carrier diffusion length is ~ 90 nm [6]. The interaction volume is in a teardrop shape for no diffusion with the majority of electrons being deposited and CL generated in the first 17 nm below the surface as in Figure 3.8(a). While the depth of electrons injected in the sample does not change, the interaction volume is enlarged when carrier diffusion is taken into account and the depth profile of CL generated changes. The majority of CL is generated in 10 to 35 nm from the surface depending on the diffusion models used (Figure 3.8(b)-3.8(d)).

The parameters used for CASINO simulations used in this project are given in Table 3.2.

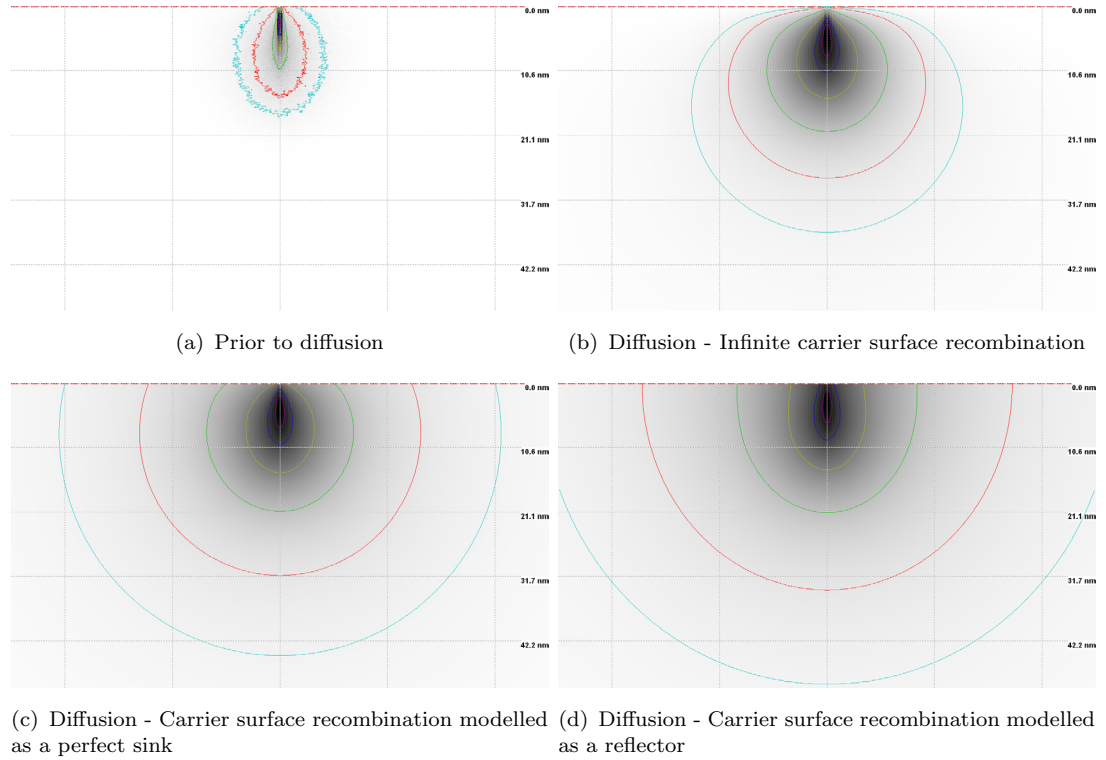


Figure 3.8: Influence of carrier diffusion models on the interaction volume in bulk ZnO. Beam energy was 1 keV with 500,000 electrons simulated. The vertical distance is the same in all 4 figures.

Table 3.2: CASINO simulation parameters for depth approximations.

| Parameter | Setting |
|-------------------------------|--------------------------------------------------------|
| Sample | ZnO substrate |
| Density | 3.998 38 g/cm ³ |
| Weight fraction (Zn:O) | 0.803 397 : 0.196 603 |
| Beam energies | 0.1 – 30 keV (0.1 keV steps to 1 keV then 1 keV steps) |
| Number of simulated electrons | 500 000 |
| Beam radius | 1 nm |
| Total Cross Section | Mott by Interpolation |
| Partial Cross Section | Mott by Interpolation |
| Effective Section Ionisation | Casnati |
| Ionisation Potential | Joy & Luo [1989] |
| Random Number Generator | Press et al. [1986] |
| Directing Cosin | Soum et al. [1979] |
| dE/dS Calculation | Joy & Luo [1989] |

3.7 Electrical Measurements

Electrical measurements were performed by the Van der Pauw method [112]. This technique allows measurements of resistivity, sheet carrier density of the majority carrier and mobility of the majority carrier. The main advantage of the Van der Pauw method is the ability to measure the properties of samples of any arbitrary shape, as long as the thickness of the sample is less than its length or width.

Ohmic contacts on ZnO crystals were made by dipping the end of a thin wire into molten indium and rapidly bringing a tiny amount of molten indium on the wire to the corners of the crystals before the indium solidifies. The contacts were labeled A, B, C and D as in Figure 3.9.

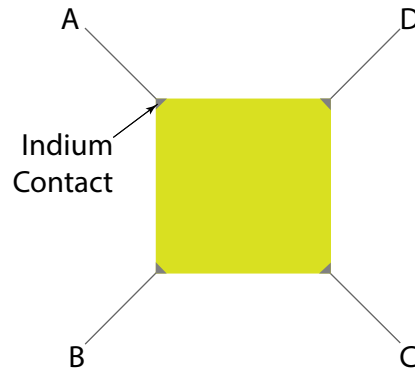


Figure 3.9: Van der Pauw setup for resistivity and Hall measurements.

3.7.1 Resistivity Measurement

A current is flowed along one edge of the sample, I_{AB} and the voltage across the opposite edge, V_{CD} is measured. The resistance can then be found from Ohm's law:

$$R_{AB,CD} = \frac{V_{CD}}{I_{AB}} \quad (3.8)$$

The sheet resistance, R_s , can then be calculated from two of those resistances, one along the vertical edge ($R_{AB,CD}$) and one along the horizontal edge ($R_{BC,DA}$)

by using the Van der Pauw equation:

$$\exp\left(-\pi \frac{R_{AB,CD}}{R_s}\right) + \exp\left(-\pi \frac{R_{BC,DA}}{R_s}\right) = 1 \quad (3.9)$$

For more accurate measurements, reciprocal measurements $R_{CD,AB}$ and $R_{DA,BC}$ can be taken and the average resistance along the vertical and horizontal edges calculated. The Van der Pauw formula then becomes:

$$\exp\left(-\pi \frac{R_{vertical}}{R_s}\right) + \exp\left(-\pi \frac{R_{horizontal}}{R_s}\right) = 1 \quad (3.10)$$

The resistivity, ρ , of the sample of thickness, t , is then found by:

$$\rho = R_s \times t \quad (3.11)$$

3.7.2 Hall Measurement

Hall measurements were performed using the same setup for the resistivity measurements. First, current was passed through opposite corners, I_{AC} , while the voltage across V_{BD} was measured for a range of current I_{AC} . This was repeated with a magnetic field, B , applied perpendicular to the surface of the sample. The voltage V_{BD} was then taken for a series of current again. The difference between the voltages taken is the Hall voltage, V_H . For more accurate results, the magnetic field direction can be reversed and the average of the Hall voltages taken. The carrier concentration, n , can then be found using:

$$n = \frac{BI}{eV_H} \quad (3.12)$$

where e is the elementary charge. From the measured resistivity and the carrier concentration, the mobility, μ , of the carriers can be calculated using:

$$\mu = \frac{1}{enR_s} \quad (3.13)$$

3.8 Synchrotron Light Experiments

Synchrotron radiation is electromagnetic radiation emitted as a result of the change of the trajectory of a high speed electron moving through a magnetic field. Synchrotron radiation provides radiation ranging from the ultraviolet to high energy X-rays with intensity several orders of magnitude greater than conventional sources (10^5 to 10^6 times greater), along with the ability to tune the source to selected energies. The light is also highly polarised. The use of high energy radiation induces a photoelectric response in a sample. This results in the emission of photoelectrons or other types of radiation that have characteristics dependent on their original electronic states. Synchrotron light experiments were performed at the Soft X-ray Beamline of the Australian Synchrotron [113].

3.8.1 X-Ray Photoelectron Spectroscopy

X-ray photoelectron spectroscopy (XPS) analysis is accomplished by irradiating a sample with monochromatic soft x-ray photons and analysing the energy of the detected electrons that are emitted from the sample. Using XPS, the chemical identity and concentration of elements in the sample can be determined by comparing the known binding energies of the elements E_b with those deduced from the kinetic energies of the emitted electrons E_k

$$E_b = h\omega - E_k - \phi_d \quad (3.14)$$

where $h\omega$ is the energy of the X-ray photon, and ϕ_d is the work function of the detector.

Another advantage of performing XPS measurements at synchrotron facilities is the energy of the X-ray photons can be finely tuned. Common laboratory XPS setups use aluminium or magnesium targets as X-ray source with photon energies of 1486.6 eV (Al K_α) or 1253.6 eV (Mg K_α). Photon energy ranging from 90 eV to 1500 eV was available for use at the Australian Synchrotron facility. This allowed for optimising the XPS signal for a particular photoemission by choosing the appropriate photon energy. Figure 3.10 shows the photoionisation cross sections for zinc, oxygen and lithium photoemissions [114]. The cross section for Li 1s is 3 orders of magnitude higher with photon energies of 150 eV compared to common laboratory sources.

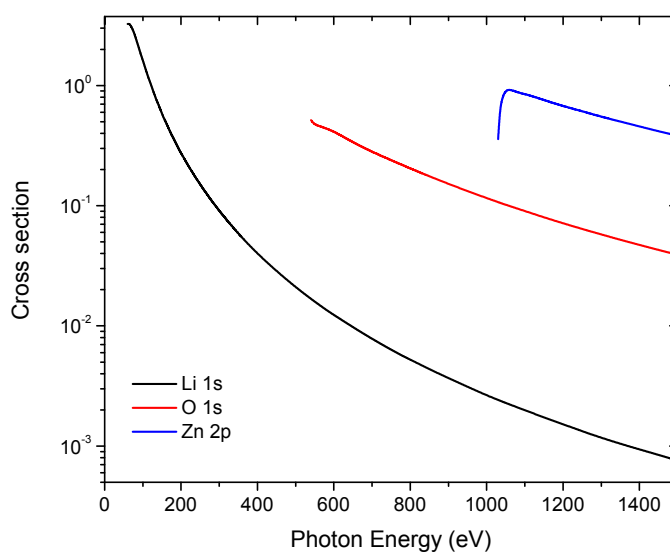


Figure 3.10: X-ray photoionisation cross sections for Zn 2p, O 1s and Li 1s photoelectrons. The cross section for Li 1s is 3 orders of magnitude higher with photon energies of 150 eV compared to common laboratory sources. Data taken from [114].

The penetration power of X-ray photons in solids is of the order of 1 μm to 10 μm . However, the electron interaction with matter is higher than that of photons. This higher interaction means that the mean free path of electrons is only of the order

of tens of angstroms. Only photoelectrons which are generated directly below the surface can leave the surface and contribute to the XPS signal. XPS is therefore a highly surface sensitive analysis technique.

3.8.2 X-Ray Absorption Near Edge Spectroscopy

X-ray absorption near edge spectroscopy (XANES) measures the absorption of X-rays as a function of X-ray photon energy. XANES is used to determine the oxidation state and coordination number of elements in a material, as well as the site symmetry of the elements. XANES also gives information on the conduction band of the materials because it is probing empty states. The X-ray photon energy is scanned over the energy of core levels of the constituent elements of the sample. An electron is excited from its level and a hole is left. An electron from a higher energy state will fall into this vacancy and releases the energy in the form of a photon or further excite an electron from a higher state to form an Auger electron.

A XANES spectrum shows a typical oscillatory fine structure shape which extends over hundreds of electron volts above the main absorption edge. Those peaks correspond to internal electron transitions between core levels. This oscillation arises due to the wave nature of the emitted photoelectron. Scattering between the photoelectron and neighbouring atoms causes a standing wave to be formed which is then reflected by the oscillations in the XANES spectrum.

XANES was performed in two configurations, total electron yield (TEY) and total fluorescence yield (TFY). TEY is performed when the sample is connected to ground through an ammeter and the neutralization current is monitored while TFY measures photons that are emitted after electrons of lower binding energy fill the created core hole.

3.9 Raman Spectroscopy

Raman spectroscopy is used to observe vibrational, rotational and low-frequency modes in a material. Raman spectroscopy works on the principle of inelastic scattering of monochromatic light by the vibrational modes of the material. The incoming photon can lose energy due to excitation of rotational, vibrational or electric states. The photon can also gain energy when an excited mode releases energy to the photon and relaxes to lower energy levels. These processes are called Stokes and anti-Stokes Raman scattering respectively. If the change in the scattering occurs in quantised energy levels, the transitions appear as distinct lines in the spectrum which are separated from the laser frequency by a characteristic Raman shift to lower or higher energies.

The wurtzite structure of ZnO with the space group $C_{6v}^4(P6_3mc)$ has $n = 4$ atoms in the primitive unit cell which leads to $3n = 12$ vibrational eigenmodes (3 acoustic and 9 optical modes). These modes are classified according to the following irreducible representations [115, 116]:

$$\Gamma = 2A_1(1) + 2B_1(1) + 2E_1(2) + 2E_2(2) \quad (3.15)$$

This summation corresponds to 12 modes because of the one-fold degeneracy of the A and B modes and the two-fold E modes. The three acoustic phonon modes consist of one A_1 mode and one E_1 mode pair, the other nine modes are optical modes:

$$\Gamma_{opt} = A_1(1) + B_1^{low}(1) + B_1^{high}(1) + E_1(2) + E_2^{low}(2) + E_2^{high}(2) \quad (3.16)$$

Figure 3.11 displays a schematic of the displacement of the six optical phonon modes. The displacements for the A_1 and B_1 modes are directed along the c -axis while the E_1 and E_2 modes are perpendicular to the c -axis. The E modes oscillate

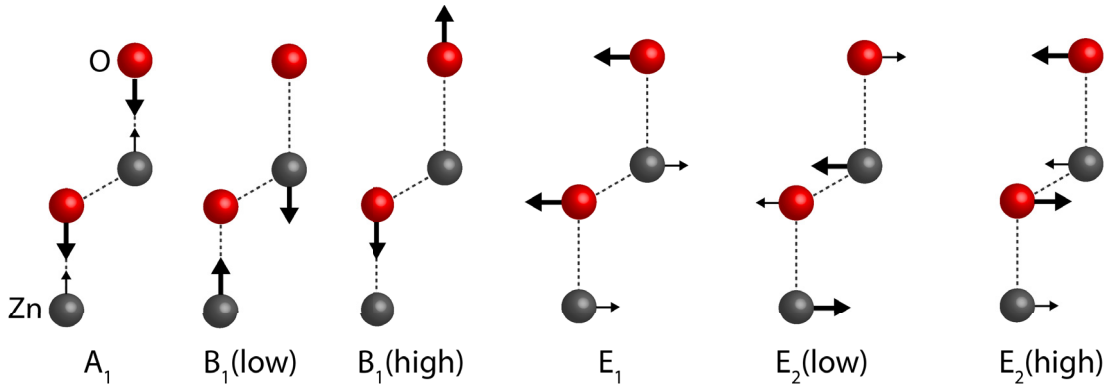


Figure 3.11: Schematic illustrations of the ion displacements of optical phonon modes in ZnO. The larger arrows represent the dominant displacement vectors. The A_1 , B_1^{high} , E_1 and E_2^{high} are oxygen-dominated while the B_1^{low} and E_2^{low} modes are dominated by the zinc displacements. Adapted from [117]

linearly and independently in the directions perpendicular to the c -axis with the same energy which leads to the two-fold degeneracy of the E_1 and E_2 modes.

The A_1 and E_1 modes consist of oscillations of the rigid Zn sublattice vs. the O sublattice which result in an oscillating polarisation. The polarity induced macroscopic electric fields split these polar modes into longitudinal optical (LO) modes with an ion displacement parallel to the phonon propagation vector and transversal optical (TO) modes with perpendicular displacement vectors. In contrast to the A_1 and E_1 Raman modes, the B_1 and E_2 modes are non-polar and as such do not exhibit LO-TO splitting. No polarisation is induced for the B modes since one sublattice is at rest while the atoms in the neighbouring other sublattices move opposite each other. Similarly in the E_2 modes, the non-polar character of the vibration is caused by the mutual compensation of the displacement in each sublattice.

Raman measurements were performed in a Renishaw inVia Raman spectrometer system equipped with a Leica DMLB microscope and a red Renishaw helium neon laser source with emission wavelength of 633 nm and power of 17 mW.

3.10 Charge-based Deep Level Transient Spectroscopy

Charge-based Deep Level Transient Spectroscopy (Q-DLTS) is used to investigate trap depths and cross sections in materials. Q-DLTS has been specifically developed to probe carrier traps in the near surface region and accordingly applied for investigations of ZnO crystals.

In the Q-DLTS method, cyclic bias pulses are applied to a Schottky barrier junction to excite carrier traps. A band diagram is shown in Figure 3.12 to illustrate the charge filling and emission mechanism. The electron occupation of the traps is monitored by measuring the associated charge transients as the junction returns to thermal equilibrium. The charge transient is measured at two times (t_1 and t_2 from the beginning of discharge) and the charge ΔQ flowed through the circuit during the period $t_1 \rightarrow t_2$ is measured as a function of the rate window $\tau = (t_2 - t_1) / \ln\left(\frac{t_2}{t_1}\right)$. For electrons, the gate timed charge difference is [118, 119]:

$$\begin{aligned}\Delta Q &= Q(t_2) - Q(t_1) \\ &= Q_0 [\exp(-e_n t_2) - \exp(-e_n t_1)]\end{aligned}\quad (3.17)$$

where Q_0 is the total charge trapped during the filling pulse. The thermal emission rate e_n , according to Maxwell-Boltzmann statistics, can be expressed as [119, 120]:

$$e_n = \sigma \Gamma_n T^2 \exp\left(-\frac{E_a}{kT}\right)\quad (3.18)$$

where σ is the capture cross section, E_a is the activation energy, and Γ_n is a constant associated with the electron mass.

By keeping the ratio $t_2/t_1 = \alpha$ constant, the function $\Delta Q(\tau)$ is maximum when the rate window is equal to the emission rate of trap, i.e. $\tau_m^{-1} = \frac{\ln \alpha}{(\alpha-1)t_1} = e_n$. The activation energy of a trap and its cross section can therefore be obtained from

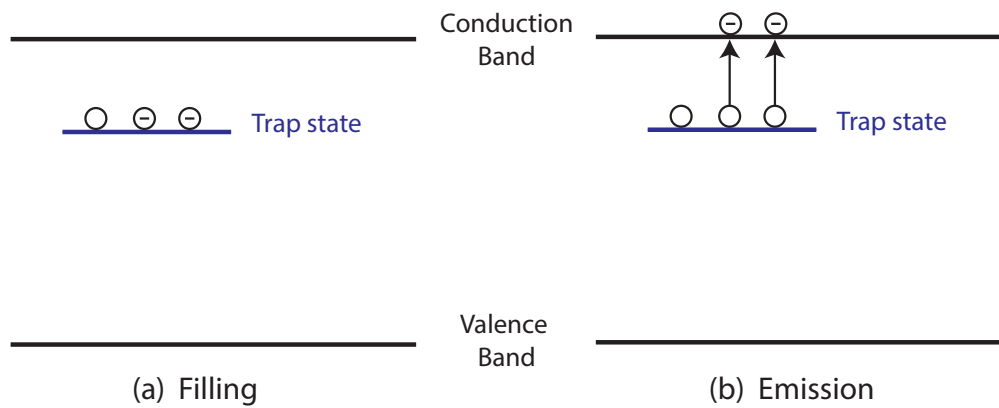


Figure 3.12: Band diagram showing the (a) trap filling and (b) emission processes.

an Arrhenius plot of Equation 3.18, whereas the trap density can be calculated from the maximum ΔQ_{max} .

A gold Schottky contact pad with a thickness of 150 nm was deposited by evaporation on one face of the ZnO crystal through a shadow mask, while indium ohmic contact was established on the opposite face as shown in Figure 3.13. Current-voltage and isothermal Q-DLTS measurements were conducted in vacuum using the ASMEC-02 system, supplied by InOmTech Inc.

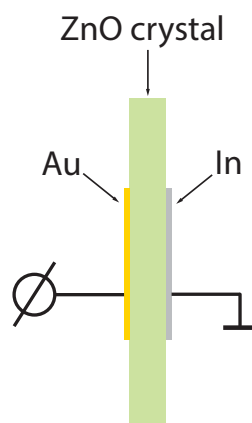


Figure 3.13: Schematic illustration of the DLTS setup showing contacts.

3.11 Other Characterisation Techniques

In addition to the techniques described in this chapter, the following characterisation tools were also used to study the crystal morphology and optical properties of the ZnO crystals:

X-Ray Diffraction

X-Ray Diffraction (XRD) was performed on a Siemens D5000 X-ray Diffractometer. The diffractometer uses copper K-alpha radiation with a wavelength of 1.5418 Å. The XRD was operated in $\theta - 2\theta$ mode.

Atomic Force Microscopy

Atomic Force Microscopy (AFM) measurements were performed on a Digital Instruments Dimension 3100 AFM. AFM was used to investigate surface morphology and mean surface roughness.

Photoluminescence

Photoluminescence (PL) measurements were performed in a liquid helium bath cryostat which allows measurements from 7 K to 300 K. The samples are excited by the 325 nm emission line of a HeCd laser and the emitted light was dispersed by a Spex-1404 double monochromator (spectral resolution 50 μeV) and detected by a bi-alkali photodetector.

Chapter 4

Hydrogen Doped ZnO

4.1 Introduction

Hydrogen can have a significant effect on the optical and electrical properties of ZnO. In this project hydrogen was incorporated into ZnO crystals by exposing ZnO to mild hydrogen plasma. The main advantage of plasma treatment over other hydrogen doping methods, such as thermal annealing in a hydrogen atmosphere, is that ZnO can be kept at relatively low temperatures. In this project the sample temperature was kept below 500 °C, at which the thermal energy is considerably lower than the formation energies of native defects reported to be in the range of 0.5 eV to 5 eV [39]. Optimal plasma conditions are important to ensure minimal damage to the crystal surface and structure during hydrogen incorporation. It has also been reported that hydrogen can be removed from ZnO by thermal diffusion at temperatures higher than 500 °C [85].

The plasma was generated with a 15 W RF source. The RF field strips electrons from hydrogen molecules forming ionised atomic hydrogen (H^+) as well as ionised hydrogen molecules (H_2^+) with a typical ratio of $H^+:H_2^+$ being 3:1 [121]. The generated ions then diffuse inside the chamber towards the crystals. The H–H

bond energy in an H_2 molecule is 4.52 eV [122] and it is therefore expected that the majority of hydrogen species are being incorporated as atomic hydrogen. These atomic hydrogen species can then interact not only with the sample surface, but also diffuse into the bulk to form shallow donors, H-related defect complexes or hydrogen molecules inside the crystals. The low diffusion barrier of hydrogen in ZnO of $\sim 0.1 - 0.5$ eV [123–125] means that hydrogen is mobile in ZnO to readily form defect complexes such as $V_{Zn}-H_2$ or H_2 molecules even at room temperature.

This chapter presents the effects of hydrogen doping in ZnO. Particular attention will be given to the following aspects of hydrogen doping:

- the incorporation and diffusion of hydrogen in ZnO at low temperature.
- the effects of hydrogen on the optical and electrical properties of ZnO.
- the interaction of hydrogen with native defects and impurities.
- the chemical states of hydrogen dopants.

4.2 Crystal Morphology and Structure

X-ray diffraction (XRD) and atomic force microscopy (AFM) were used to assess the impact of hydrogen plasma on the crystallinity and the surface morphology of the crystals.

X-ray diffraction (XRD) was performed to study the crystallinity of the crystals before and after hydrogen plasma. Figure 4.1 shows the θ - 2θ XRD patterns for both the as-received and H-doped ZnO crystals. Both patterns exhibit a sharp peak at 56.5° and no other significant XRD peaks. This shows that the crystals are cut along the a -plane ($11\bar{2}0$) of the wurtzite structure. The smaller peaks at 51° and 54° do not correspond to any main crystallographic planes of ZnO. They do however indicate the possibility of a slight mis-cut in the crystal. It is

worth noting that the intensity of those smaller peaks are about three orders of magnitude smaller than the main peak at 56.5° . The XRD pattern is unchanged after hydrogen plasma treatment indicating that the presence of hydrogen in the crystal lattice does not significantly affect the high crystallinity of the bulk of the crystals. XRD however is a bulk measurement technique and does not give information about the surface of the crystal.

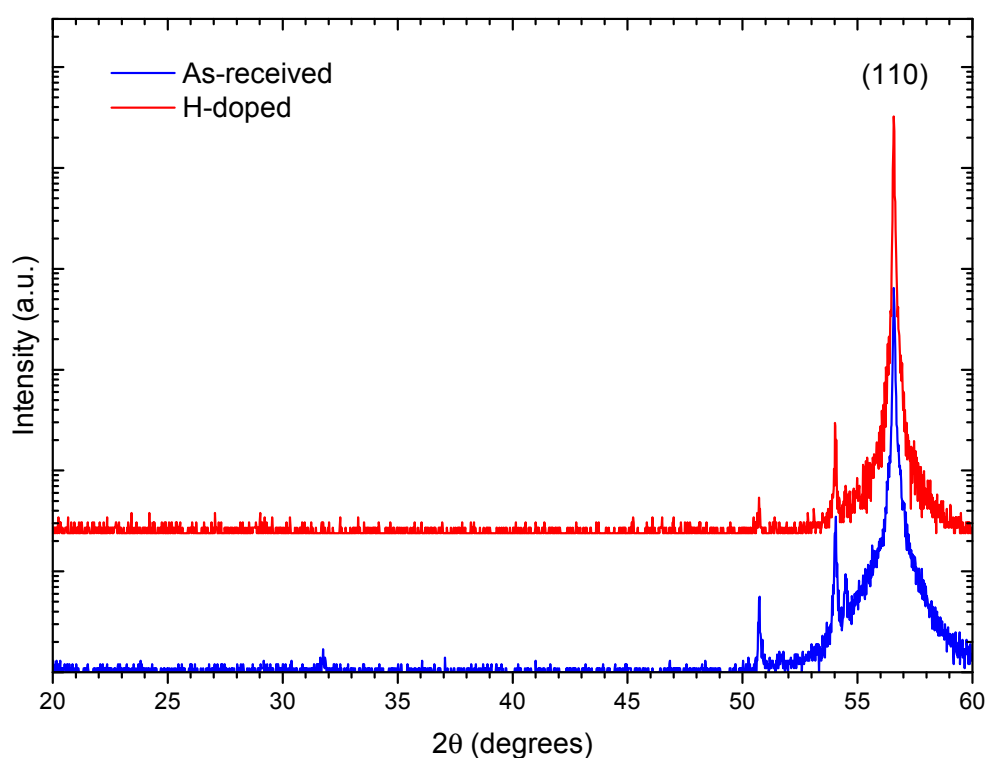
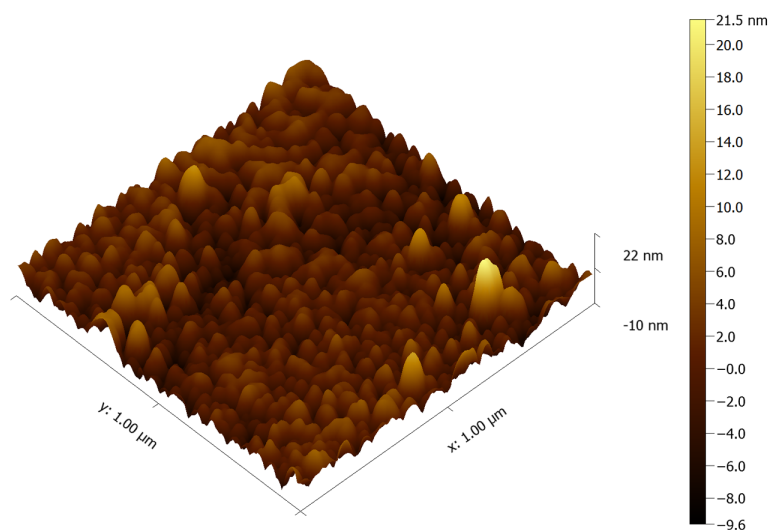


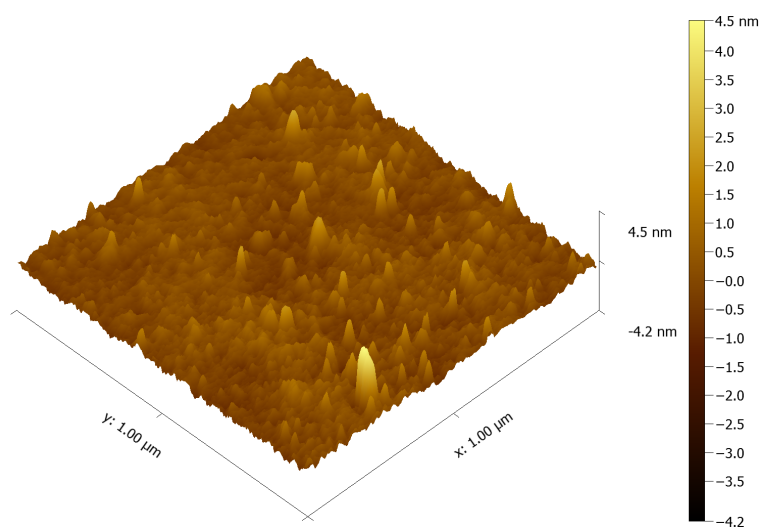
Figure 4.1: X-ray diffraction patterns for as-received and H-doped ZnO exposed to the hydrogen plasma for 120s. Patterns were recorded in the θ - 2θ mode.

Atomic Force Microscopy (AFM) studies were done on the crystals to probe the surface for any changes after hydrogen plasma treatment. Figure 4.2 shows topographic AFM images of the surface of the crystals before and after 10 minutes of hydrogen plasma treatment. The as-received crystal shows grain like surface morphology. These grains are not found on the doped crystal which shows a smooth surface. The roughness of the surface is reduced from 3 nm to 0.5 nm measured over an area of $1\ \mu\text{m} \times 1\ \mu\text{m}$ following hydrogen plasma exposure. This

change in the surface morphology can be attributed to removal of zinc and oxygen atoms from the surface by the plasma [126]. This is similar to etching of the surface with atomic hydrogen as the reactive species [127].



(a) As-received



(b) H-doped

Figure 4.2: AFM images of the surface of (a) as-received and (b) 10 minutes H-doped ZnO. The surface roughness was reduced from 3 nm to 0.5 nm after plasma exposure.

4.3 Electrical Properties of Hydrogen Doped ZnO

Electrical measurements were performed using the Van der Pauw method as described in Section 3.7. Hall measurements were done on both the as-received and H-doped crystals to determine the carrier concentration and mobility of the majority carrier. The results are summarised in Table 4.1. Carrier concentration is increased by two orders of magnitude from $2.1 \times 10^{14} \text{ cm}^{-3}$ to $2.8 \times 10^{16} \text{ cm}^{-3}$. This is consistent with the formation of new shallow donors such as H_i or H_O [85, 95]. The increase in mobility of the majority carrier indicates a decrease of impurity scattering as a result of passivation of defects by hydrogen [107, 108]. This is consistent with optical results reported in Section 4.4.2.

Table 4.1: Hall measurements on as-received and H-doped ZnO

| | Carrier concentration (cm^{-3}) | Mobility ($\text{cm}^2/\text{V s}$) |
|-----------------|--------------------------------------------|---------------------------------------|
| As-received ZnO | 2.1×10^{14} | 100 |
| Doped ZnO | 2.8×10^{16} | 167 |

Hydrogen plasma treatments, under similar plasma conditions to those used in this work, have shown that hydrogen will diffuse to a depth of $\sim 50 \mu\text{m}$ as revealed by SIMS measurements [85]. The Van der Pauw method however measures the sheet surface conductivity and those measurements may not be representative of the whole crystal. It has been reported that the conductivity in ZnO is dominated by surface layers [128, 129] and hence the measured carrier concentration value in H-doped ZnO could be due to hydrogen related shallow donors [130]. The large increase in carrier concentration after hydrogen doping suggests high concentration of hydrogen related donors in the near surface region.

4.4 Optical Properties of Hydrogen doped ZnO

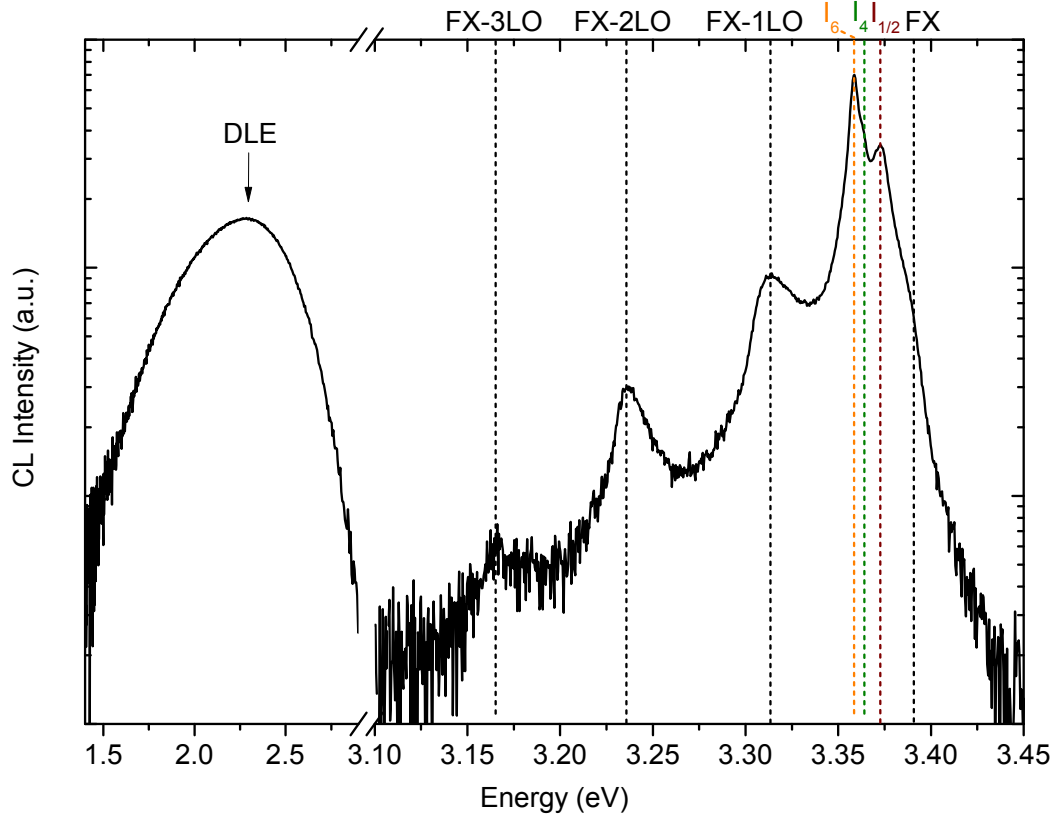


Figure 4.3: CL spectrum of as-received ZnO showing the FX, BX, FX-1LO, FX-2LO, FX-3LO and the broad deep level emission centered at 2.3 eV. Note the different scale on the energy axis between the NBE and DLE regions. This spectrum was collected at 80 K with beam energy of 5 keV and beam current of 15 nA taken at 80 K.

Figure 4.3 shows the CL spectrum from the as-received *a*-plane ZnO crystal from MTI Corporation collected at 80 K with beam energy of 5 keV and beam current of 15 nA. This beam energy of 5 keV corresponds to an excitation depth of ~ 100 nm in ZnO. This interaction volume is comparable to the sampling depth in PL measurements.

The spectrum consists of two distinct luminescence regions; the near band edge (NBE) in the UV region and a broad deep level emission (DLE) in the visible. The NBE emission is made up of a series of peaks in the region from 3.15 eV to 3.40 eV.

The weak shoulder at 3.39 eV is attributed to free exciton (FX) recombinations. A series of peaks in the region from 3.35 eV to 3.38 eV are attributed to radiative recombination of excitons bound to shallow donors (D^0X or D^+X). The main features in this region are the I_6 peak at 3.359 eV, the $I_{1/2}$ at 3.373 eV and a shoulder at 3.363 eV which is attributed to the I_4 . Three additional peaks on the low energy side of the bound exciton (BX) labeled FX-1LO, FX-2LO and FX-3LO are also observed. The separation of these peaks is consistent with the longitudinal optical (LO) phonon mode in ZnO of 72 meV [131, 132], so these peaks are attributed to the first three phonon replica of the free exciton emission.

The CL emission of the crystal also shows a broad deep-level luminescence peaking at 2.35 eV. This peak is often called the deep level emission (DLE). The origin of this DLE peak is controversial but is often attributed to radiative recombination of electron-hole pairs at native defect sites such as V_O and V_{Zn} or impurities such as copper [49, 102]. Experimental evidence shows that copper impurities result in a fine structure within photoluminescence spectra at liquid helium temperature. The transition from (Cu^+, h) to the $Cu^{2+} T_2$ state results in a photon with the zero-phonon line of the emission at 2.86 eV [61]. Figure 4.4 shows the CL spectrum of the as-received ZnO taken at 10 K. The structureless profile of the DLE in the a -plane MTI crystals at 10 K suggests that the emission is not due to copper impurities, but originates from native defects [133]. The broad profile of the DLE when compared to the NBE emission can be explained in terms of the high coupling of the emission to lattice vibrations [134]. This leads to peak broadening through phonon emissions. The defect emission is broad and centred at 2.35 eV. The broad profile of the defect emission and the multitude of emissions in the DLE region make assignment of individual contributions difficult.

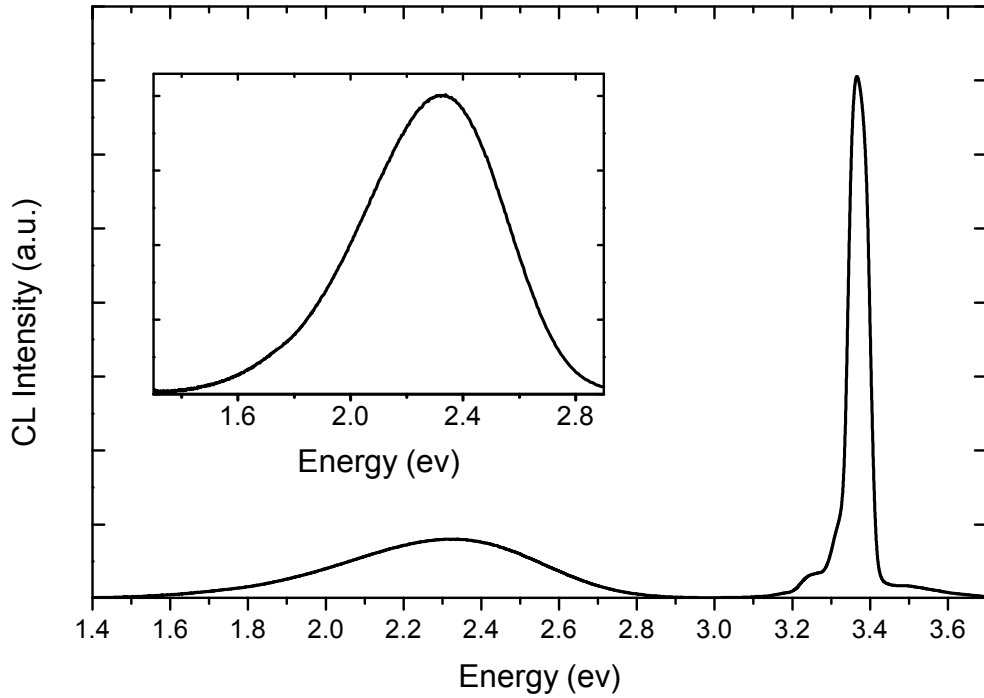


Figure 4.4: CL spectrum of as-received ZnO at 10 K. Inset shows a magnified view of the structureless DLE. Collected with beam energy of 5 keV and beam current of 15 nA.

4.4.1 Effects of Hydrogen on the NBE luminescence

Figure 4.5 shows the CL spectra of both the as-received and H-doped crystals after 2 minutes plasma treatment. It is clear that hydrogen doping has a significant effect on the CL of ZnO. The intensity of the NBE emission is doubled following hydrogen incorporation. A broadening of the bound exciton emission peaks is also observed. However, the spectral resolution of the CL system did not allow for proper investigation of the effects of hydrogen on individual peaks in the NBE region.

There are three possible mechanisms by which the NBE intensity can increase after hydrogen treatment:

1. formation of new shallow donor levels, e.g. H_1 , which provide additional efficient radiative recombination channels through the I_4 channel.

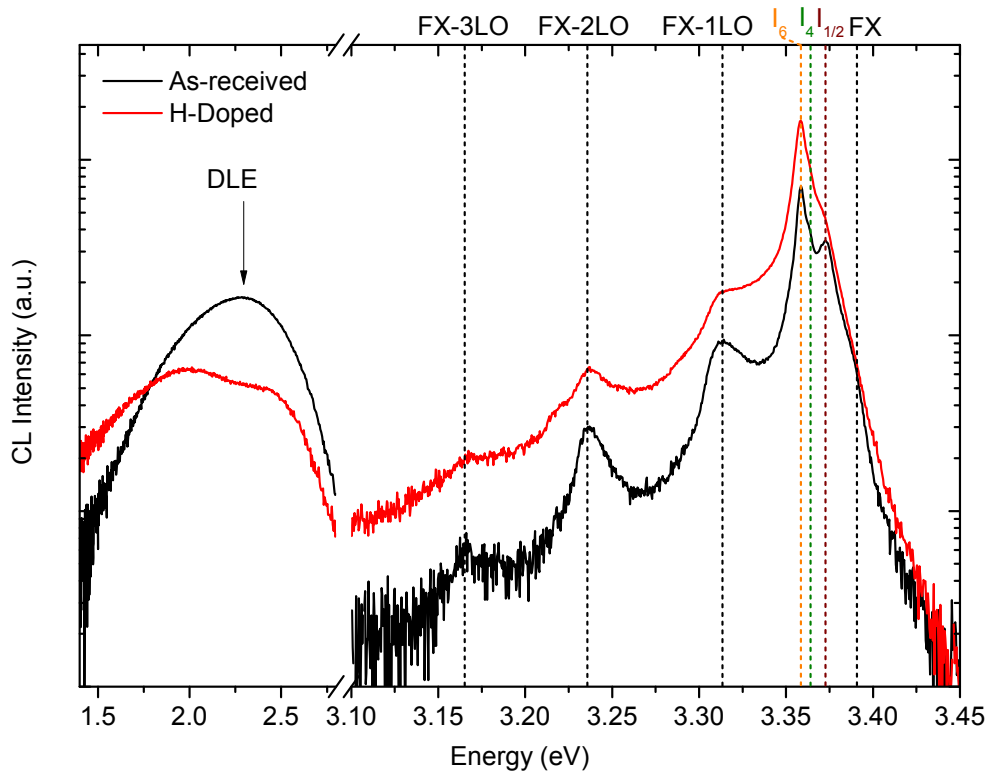


Figure 4.5: Comparison of the CL spectra of as-received and H-doped ZnO after 2 minutes H_2 plasma. Both spectra were collected at 80 K with a beam energy of 5 keV and beam current of 15 nA.

2. elimination of competitive radiative recombination channels by the formation of neutral hydrogen complexes with defect centres.
3. formation of other defect related luminescence centres as a result of damage caused by the hydrogen plasma.

Hall measurements (see Section 4.3) show an increase in carrier concentration by two orders of magnitude. This indicates either formation of new shallow donor levels or passivation of defects and charge traps by the introduction of hydrogen, leading to the increase of the NBE emission and carrier concentration.

In order to investigate the effects hydrogen had on the bound excitons and phonons, high resolution photoluminescence was performed. Figure 4.6 shows the low temperature ($T = 7$ K) PL spectra of the NBE region of both the as-received and H-doped crystals. The inset shows the donor bound exciton region

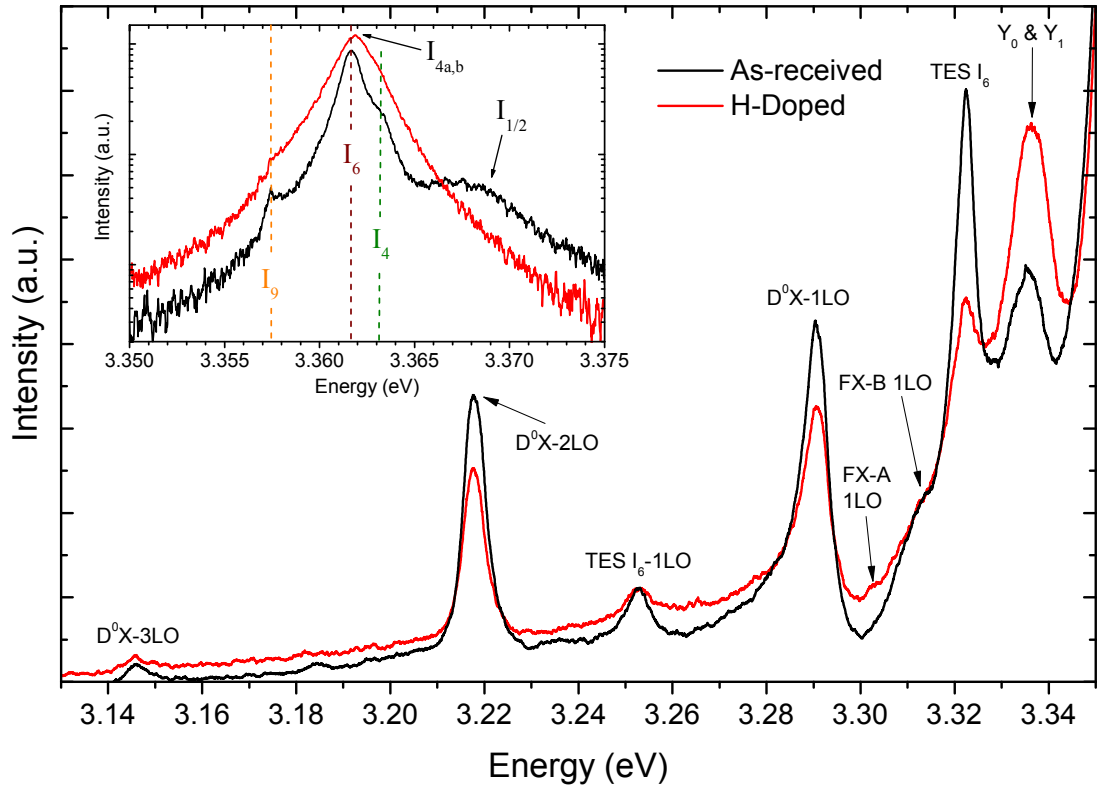


Figure 4.6: High resolution PL spectra of the as-received and H-doped ZnO crystals taken at 7 K. The inset shows the donor bound exciton region of the spectra on a logarithmic scale.

where the I lines are found. The main peak in the as-received crystal is the I_6 line at 3.616 eV. Also present are the I_9 line at 3.357 eV, the I_4 at 3.363 eV and a broad luminescence centred at 3.368 eV. Of particular interest is the I_4 line which is taken as a signature for hydrogen shallow donors in ZnO [27, 89, 95]. The intensity of the I_4 line is increased following hydrogen incorporation and a slight blue shift of the main peak is observed. For H-doped ZnO, the dominant peak at 3.362 eV (labelled $I_{4a,b}$) has previously been attributed to an excited state of the H-related neutral donor bound exciton I_4 [135]. Analysis of the BX spectral region reveals that the $I_{4a,b}$ intensity increases in comparison with that of I_4 after hydrogen incorporation suggesting that hydrogen dopants introduced by the plasma are in a different chemical state to those incorporated during the hydrothermal growth. This is consistent with the CL results and can be interpreted as hydrogen forming new shallow donors which act as efficient radiative

recombination pathways. The broad luminescence at 3.368 eV, which is where the I_2 or I_1 lines are expected to be, has also been attributed to an emission from the “bottleneck” region of the lower polariton branch of the A valence band (LPB_A) [131]. This assignment is unlikely as the intensity of that emission is expected to increase with carrier concentration. It can be seen that the emission is quenched following hydrogen doping. It has also been reported that the I_2 at 3.368 eV appears in ZnO following lithium doping and has been attributed to lithium interstitial (Li_i) shallow donors [27, 136]. This Li_i can then be passivated by hydrogen, leading to the quenching of the luminescence.

The intensity of the phonon replica of the D^0X emission at 3.2903 eV and 3.2180 eV as well as that of the two-electron satellite (TES) of the I_6 at 3.2527 eV are reduced after hydrogen incorporation. Conversely, the peak at 3.3363 eV is enhanced after hydrogen incorporation. This peak is at the position where the Y_0 and Y_1 lines are to be expected. The origin of the Y lines is still controversial, but has recently been attributed to the radiative recombination of excitons bound to extended structural defects [137]. Such defects could have been created in the crystal when exposed to the hydrogen plasma.

4.4.2 Effects of Hydrogen on the DLE

In addition to an increase in the NBE emission, hydrogen doping also affects the DLE as observed in Figure 4.5. The intensity of the DLE peak is reduced and is separated into two components: one yellow luminescence centered at ~ 1.9 eV [50] which is associated to a donor-acceptor pair recombination involving a deep lithium acceptor occupying a Zn site (Li_{Zn}) and a green luminescence centered at ~ 2.35 eV whose origin has been attributed to bulk zinc vacancies (V_{Zn}) [39] or surface oxygen vacancies (V_{O}) [40]. Zinc vacancies are double acceptors and occur in the 2- charge state ($\text{V}_{\text{Zn}}^{2-}$). Hydrogen, known to act almost exclusively as positive charge state (H^+) [86], would preferentially interact with $\text{V}_{\text{Zn}}^{2-}$ rather than

V_{O}^+ or V_{O}^{++} centres. This assignment is in agreement with first principle calculations which predict the existence of a complex involving V_{Zn}^{2-} and two hydrogen atoms [99]. These $V_{\text{Zn}}\text{-H}_2$ inhibit the involvement of V_{Zn} in radiative recombination, thereby quenching the green luminescence. The increase in the intensity of the yellow luminescence can be attributed to the quenching of the green luminescence. As there are a finite number of electron-hole pairs being generated at any given time, recombination preference is given to the most efficient channel [138]. By quenching the green luminescence radiative pathway, the probability of a radiative recombination occurring through the yellow luminescence pathway increases.

4.4.3 Effects of Temperature on Hydrogen Incorporation

The temperature at which the sample is kept during hydrogen plasma treatment has significant effects on the optical properties of the crystals near-surface region as shown in Figure 4.7. The spectra were taken at 80 K with a beam energy of 5 keV which corresponds to a CL generation depth of 100 nm and a beam current of 15 nA. The as-received crystal shows well defined bound exciton peaks and a broad deep level luminescence centered at 2.31 eV (see beginning of Section 4.4 for a discussion on the peaks).

After hydrogen doping at 25 °C, the intensity of the NBE emission is doubled as seen in Figure 4.7. A broadening of the emission peaks is also observed. This broadening suggests that damage to the surface is caused by the hydrogen plasma through sputtering of the surface atoms. An enhancement of the emission at 3.333 eV is observed after hydrogen doping. That spectral position corresponds to a *Y* line as shown in the PL measurements before. The DLE was red-shifted from 2.32 eV to 1.97 eV after hydrogen doping. This apparent shift in the peak position is due to the quenching of the GL by hydrogen which forms neutral $V_{\text{Zn}}\text{-H}_2$ complexes that passivate the native V_{Zn} which are responsible for the

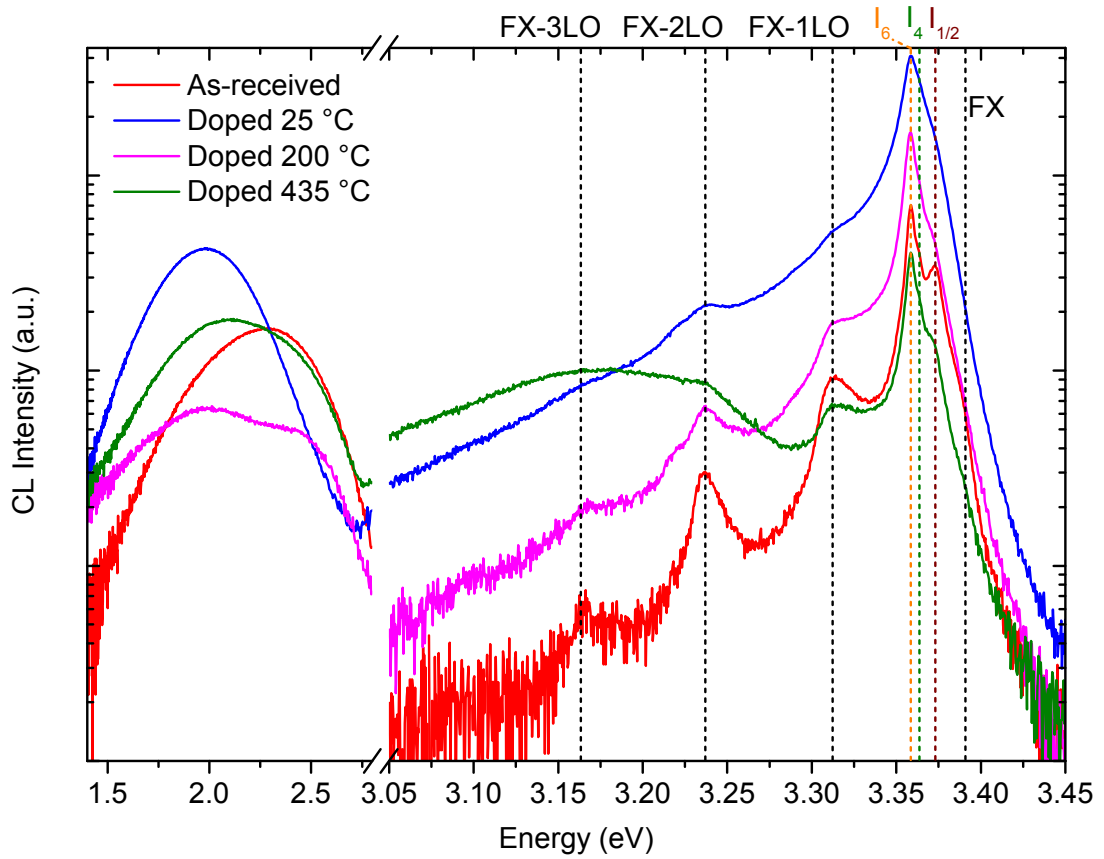


Figure 4.7: CL spectra of as-received and H-doped ZnO crystals with the doping procedure performed at various temperatures. The plasma exposure time was kept at 120 s for the doped crystals. All spectra were collected at 80 K with beam energy of 5 keV and beam current of 15 nA.

GL. The quenching of the GL implies that hydrogen has enough thermal energy at 25 °C to diffuse in the crystal to form a $V_{Zn}-H_2$ complex which requires two hydrogen sitting at the zinc vacancy site. It is accepted that the YL in ZnO is caused by a radiative recombination of a donor-acceptor pair involving a shallow donor and a Li_{Zn} acceptor. The relative increase in the YL after hydrogen incorporation can be explained in terms of competition for carriers in CL. When the GL pathway was quenched, the probability of a radiative recombination via the channels responsible for the YL increased. Another possibility is that hydrogen incorporation increases the donor concentration in the vicinity of Li_{Zn} centres, thereby making the DAP luminescence pathway more efficient.

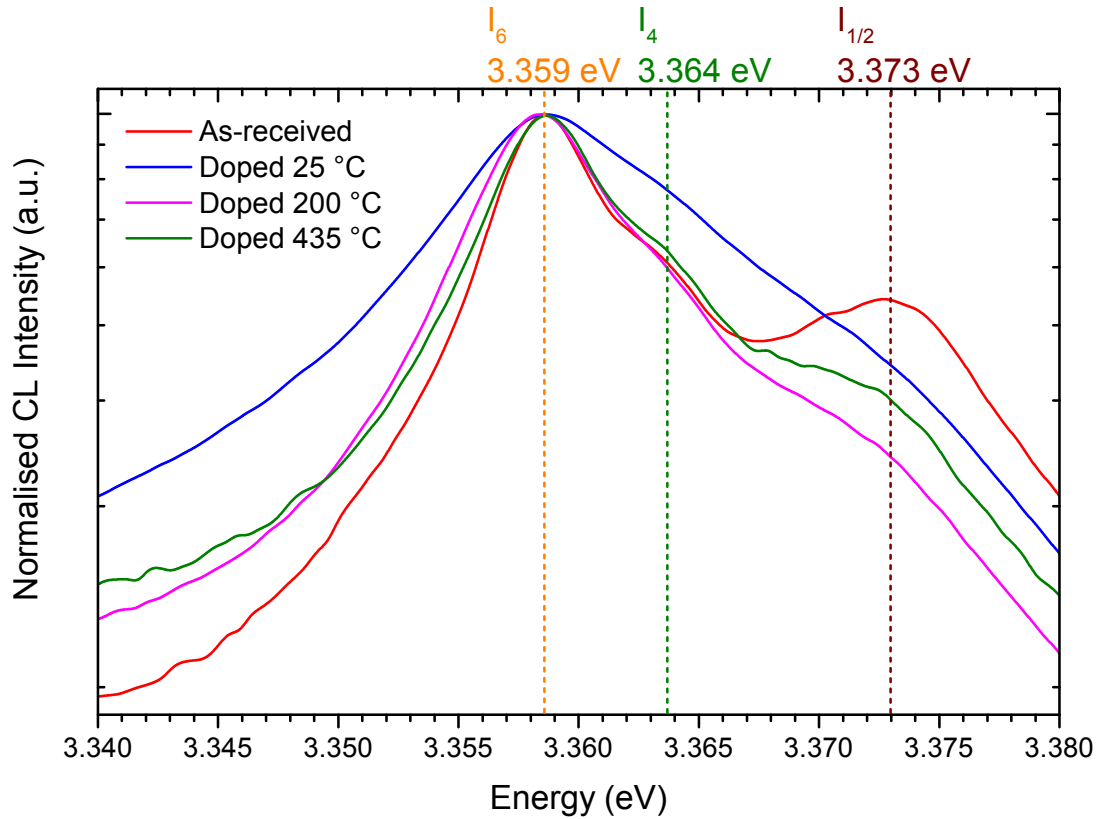


Figure 4.8: Normalised CL spectra of the bound exciton region. Spectra were normalised to the I_9 line. All spectra were collected at 80 K with beam energy of 5 keV and beam current of 15 nA.

For doping performed at 200 °C, the intensity of the NBE emission is increased compared to the as-received crystal, but is lower than when doping was performed at 25 °C as shown in Figure 4.7. The emission peaks are also narrower and more defined. The narrowing of the line width is synonymous with an improved crystal quality caused by the higher temperature of the crystal during hydrogen incorporation. This is in effect a low temperature annealing of the crystal. Further support for this explanation is the decrease of the Y line emission at 3.333 eV. The overall intensity of the NBE emission being reduced when compared to the plasma treatment done at 25 °C as in Figure 4.8 can be caused by two factors: (1) hydrogen diffusing from the near-surface layer deep into the bulk or (2) hydrogen being removed from the surface at the higher temperature. Previous reports have found that hydrogen is stable in ZnO at temperatures of up to ~ 500 °C [85, 95].

The lower temperature involved in this case would imply diffusion of hydrogen deeper in the bulk. This also explains the decrease of the NBE intensity when compared to the sample at 25 °C. Similar to the 25 °C case, the GL was decreased. However, the effect was less significant. Hydrogen has higher thermal energy at 200 °C than at 25 °C and hence can travel deeper in the bulk before interacting with native defects such as V_{Zn} .

At 400 °C the crystal seems to be more damaged by the hydrogen plasma. At such high temperatures, it is expected that sputtering of the surface Zn or O atoms by hydrogen species takes place more easily. This damage can be seen in Figure 4.7 as a broad luminescence centered at ~ 3.15 eV and a decrease in the NBE intensity when compared to the as-received crystal. The intensity of the GL has not changed when compared to the as-received sample while that of the YL was slightly increased.

While low voltage CL gives information of the crystals near surface regions, it is necessary to perform depth dependent CL to have a better idea of hydrogen incorporation and diffusion. The DLE is also made up of two distinct emissions, the green and the yellow emission. It is therefore necessary to deconvolve the broad peak centered at 2.31 eV into two components for proper analysis.

4.4.4 Deconvolution of the Deep-Level Luminescence Band

The DLE peak in ZnO consists of at least two distinct emissions (Figure 4.5). One in the green region attributed to V_{Zn} and a yellow component attributed to Li_{Zn} . In order to investigate these components and find fit parameters, an as-received ZnO crystal was doped with lithium. A 50 nm layer of lithium metal was thermally evaporated on a clean *a*-plane ZnO crystal surface in a vacuum. The coated crystal was then annealed in-situ in the deposition chamber for 30 min at 950 °C to indiffuse lithium acceptors in the crystal. Figure 4.9 shows the XPS

spectra of the Li 1s core level for both the as-received and Li doped crystals taken at an X-ray photon energy of 160 eV. A peak at binding energy of 54.7 eV appears in the Li doped crystal. This indicates that Li has been incorporated in the ZnO crystals.

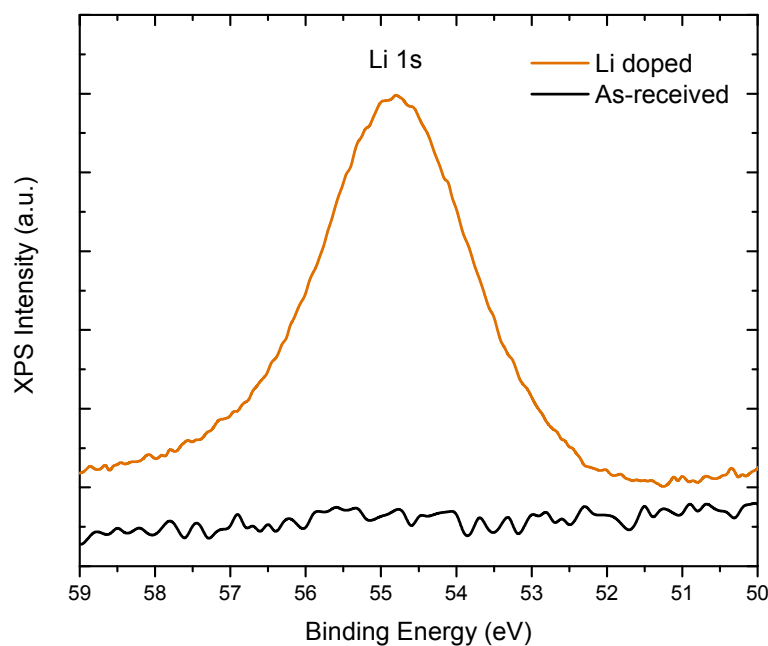


Figure 4.9: XPS spectra of the Li 1s core level for the as-received and Li doped crystals taken at a photon energy of 160 eV.

Figure 4.10 shows the CL spectrum of the yellow emission in the Li doped ZnO crystal taken at 80 K. The Li-doped ZnO displays deep level emission dominated by the yellow luminescence. The yellow luminescence in ZnO is known to couple strongly with phonons in the lattice and it has been reported to have a Huang-Rhys factor of $S = 13$ [139]. This large Huang-Rhys factor indicates that the peak is symmetrical and can therefore be fit with a single Gaussian function [134]. A least square Gaussian fit of the yellow luminescence resulted in a peak centered at 1.95 eV with a full width at half maximum (FWHM) of 0.58 eV.

Tying down the peak energy and FWHM parameters for the yellow luminescence and letting the green luminescence fit accordingly means that a unique fit is achieved every time. Figure 4.11 shows such a deconvolution with two Gaussian

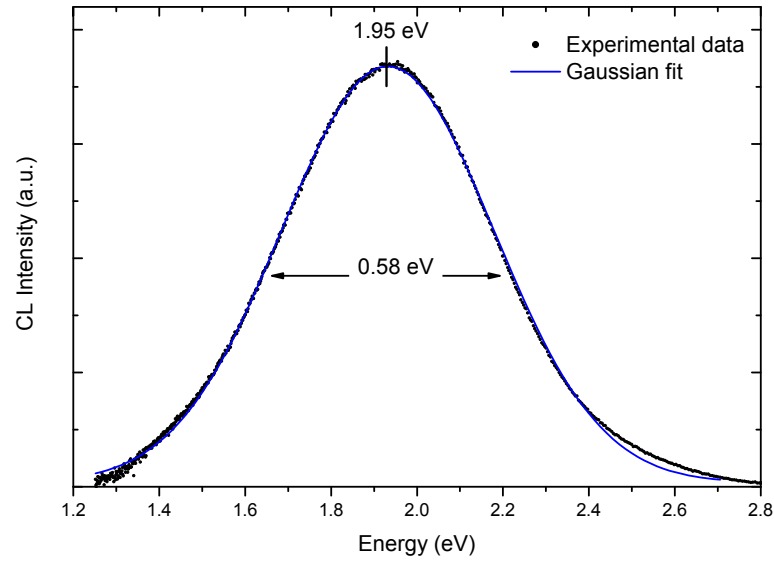


Figure 4.10: CL spectrum of the Li doped crystal showing the least square Gaussian fit of emission. Peak position at 1.95 eV and FWHM of 0.58 eV. Spectrum was collected at 80 K with beam energy of 15 keV and beam current of 4 nA

components and a fit to the DLE achieved by a non-linear least square fitting algorithm. This fit yielded the parameters for the GL of peak position at 2.35 eV and FWHM of 0.51 eV.

The fit parameters for the yellow and green luminescences used in this project are summarised in Table 4.2. When comparing the contribution of different emission in depth or power resolved experiments, the integrated intensity of the deconvolved peaks were used instead of peak height. For the NBE emission, the whole integrated intensity of the region from 3 eV to 3.4 eV was used.

Table 4.2: Fit parameters for the yellow and green luminescences obtained by least square Gaussian fits

| Peak | Peak Position | FWHM |
|---------------------|---------------|---------|
| Yellow luminescence | 1.95 eV | 0.58 eV |
| Green luminescence | 2.35 eV | 0.51 eV |

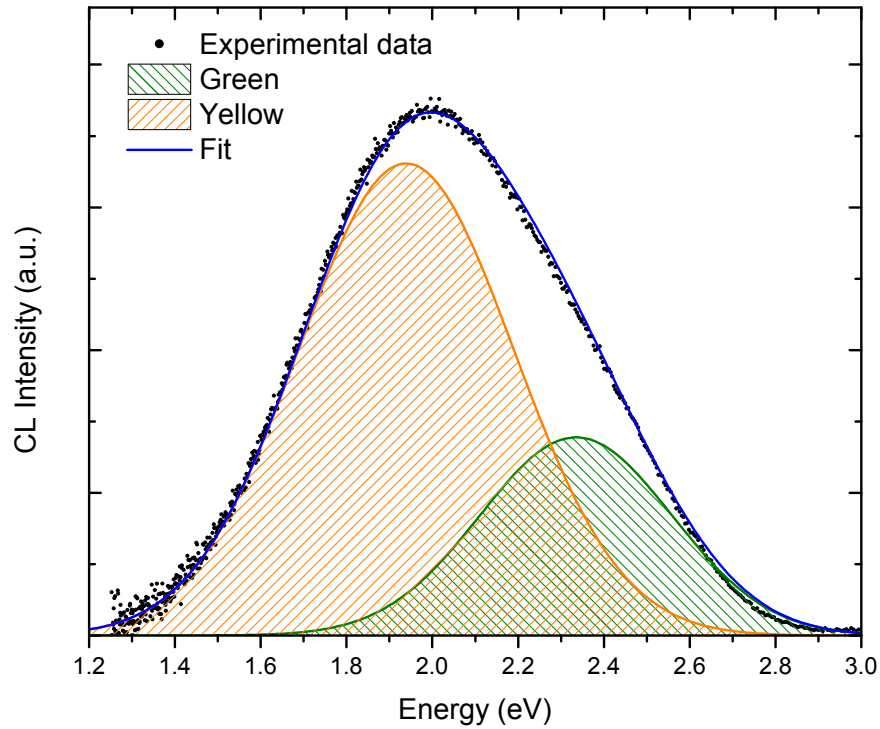


Figure 4.11: The DLE peak of ZnO has been deconvolved into two Gaussian components. The yellow component at 1.95 eV with FWHM of 0.58 eV and the green component at 2.35 eV with FWHM of 0.51 eV.

4.4.5 Depth Distribution of Luminescence Centres

As the energy of the beam determines the penetration depth of electrons, and consequently the depth at which CL is generated, it is possible to control the depth at which CL is generated. The number of electron-hole pairs generated is proportional to the beam power and can be approximated by the following equation [138]:

$$[n]_{eh} \propto I_b \cdot E_b \quad (4.1)$$

where $[n]_{eh}$ is the number of electron-hole pairs generated, I_b is the beam current and E_b is the beam energy. By varying both the beam current and beam energy to keep the power constant, it is possible to obtain information on the depth distributions of a luminescence centre such as a defect. For example, if CL is collected at low beam energies, information about the surface is collected, while

increasing the beam energy gives more information about the bulk properties of the sample.

One limitation of this technique is the higher energy tail of band-edge luminescence from semiconductors can be readily re-absorbed by the material itself, leading to an apparent red-shift. The emitted light intensity follows a Beer-Lambert relation [140]:

$$I = I_0 \exp(-\alpha d) \quad (4.2)$$

where α is the absorption coefficient and d is the photon generation depth. This self-absorption effect is more pronounced when high beam energies are used i.e. photons are generated at depths of several micrometres below the surface.

4.4.5.1 Simulations of CL Interaction Volumes in ZnO

The penetration depth and consequently the interaction volume of an electron beam depends on the beam energy. In order to correlate the beam energy to CL generation depth, the CASINO package [111] was used for Monte Carlo simulations of the electron beam interaction with ZnO material.

Figure 4.12 shows the typical shape of the energy loss profile of electrons in ZnO as obtained from the CASINO simulations. The energy loss curve data was obtained from CASINO simulations using the parameters in Table 3.2. At low accelerating voltages most of the energy is dissipated within a small volume. At higher beam energies the tail of the energy loss curve decays deep into the sample. As a result, maximum penetration depths give a poor indication of CL generation. Simulations have been done for the primary beam energy range of 0.1 keV to 30 keV. It is generally accepted that the CL generation depth is taken as the depth at which 75% of the energy is dissipated under the energy loss profile. Figure 4.13 shows the CL generation depth which has been calculated by integrating over the simulated energy loss curves.

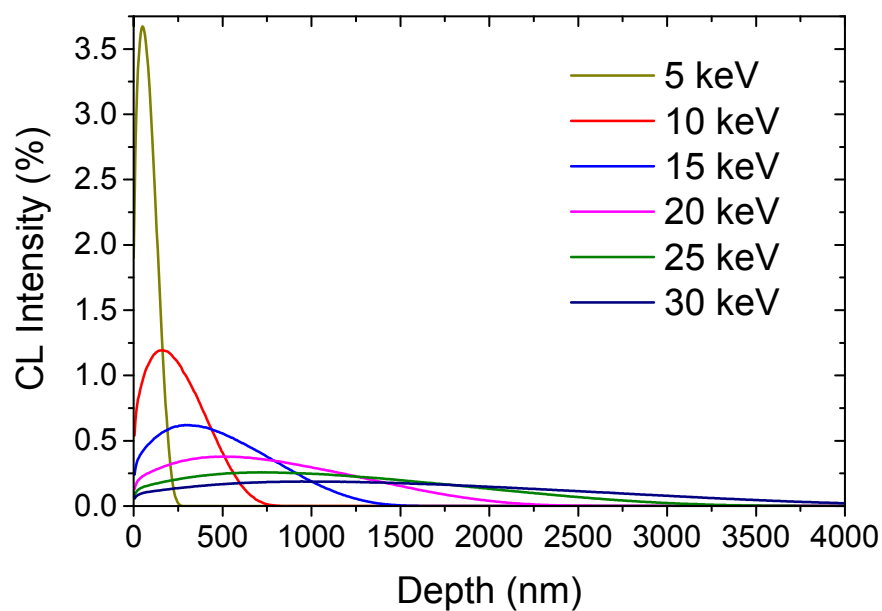


Figure 4.12: CASINO simulated electron energy loss curves for beam energies of 5 keV, 10 keV, 15 keV, 20 keV, 25 keV and 30 keV. The vertical axis corresponds to the percentage of CL generated at that particular depth.

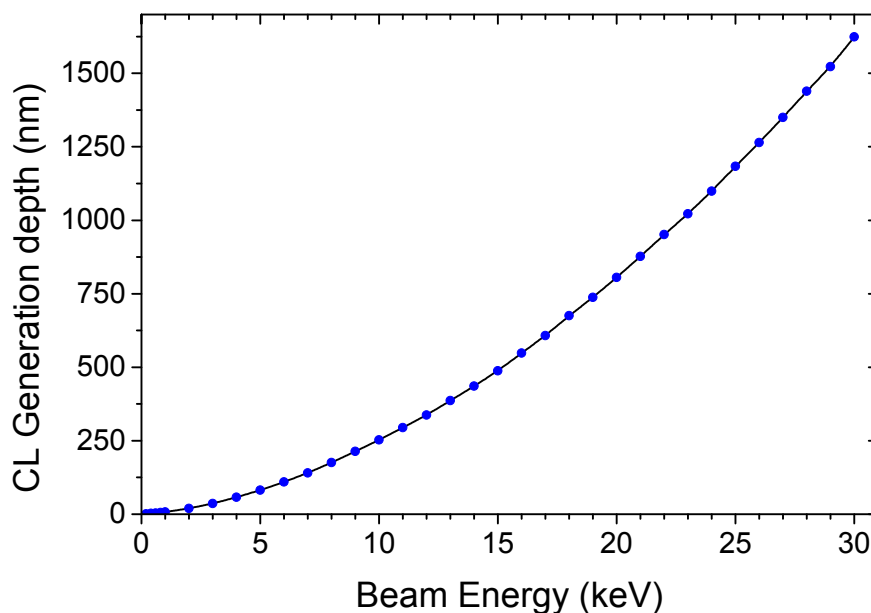


Figure 4.13: CL generation depth as a function of electron beam energy. The depth here corresponds to the depth at which 75% of the electron beam energy has been lost.

4.4.5.2 Distribution of Luminescence Centres in H-doped ZnO

Depth-resolved cathodoluminescence (DRCL) was used to determine the spatial distribution of luminescence centres from the surface of the crystal. By correlating electron beam energies to electron interaction volumes obtained from CASINO simulations (Section 4.4.5.1), it is possible to estimate the depth at which the CL signal is generated. In DRCL, the beam power is kept constant by varying both the beam energy and current at the same time. It is therefore expected that the number of electron-hole pairs generated in each scan to be constant. In this ideal case with a homogeneous distribution of luminescence centres throughout the depth of the sample and neglecting surface recombinations, a flat horizontal line with constant intensity, which represents the integrated area of the luminescence peaks, is expected.

Figure 4.14 shows the DRCL spectra for the as-received and H-doped crystals where doping was performed at 25, 200 and 435 °C. The DRCL spectra represent the integrated area under the respective CL spectra for each luminescence band. The beam power was kept constant at 30 μ W throughout all acquired scans. In all samples, for beam energies of $E_b < 2$ keV, which corresponds to a layer of about 30 nm, no CL emission was observed. This is due to non-radiative defects caused by surface polishing damage completely quenching any luminescence [141]. For the as-received ZnO sample, the NBE emission rapidly increases after the first 2 keV to reach a maximum at a depth of 170 nm. With higher beam energies, the NBE emission is constant and does not show any self-absorption effects (See Equation 4.2). This shows that DRCL is a valid technique to use for the study of light emission from different depths of a sample.

The NBE luminescence of the ZnO crystals is significantly changed after hydrogen incorporation. For the sample doped at 25 °C, the maximum NBE intensity was increased by one order of magnitude when compared to the as-received sample as in Figure 4.14 (a). The NBE intensity rises quickly from 2 keV to peak at

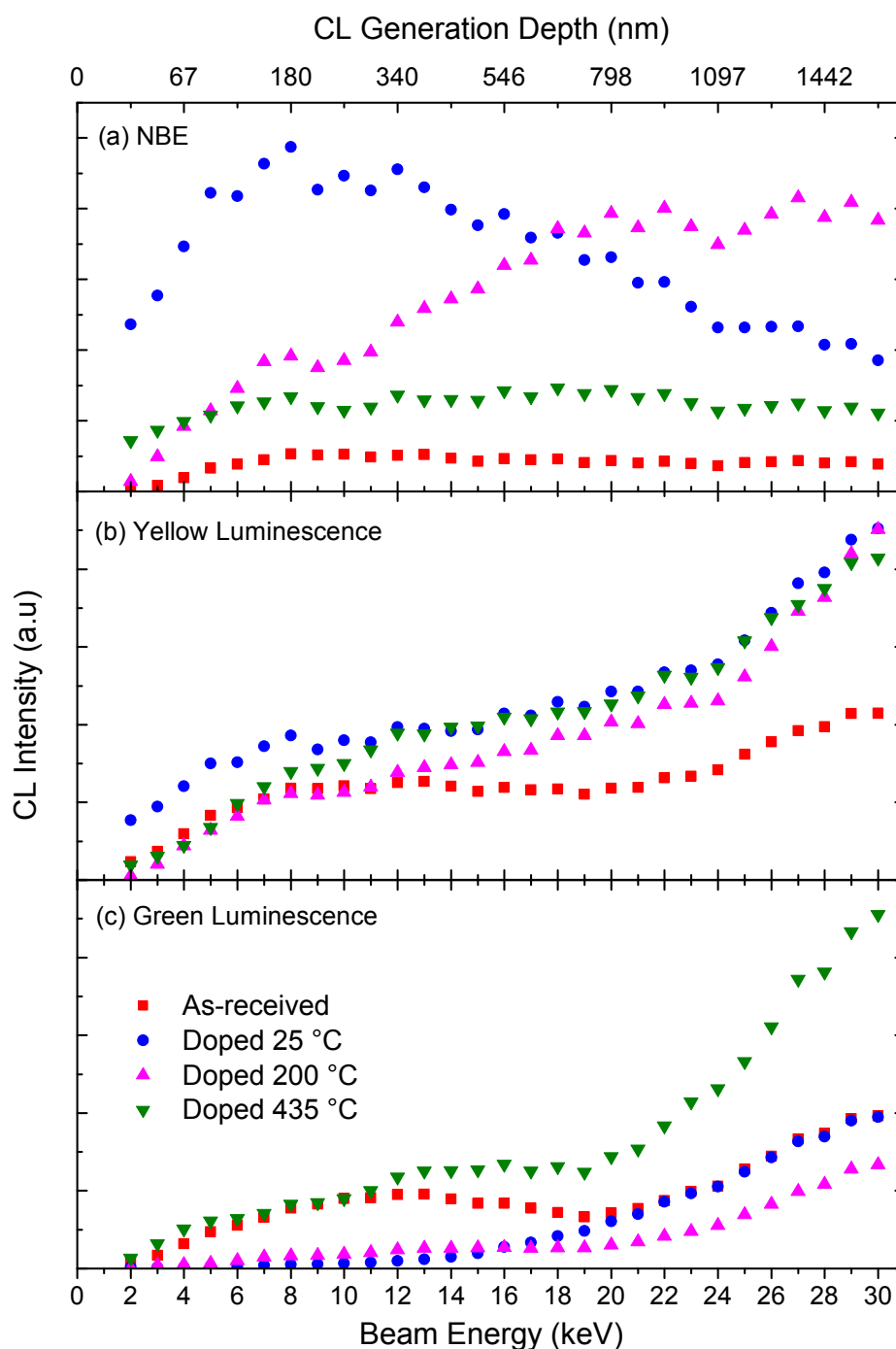


Figure 4.14: Distribution of luminescence centres in as-received ZnO and H-doped ZnO crystals at different temperatures. Integrated intensity for (a) NBE emission, (b) yellow luminescence and (c) green luminescence are shown from 2 keV to 30 keV. Spectra were collected at 80 K with a beam power of 30 μ W. The top x -axis is the CL generation depth in ZnO corresponding to 75% CL intensity obtained by CASINO simulations.

10 keV which corresponds to a CL generation depth of ~ 250 nm and then drops for higher beam energies. The enhancement of the NBE is consistent with the formation of new H_i shallow donors in the near surface region. In fact, the depth profile of the NBE luminescence can be used to approximate the distribution of hydrogen donors incorporated in the crystal by the plasma treatment.

Hydrogen doping (Figure 4.14 (c)) causes the GL to be quenched in the top 500 nm of the crystal. The intensity of the GL then increases until it reaches the same profile as the as-received crystal at 900 nm depth. The discrepancy between the NBE and GL profile is due to the fact that hydrogen is more likely to stay as single H_i than interact with native defects to form $V_{Zn}-H_2$ complexes, specially when the concentration of H_i is low which is the case at depths below 900 nm. The reduction in the green intensity is fairly constant within the depth range 30 nm to 800 nm, indicating a uniform hydrogen concentration, in good agreement with other types of depth profiling measurements [123]. The fact that the green luminescence is quenched at depths reaching several μm in the bulk demonstrates that surface oxygen vacancies cannot be the source of the green luminescence but that they most likely originate from bulk zinc vacancies. The YL is enhanced throughout the whole sampling range because of the quenching of the GL.

Increasing the temperature at which the ZnO crystal was kept at during hydrogen incorporation from 25°C to 200°C increases the diffusion of hydrogen deeper in the bulk. In Figure 4.14 (a), it can be seen that the peak of NBE luminescence occurs at 1000 nm, increasing from 250 nm when the temperature was increased. This is consistent with hydrogen species having higher thermal energy (from 25 meV to 42 meV) and can therefore diffuse deeper in the bulk. This behaviour can also be seen in the GL depth profile from Figure 4.14 (c). The GL is still quenched in the near surface region, but at depths deeper than 900 nm the intensity of the GL in the H-doped crystal is still lower than the as-received.

This is in contrast to when hydrogen doping was performed at 25 °C. The profile shows that hydrogen has indeed diffused deeper at 200 °C than at 25 °C.

For the crystal doped at 435 °C, the apparent increase of the NBE luminescence when compared to the as-received crystal is not due to hydrogen but caused by the formation of the new band at 3.15 eV as shown in Figure 4.7. The profile of the NBE also suggests that no hydrogen has been incorporated in the form of H_i donors. It is possible that the higher temperature of 435 °C is more favourable for the removal of hydrogen from the crystal than its incorporation. The depth profiles of both the YL and GL follow the as-received crystal in the near surface region, but increase with depths below 200 nm. The fact that the GL does not show any quenching effects means that $V_{Zn}-H_2$ complexes were not formed because hydrogen was not incorporated in the crystal at that temperature.

4.4.6 Effect of Plasma Exposure Time on the Luminescence

To optimise the emission efficiency of the crystals through hydrogen doping, the CL intensity was monitored as a function of plasma exposure time with the sample kept at 25 °C. The deconvolved CL emission from the NBE, yellow and green emissions are shown in Figure 4.15. The NBE intensity increases by about one order of magnitude after 120 s then shows a decrease in intensity with further plasma exposure. This decrease could be due to damage in the crystal caused by removal of atoms from the surface of the crystal [126, 127]. Another possible explanation is the formation of hydrogen molecules (H_2) at high concentration of H_i [90, 142]. H_2 being a neutral impurity, does not take part in radiative recombination and hence leads to a decrease in the D^0X emission.

The intensity of the green luminescence is halved after 120 s. The emission is not quenched entirely because the depth of the interaction volume is bigger than

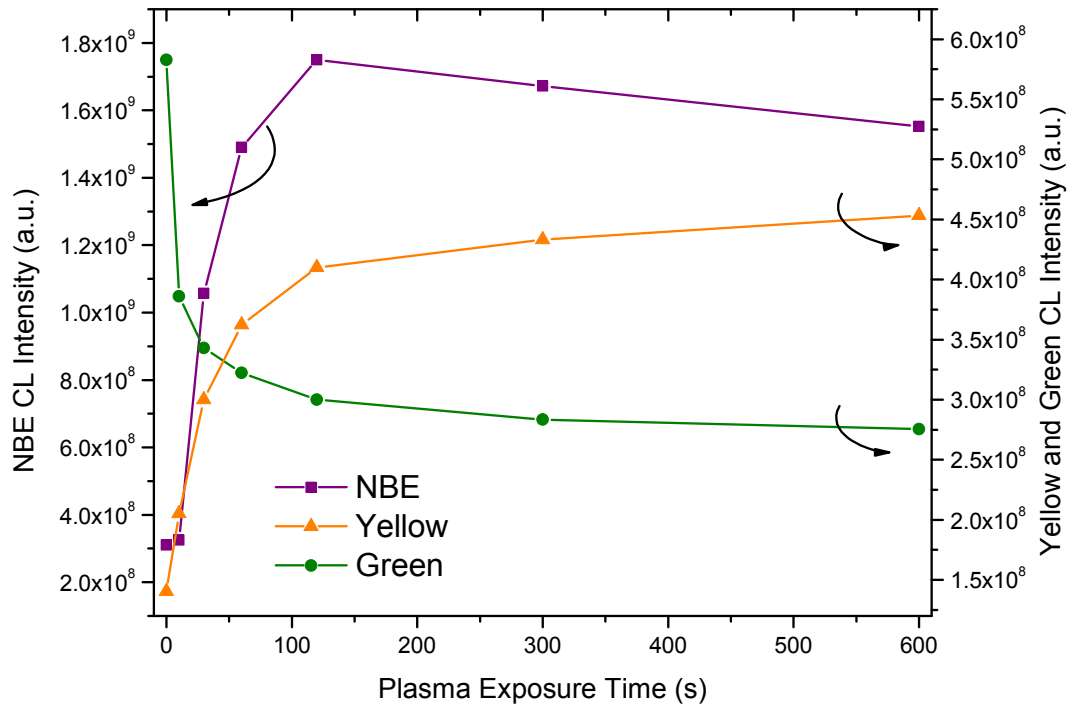


Figure 4.15: Integrated intensity of the NBE, yellow and green emissions as a function of hydrogen plasma exposure time. Spectra were collected at 80 K with a beam energy of 15 keV and beam current of 2.5 nA.

the depth at which hydrogen was introduced by the plasma. The intensity of green luminescence keeps on decreasing after 120 s due to hydrogen thermally diffusing deeper in the crystal and forming more neutral $V_{Zn}-H_2$. The yellow luminescence is not passivated by hydrogen but instead increases after plasma treatment. The results suggest that H_i donors do not interact with Li_{Zn} . The increase in the intensity of the yellow luminescence is most likely due to the passivation of competitive recombination processes, both radiative (e.g. the green luminescence centres) and non-radiative.

The effects of hydrogen plasma exposure time on the distribution of the luminescence centres were also studied. Figure 4.16 shows the DRCL for the as-received and H-doped ZnO crystals. The intensity of the NBE luminescence is increased

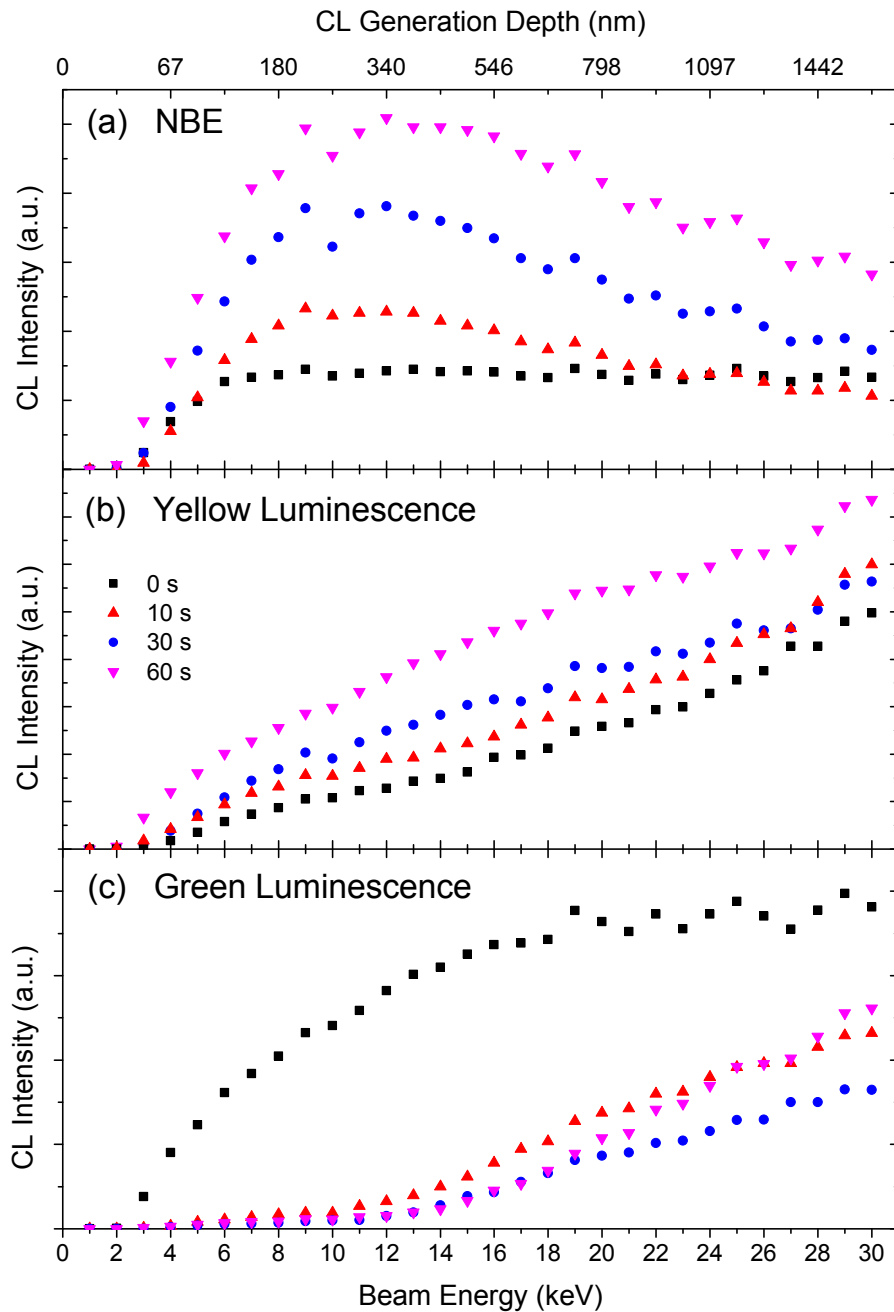


Figure 4.16: Distribution of luminescence centres in ZnO crystals for (a) NBE (b) yellow and (c) green luminescences as a function of hydrogen plasma time. Spectra were collected at 80 K with a beam power of 30 μ W. The top x -axis is the CL generation depth in ZnO corresponding to 75% CL intensity obtained by CASINO simulations.

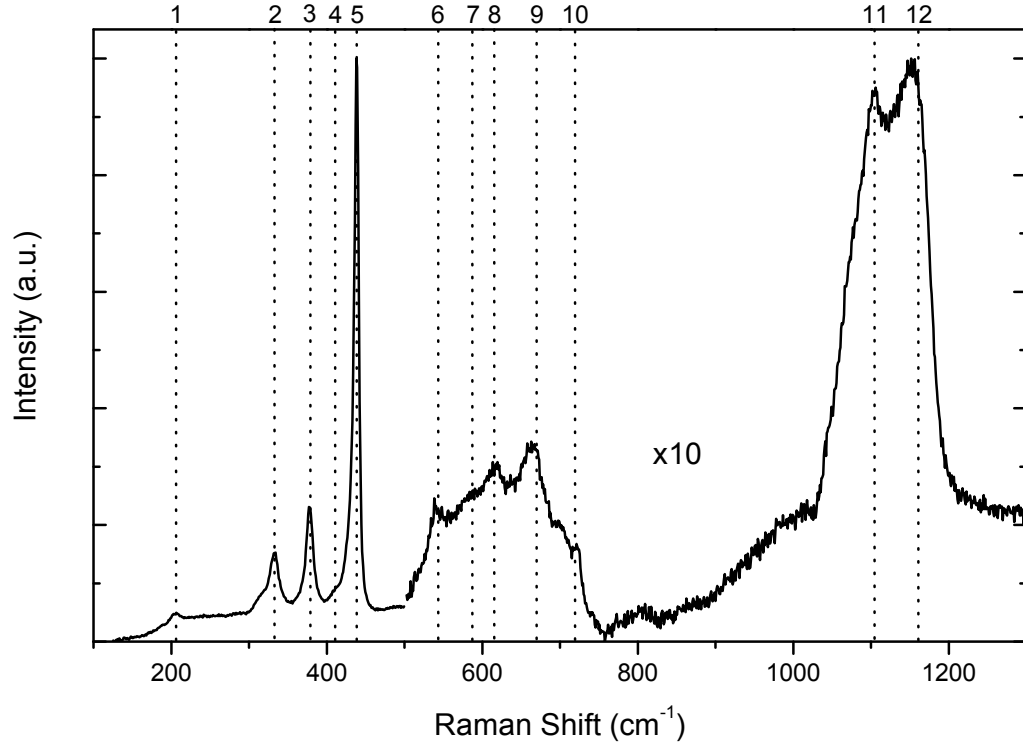
with increasing plasma time. The overall trend of the depth profiles do not change with increasing plasma exposure. Only the intensity is increased. The plasma exposure time dependent green luminescence profiles (Figure 4.16 (c)) show that this luminescence is being quenched after only 10 s of plasma exposure.

This indicates that hydrogen is incorporated at depths up to 350 nm in less than 10 s. With increasing plasma time, the shape of the depth profiles do not change, but the effects of the hydrogen plasma are enhanced. While the surface green luminescence is already mostly quenched in the first 10 s, the intensity of the luminescence keeps on decreasing further in the bulk with plasma time, indicating thermal diffusion of hydrogen deeper in the bulk. This is in agreement with first principle calculations which predict hydrogen to be mobile in ZnO at temperatures as low as 100 °C [106].

4.5 Raman Spectroscopy

Raman spectroscopy was used in this project to investigate any effects that hydrogen could have on the vibrational modes of ZnO. This can be in the forms of formation of new Raman peaks attributed to hydrogen forming bonds with ZnO or forming H₂ molecules. Other spectral changes could be shifts or quenching of native ZnO peaks.

ZnO exists mainly in the hexagonal wurtzite structure with four atoms per unit cell and belongs to the $C_{6v}^4(P6_3mc)$ space group. From the group theory, one will theoretically expect one A_1 , one E_1 , two E_2 , and two B_1 optical phonon modes [116, 144]. Phonon modes of A_1 , E_1 and E_2 symmetry are Raman active while the B_1 mode is silent. The polar characteristics of the A_1 and E_1 vibrational modes give rise to both longitudinal and transverse components. A typical Raman spectrum of the as-received a -plane ZnO crystal is shown in Figure 4.17. Peaks at 205, 332, 378, 438, 540, 584, 615, 670 and 724 cm⁻¹ were clearly observed



| | Raman Shift (cm ⁻¹) | Symmetry | Process |
|----|---------------------------------|------------|------------------------------------------------|
| 1 | 205 | A_1 | 2TA |
| 2 | 332 | E_2, E_1 | $E_2^{\text{high}} - E_2^{\text{low}}$ |
| 3 | 378 | A_1 | $A_1(\text{TO})$ |
| 4 | 410 | E_1 | $E_1(\text{TO})$ |
| 5 | 438 | E_2 | E_2^{high} |
| 6 | 540 | A_1 | $2B_1^{\text{low}}; 2\text{LA}$ |
| 7 | 584 | E_1 | $E_1(\text{LO})$ |
| 8 | 615 | A_1 | TA+TO |
| 9 | 670 | A_1 | TA+TO |
| 10 | 724 | A_1 | TA+TO |
| 11 | 1103 | A_1 | 2LO |
| 12 | 1157 | A_1 | $2A_1(\text{LO}), 2E_1(\text{LO}); 2\text{LO}$ |

Figure 4.17: Raman spectrum for the as-received a -plane single crystal ZnO used in this work taken at 300 K. The intensity of the Raman emission was multiplied by 10 after 500 cm⁻¹. Symmetry of the modes and their assignments are taken from references [116, 117, 143].

in the low frequency region. Moreover, there is a very weak shoulder located at the low energy side of the 438 cm^{-1} peak, which corresponds to the $E_1(\text{TO})$ at 410 cm^{-1} . Further peaks located at 1103 and 1157 cm^{-1} were also found in the high frequency regions. No more high-order peaks could be observed at frequencies over 1200 cm^{-1} . The E_2 peak at 438 cm^{-1} , being the main peak in the Raman spectrum, suggests good crystal quality [145, 146]. The peaks in the Raman spectra along with their corresponding symmetries and processes are summarised in Figure 4.17.

Raman spectroscopy was performed on both the as-received and hydrogen doped crystals. Figure 4.18 shows the Raman spectra for both the as-received and H-doped ZnO crystals. The H-doped crystal shows the same peaks as the as-received one. No peak shifts or additional peaks were found, indicating no changes in the crystal quality. It is worth noting that ZnO is transparent to red light ($\lambda = 633\text{ nm}$) and hence most of the Raman signal comes from the bulk of the material and any surface damage from sputtering of Zn or O atoms from the surface of the crystal would not be clearly seen in the Raman spectra. The intensity of the E_2 peak in both the as-received and H-doped crystals is similar and indicates that hydrogen doping has not degraded the bulk crystal quality. This suggests that any damage done by the hydrogen plasma, such as etching effects (see Section 4.2), is highly localised at the surface of the crystals.

There have been reports of Raman modes associated to hydrogen in ZnO. The appearance of a mode at 3611 cm^{-1} after hydrogen plasma treatment is associated with the stretch mode of the O–H bond of the interstitial bond-centred hydrogen [147]. Other modes at 4145 , 3628 , and 2985 cm^{-1} are associated with vibrational modes of interstitial H_2 , HD and D_2^1 molecules [90]. These modes were however not detected in this work. The main reasons for this could be the difference between acquisition conditions and doping conditions. A red laser ($\lambda = 633\text{ nm}$) was used to perform the Raman measurements while the Raman modes reported

¹D is the deuterium atom which is heavy hydrogen ${}^2_1\text{H}$

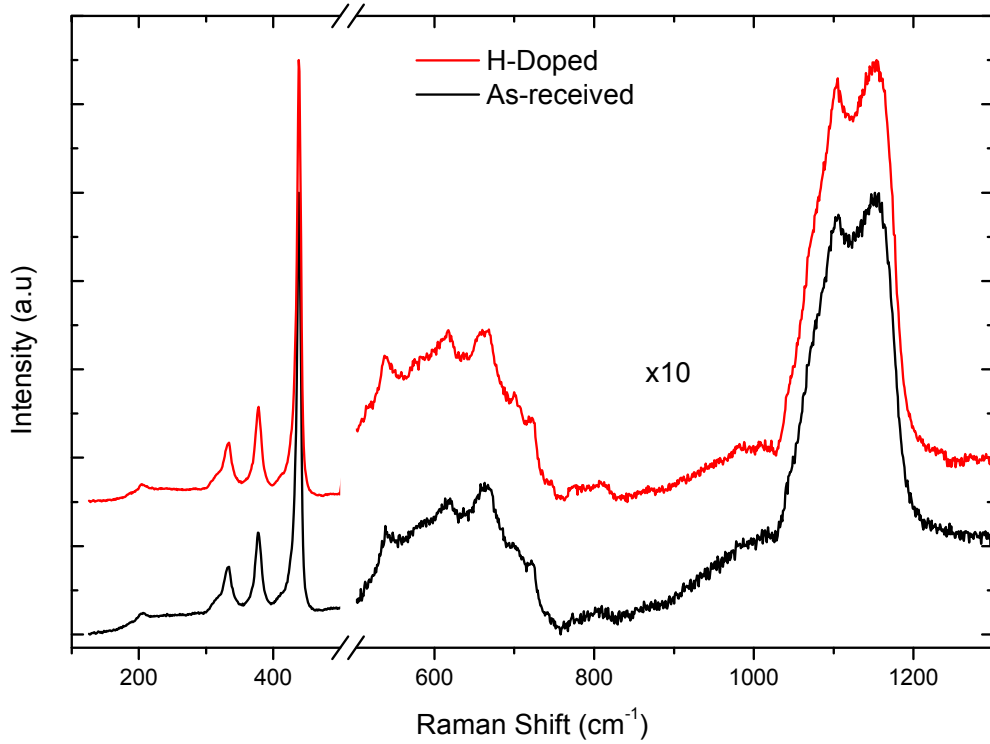


Figure 4.18: Raman spectra for the as-received and H-doped ZnO crystals taken at 300 K. The intensity of the Raman emission was multiplied by 10 for Raman shifts above 500 cm^{-1} . The spectra were offset for clarity.

in literature were performed using a green laser ($\lambda = 532\text{ nm}$). Raman scattering intensity is highly dependent on the excitation wavelength and follows a λ^{-4} relationship [148, 149]. It is highly probable that these hydrogen specific Raman modes are not excited with a red laser and no results have been reported in the open literature where a red laser was used. Moreover, the measurements cited were taken at 4 K while those taken in this work were performed at 300 K. It is possible that those Raman modes are only detected at low temperature.

It is worthwhile noting that those Raman peaks have been reported in H-doped ZnO crystals where the hydrogen was introduced through thermal annealing of the crystals in a hydrogen atmosphere [90, 150]. It is possible that hydrogen has diffused in more uniformly and to a higher concentration by the annealing

procedure than through plasma exposure. It was found in Section 4.4.5.2 that hydrogen diffused to only a few μm from the surface of the crystal exposed to the plasma. Red light is not absorbed by ZnO and hence can travel through the whole thickness (500 μm) of the crystal. It is then expected that the majority of the Raman signal will come from the untreated part of the sample and the layer that contains hydrogen dopants is too thin to contribute enough Raman signal. It is also possible that the detector sensitivity at high Raman shifts is too low to detect anything in that region.

4.6 Synchrotron Light Measurements

Synchrotron light measurement techniques such as X-ray photoelectron spectroscopy (XPS) and X-Ray Absorption Near Edge Spectroscopy (XANES) were used to investigate the chemical states of zinc and oxygen ions before and after hydrogen doping. XPS was used to study the electronic structure of the ZnO crystals, namely the charge states and the band structure and electron distribution. XANES was used to study the local structure around Zn and O atoms in the crystals and how it is affected by hydrogen incorporation.

4.6.1 X-Ray Photoelectron Spectroscopy

X-ray photoelectron spectroscopy (XPS) was used to analyse the chemical states and valence band of both as-received and H-doped ZnO crystals. Figure 4.19 shows the XPS spectrum of the as-received ZnO taken with photon energy of 1487 eV and the X-ray beam incident at an angle of 55° to the normal of the surface of the crystal. The characteristic background originates from electrons that are emitted from ionised atoms deeper under the surface and undergo inelastic scattering processes before they leave the surface of the crystal. The 0 eV level equals the Fermi level of the sample. Several peaks can be observed and it

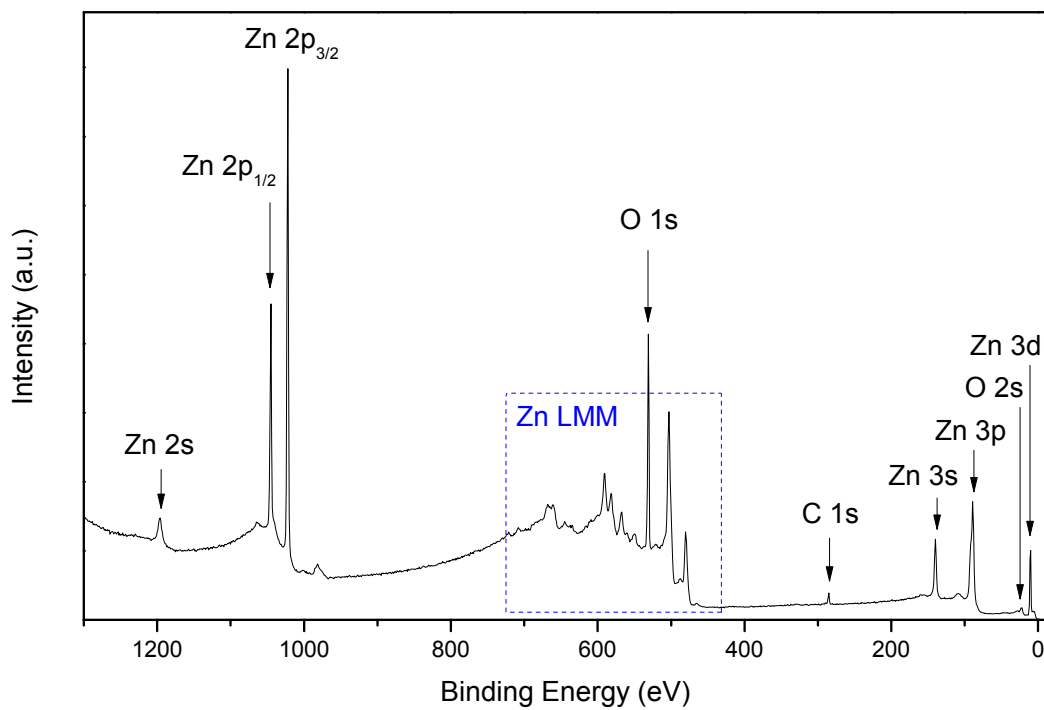


Figure 4.19: XPS spectrum of the as-received *a*-plane ZnO crystal used in this work with core shell zinc and oxygen photoelectron peaks labeled. The region marked LMM are the Auger electrons of zinc. The X-ray photon energy was set at 1487 eV.

is important to distinguish which ones are fundamental to the technique, result from instrumental effects or depend on the chemical nature of the sample and can provide information on the constituents.

Zinc displays a series of lines in the XPS spectrum with each line originating from a particular core level. The line at 1195 eV comes from the 2s core shell of zinc. Two lines at 1045 eV and 1022 eV exhibit the characteristic spin-orbit splitting of the 2p level with the typical intensity ratio of 1:2 and belong to the Zn 2p_{1/2} and Zn 2p_{3/2} respectively. Further peaks associated with zinc are the 3s level at 140 eV, the 3p_{3/2} at 89 eV and the 3d peak at a binding energy of 10 eV. Furthermore, several Auger lines associated with zinc can be identified. These lines occur when an inner core vacancy, that was created by the emission

of a photoelectron due to X-ray bombardment, is occupied by a higher orbital electron, and the transition energy is not emitted as a photon but rather non-radiatively used to ionise another electron. This electron is called an Auger electron and is independent of the initial ionisation source. The Auger lines in the spectra form rather complex patterns, for example the $L_3M_{23}M_{45}(^1P)$ Auger line describes a process with an initial vacancy in a $L_3 = 2p_{3/2}$ state and two final vacancies in the $M_{23} = 3d_{3/2}$ and $M_{45} = 3d_{5/2}$ states. Most of the lines between 400 eV and 700 eV can be assigned to Zn Auger processes.

Other than the zinc peaks, oxygen (1s at 531 eV and 2s at 23 eV) and carbon (1s at 285 eV) can also be clearly identified by their photoelectron and Auger lines. A summary of all detected peaks and their assignments is given in Table 4.3.

Table 4.3: Assignment of the observed transition lines in the XPS spectrum of the as-received *a*-plane ZnO crystal to their chemical identity and electronic configuration.

| Binding energy (eV) | Chemical identity | Configuration |
|---------------------|-------------------|------------------------------------------------------------------|
| 1195 | Zn | 2s |
| 1045 | Zn | 2p _{1/2} |
| 1022 | Zn | 2p _{3/2} |
| 983 | O | KL ₂₃ L ₂₃ |
| 668 | Zn | L ₃ M ₂₃ M ₄₅ |
| 660 | Zn | L ₂ M ₂₃ M ₂₃ |
| 590 | Zn | L ₃ M ₂₃ M ₄₅ (¹ P) |
| 581 | Zn | L ₃ M ₂₃ M ₄₅ (³ P) |
| 567 | Zn | L ₂ M ₂₃ M ₄₅ (¹ P) |
| 531 | O | 1s |
| 503 | Zn | L ₃ M ₄₅ M ₄₅ |
| 479 | Zn | L ₂ M ₄₅ M ₄₅ |
| 285 | C | 1s |
| 140 | Zn | 3s |
| 89 | Zn | 3p _{3/2} |
| 23 | O | 2s |
| 10 | Zn | 3d |

The ratio of zinc to oxygen in the sample was studied using the area under the Zn 3p_{3/2} and O 1s peaks. The atomic fraction of zinc or oxygen can be found

using the following equation [151]:

$$[Zn] = \frac{I_{Zn}/S_{Zn}}{I_{Zn}/S_{Zn} + I_{O}/S_{O}} \quad \text{or} \quad [O] = \frac{I_{O}/S_{O}}{I_{Zn}/S_{Zn} + I_{O}/S_{O}} \quad (4.3)$$

where I is the area under the relevant peak and S is the atomic sensitivity factor (ASF). ASF values are empirically measured for each photoemission peak and are designed to scale the measured areas so that meaningful atomic concentrations can be obtained, regardless of the peak chosen. The ASF at a photon energy of 1486.7 eV for zinc 2p_{3/2} and oxygen 1s are 5.26 and 0.726 respectively [151]. The ratio of zinc to oxygen in the as-received crystal was found to be 0.47:0.53. This ratio is within the range of the uncertainty of the XPS quantisation method and can be considered to be in a 1:1 ratio. It is worth noting that the as-received and the H-doped crystals all show a 1:1 zinc to oxygen ratio.

Of particular interest in terms of hydrogen doping, the oxygen 1s state was further investigated because it is very sensitive to chemical environment and these are reflected in peak shifts or shape changes of the peak. High resolution spectra (100 meV) of the O 1s were recorded at different X-ray photon energies. The X-ray penetration length in ZnO can be found using the following relation [152]:

$$\delta_p = \frac{1}{\alpha} \quad (4.4)$$

where δ_p is the penetration depth and α is the energy dependent attenuation depth.

With higher X-ray photon energy, the kinetic energy of the photoelectrons are higher according to the relation:

$$E_k = h\omega - E_b - \phi \quad (4.5)$$

where $h\omega$ is the energy of the X-ray photon, E_b is the binding energy of the

electron and ϕ is the work function. Higher kinetic energy also means that the probing depth will be higher according to Figure 4.20 which shows the inelastic mean free path (IMFP) of electrons. The IMFP of an electron is the distance an electron can travel without undergoing inelastic collisions. The curve shows that the mean free path is not strongly dependent on the material, but that it is strongly dependent on the electron energy, with the shortest IMFP of $\sim 5 \text{ \AA}$ at 50 eV electron energy.

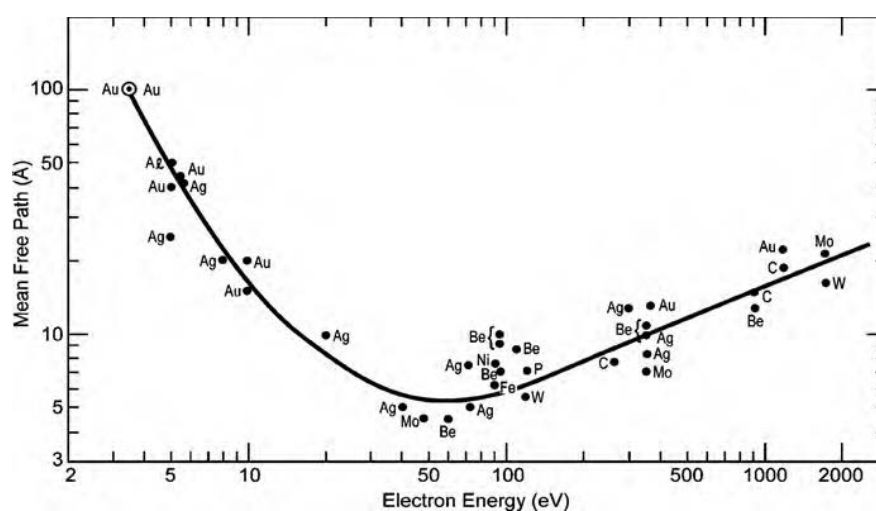


Figure 4.20: Universal curve of the inelastic mean free path of electrons in solids as a function of their energy. From [153].

High resolution XPS spectra of the O 1s core shell were taken at X-ray photon energies of 650, 750, 850, 1000, 1200 and 1487 eV and are presented in Figure 4.21. This corresponds to a probing depth range of $\sim 20 \text{ \AA}$ at a photon energy 650 eV to $\sim 60 \text{ \AA}$ at 1487 eV.

It can clearly be seen that the O 1s peak consists of two components. These two components correspond to oxygen in two different chemical states: the lower energy component at $\sim 530.5 \text{ eV}$ originates from O^{2-} ions fully coordinated by zinc ions in the lattice and the higher energy component at $\sim 532.0 \text{ eV}$ being from hydrogenated O^{2-} ions [23, 154–156].

It was found that the high energy component at 532.0 eV is enhanced after hydrogen incorporation at both temperatures when compared to the as-received crystal

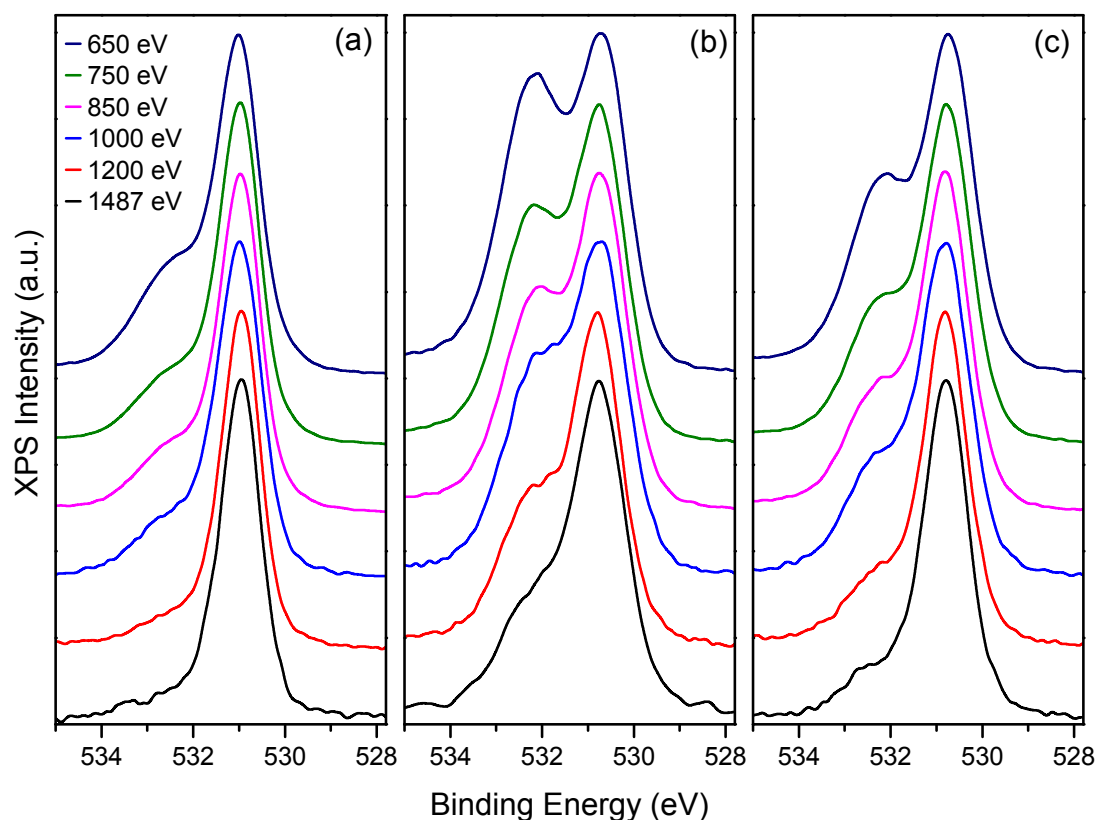


Figure 4.21: High resolution normalised XPS spectra of the O 1s core level of (a) as-received, (b) H-doped at 25 °C and (c) H-doped at 200 °C crystals taken at X-ray photon energies ranging from 650 eV to 1487 eV.

at the same X-ray energies. The crystal doped at 25 °C shows more enhancement of the 532.0 eV component when compared to the one doped at 200 °C. The presence of the higher energy component in the as-received crystal can come from the unintentional hydrogen doping during hydrothermal growth of the crystal or from adsorbed surface -OH groups. An enhancement of the higher energy side is not unexpected because the incorporated hydrogen can lead to the formation of hydrogenated O^{2-} ions. Calculations predict the $\text{V}_{\text{Zn}}\text{-H}_2$ complex to comprise of two non-equivalent O–H bonds with the hydrogen atoms sitting at the V_{Zn} site. One of the O–H bond is aligned 10° off the c -axis of the crystal while the second O–H bond is at an angle of 100° to the c -axis [99, 157]. The increase of the 532.0 eV component is in agreement with CL measurements (see Section 4.4)

which showed a quenching of the green luminescence after hydrogen incorporation. The proposed cause for the quenching behaviour was the formation of neutral $V_{\text{Zn}}\text{-H}_2$ complexes. The 532.0 eV component is also more pronounced when XPS was collected with an X-ray energy beam of 650 eV than at higher photon energies. This is consistent with hydrogen diffusion in ZnO being non-uniform and the diffusion being temperature dependent and is in good agreement with depth-resolved CL measurements (see Section 4.4.5). The crystal treated at 25 °C shows higher enhancement of the 232.0 eV compared to that at 200 °C. This indicates a higher concentration of hydrogen in the near surface region in the sample doped at the lower temperature. The hydrogen is able to diffuse deeper at higher temperatures, thereby reducing its concentration in the near surface region, as evidenced by the lower intensity of the 532.0 eV component at higher treatment temperatures.

The valence band (VB) photoelectron spectra were also collected for all three crystals and are shown in Figure 4.22. The spectra were collected before and after a 20 min argon ion sputtering surface cleaning procedure. The collected VB spectra were normalised to the Zn 3d peak at 10.2 eV. There are two main features in the valence band of the crystals: one peak, B, centered at 7.1 eV and a peak, A, centered at 4.3 eV. Peak B has been assigned to the mixed O 2p and Zn 4s states while peak A has been assigned to O 2p states [158, 159].

The onset of the valence band for the as-received crystal is shifted from 3.0 eV to 2.7 eV below the Fermi level after Ar ion sputtering. This is consistent with adsorbed surface defects, e.g. $-\text{OH}$ groups, increasing the n -type conductivity of the crystal. The intensity of both the A and B peaks of the doped samples is increased following hydrogen plasma. The valence band onset is also reduced to ~ 1.2 eV when compared to the as-received crystal. After Ar ion sputtering, the valence band of all three crystals display similar intensities and shapes. This indicates that surface states were created by the hydrogen plasma for the doped samples and were removed after Ar ion sputtering. The change in the valence

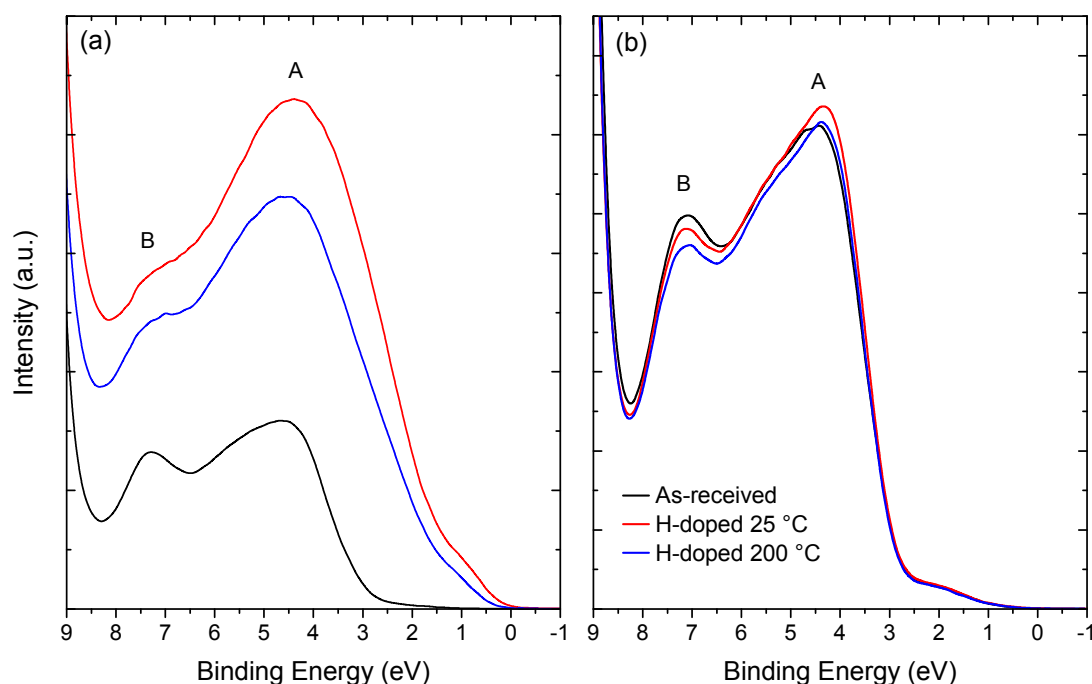


Figure 4.22: Valence-band photoemission spectra of the as-received, H-doped at 25 °C and H-doped at 200 °C ZnO crystals. Spectra were taken (a) before and (b) after 20 minutes of argon ion sputtering. The 0 eV energy is the Fermi level position. Spectra were collected at a photon energy of 160 eV and normalised to the Zn 3d peak.

band of the as-received crystal can be attributed to the removal of residual adsorbed surface states.

4.6.2 X-Ray Absorption Near Edge Spectroscopy

X-Ray Absorption Near Edge Spectroscopy (XANES) was performed to study the conduction band of the ZnO crystals before and after hydrogen incorporation. XANES was collected in two modes, total fluorescent yield (TFY) and total electron yield (TEY). While both techniques investigate the absorption cross section, the sampling range is different. TEY mainly studies the surface of crystals (~ 10 nm or so) while TFY gives more information on the bulk of the crystal. This is because X-ray photons can travel μm range in ZnO as shown in Figure 4.23. The attenuation depth is the distance, λ , into the material measured

along the surface normal where the intensity of X-rays falls to $1/e$ of its value at the surface [152]. So in ZnO, X-rays have a travel range of about $1\ \mu\text{m}$ even at the absorption edges, making TFY a bulk measurement technique. On the other hand, electron interaction with matter is higher than that of photons, allowing only photoelectrons which are generated directly below the surface ($\sim 10\ \text{nm}$) to be emitted from the surface. TEY is therefore a surface measurement technique. By recording both the TEY and TFY concurrently during the X-ray absorption measurements, information about both the surface and bulk of the ZnO crystals can be studied.

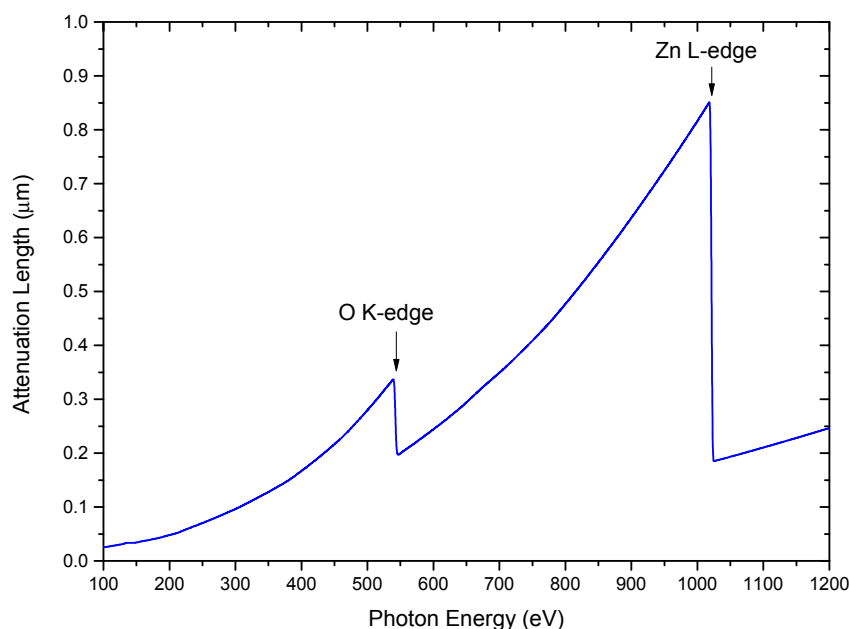


Figure 4.23: X-ray attenuation length in ZnO. The attenuation decreases drastically at the O and Zn absorption edges, but X-rays can still travel μm distances before being absorbed by the crystal. Adapted from [160] and [161].

The ZnO samples were loaded in the analysis chamber for XANES measurements in such a way to allow the as-received and H-doped ZnO crystals to be rotated as shown in Figure 4.24. The beam was incident at a normal angle to the a -plane surface of the crystals, with the polarisation of the beam being in the horizontal.

The crystals were oriented so that the electric field was perpendicular to the c -axis when $\theta = 90^\circ$, parallel to the c -axis when $\theta = 0^\circ$ or at an angle of 45° to the c -axis.

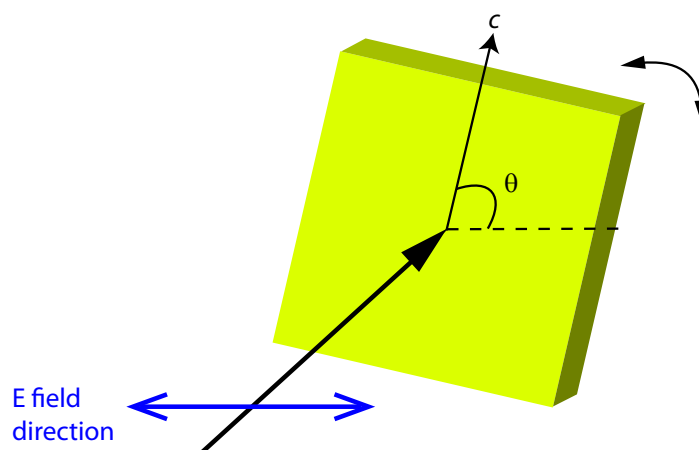


Figure 4.24: XANES experimental geometry. The X-ray beam was normally incident to the a -plane surface of the crystals. The beam was linearly polarised with the polarisation direction in the horizontal. The angle θ was used to align the electric field vector of the X-ray beam parallel, perpendicular or at 45° to the c -axis of the crystal.

Figure 4.25 shows the XANES spectra recorded in both TEY and TFY modes of the O K-edge for the as-received and the crystals doped at 25°C and 200°C . The angle the c -axis of the crystals made with the electric field vector of the X-ray beam was also set at 0° , 45° and 90° . Both the TEY and TFY exhibit a series of sharp features labeled A to K for all three samples. The relative intensity of the peaks are dependent on the angle θ between the c -axis and the polarisation of the incoming photons. While the assignment of the features in the absorption spectra is still controversial, there has been some agreement on some of the assignments. Peak A has been attributed to an electron excitation from the O 1s state to O $2p_{x+y}$ states hybridised with Zn 4s states; features in the region from 539 eV to 550 eV (peaks B to G) can be attributed to O $2p_z$ orbitals hybridised with Zn 4p states and the region above 550 eV (peaks I to K) to O 2p

orbitals hybridised with Zn 4d states [158, 162–164]. A summary of the peaks and assignments associated with the O K-edge is given in Table 4.4.

Moreover, the H-doped crystals also exhibit a pre-edge feature at 528 eV labeled PE in the TEY mode which is not present in the TFY measurements. The pre-absorption edge feature, PE, in the TEY spectra of the H-doped crystals has been associated to the $1s \longrightarrow \sigma_{\text{OH}}$ resonance of the O–H bond [165–167]. This result is consistent with hydrogen forming O–H bonds in the crystals. The presence of the PE feature only in the TEY spectra indicates that this transition mainly occurs in the near surface region of the H-doped crystals and can be attributed to a high concentration of hydrogen in that region. This is consistent with XPS measurement in which the component of the O 1s photoelectron peak associated to hydrogenated O^{2+} ions is enhanced in the surface region. It is also possible that hydrogen creates new states just below the conduction edge and these states are reflected by the pre-absorption edge.

The difference in intensity of the various features in the H-doped crystals when compared to the as-received one can be explained by hydrogen filling the lowest empty levels in the conduction bands with electrons. In ZnO, the first unoccupied molecular orbital is the $3a_{1g}$ orbital which can be attributed to the broad feature A in the O K-edge spectra at 537 eV [162, 168]. Hydrogen, being a donor in ZnO, donates electrons to the conduction band as evidenced by Hall measurements (see Section 4.3). The first free orbital in the conduction band of ZnO is the $3a_{1g}$ orbital which is a hybridisation of the O $2p_{x+y}$ and Zn 4s orbitals. The electrons from hydrogen fill the $3a_{1g}$ orbital and this is shown as a decrease in the intensity of the peak A after hydrogen incorporation. Features B and C are enhanced because the lower energy $3a_{1g}$ orbital is now filled and electron excitations from the O 1s levels to those free orbitals responsible for features B and C are enhanced. Moreover, the features B and C are broader in the H-doped crystals in comparison to the as-received one. This broadening has been attributed to the presence of oxygen vacancies in the near-surface region

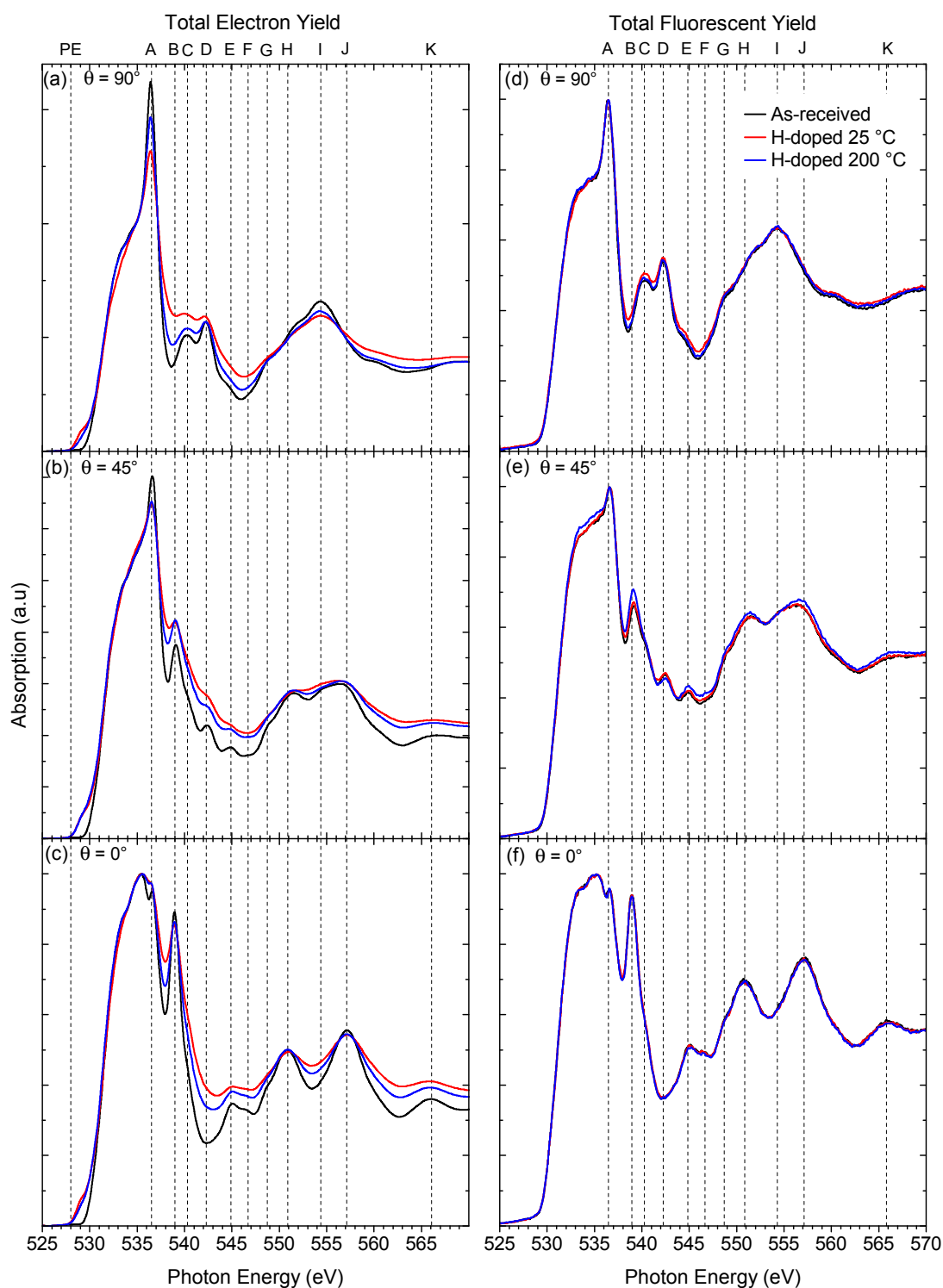


Figure 4.25: O K-edge XANES taken in both TEY and TFY modes for as-received, H-doped at 25 °C, H-doped at 200 °C at angle $\theta = 90^\circ$ in (a) and (d), $\theta = 45^\circ$ in (b) and (e), and $\theta = 0^\circ$ in (c) and (f).

[169, 170]. The origin of the broadening in the H-doped samples can be attributed to removal of oxygen atoms from the surface during hydrogen plasma treatment. This is consistent with the flattening of the surface observed following hydrogen plasma by AFM measurements (see Section 4.2).

The XANES spectra for all three samples show a high orientation dependence with different features present at different angles. The orientation dependence can be explained by the polarisation of the Zn–O bonds. The p_{x+y} orbitals lie in a plane perpendicular to the c -axis while the p_z orbitals lie parallel to the c -axis. Depending on the orientation of the electric field vector of the incoming photons in relation to the c -axis, some transitions can be enhanced [158, 164]. Features A, C, D, and I are enhanced when the electric field vector of the incoming photons is perpendicular to the c -axis ($\theta = 90^\circ$). This indicates that transitions from the O 1s level to O $2p_{x+y}$ like orbitals are enhanced. Features B, E, H, and J are enhanced when the electric field vector is parallel to the c -axis ($\theta = 0^\circ$). In this case, the empty orbitals are of O $2p_z$ type. At an angle $\theta = 45^\circ$, contributions from both O $2p_{x+y}$ and O $2p_z$ type orbitals can be observed. This spectral shape is often reported for the O K-edge XANES spectra of ZnO nanoparticles which have random orientations [164].

Figure 4.25 shows the XANES spectra recorded in both TEY and TFY modes of the Zn L_3 -edge for the as-received and the crystals doped at 25 °C and 200 °C. As was the case with the O K-edge XANES spectra, both the TEY and TFY exhibit a series of sharp features labeled L to U for all three samples. According to the dipole-transition selection rule, the Zn L-edge XANES probes the unoccupied Zn s- and d-derived states [171]. The Zn 3d orbital is fully occupied, so the lowest unoccupied orbital of the Zn ion is Zn 4s, followed by Zn 4p and Zn 4d [158, 172]. The features L and M have been attributed to the transitions of a Zn 2p electron to a Zn 4s state [158]. Features N to V have been attributed to transitions from Zn 2p states to Zn 4d states [173–175].

At every angle measured for both TEY and TFY, the spectra from the as-received and the two H-doped crystals look identical. This implies that hydrogen has not interacted with zinc states. Moreover, the angle dependence can be explained in a similar way to the O K-edge. Features L and M have contributions from Zn 4s derived states which are not sensitive to the photon polarisation and as such are not angle dependent. Features associated with Zn 3d states (N to V) show high angle dependencies because the d states are highly directional.

Table 4.4: Summary of XANES peaks for O K-edge and Zn L-edge and their assignments in the ZnO crystals used in this work.

| Peak | Energy range (eV) | Assignment |
|-------|-------------------|------------------------|
| A | 538 | O $2p_{x+y}$ and Zn 4s |
| B – G | 539 – 550 | O $2p_z$ and Zn 4p |
| I – K | > 550 | O 2p and Zn 4d |
| L, M | 1015 – 1025 | Zn 4s |
| N – V | > 1025 | Zn 4d |

The XANES results of the oxygen and zinc absorption edges can help understand where hydrogen sits in the lattice of the crystal. There are three possible positions for interstitial hydrogen to occupy in the lattice that have been reported (see Section 2.6.2) [86, 102]. These are namely the bond-centered (BC) positions where hydrogen sits along the bond between the host zinc and oxygen atoms; the anti-bonding orientation where hydrogen is attached to a host oxygen atom and pointing away from the Zn–O bond (AB_O); the anti-bonding orientation where hydrogen is attached to a host zinc atom and pointing away from the Zn–O bond (AB_{Zn}). The XANES results show that hydrogen interacts with O atoms only and not Zn. This indicates that the majority of the hydrogen dopants introduced by plasma sit at the AB_O site.

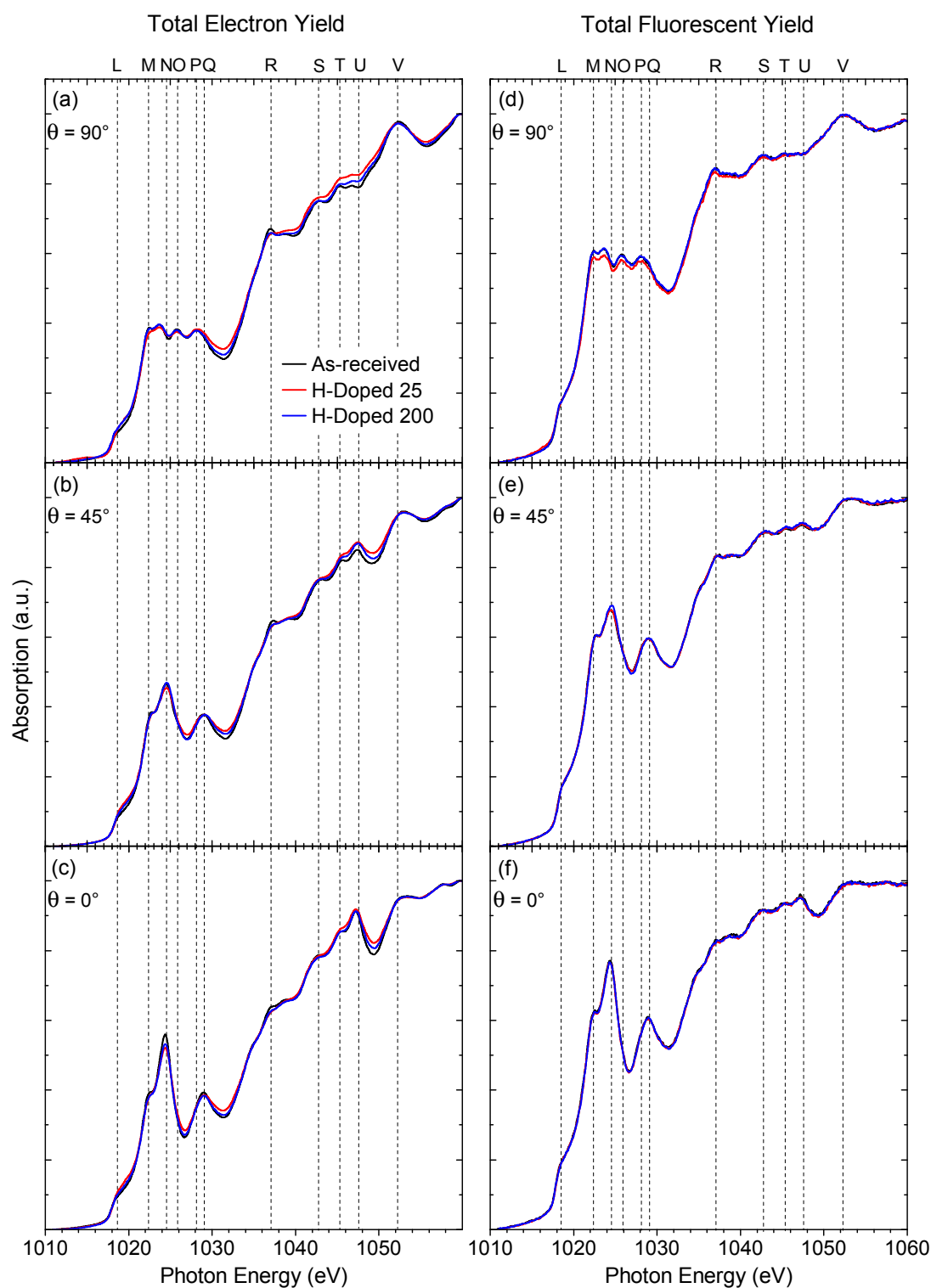


Figure 4.26: Zn L-edge XANES taken in both TEY and TFY modes for as-received, H-doped at 25 °C, H-doped at 200 °C at angle $\theta = 90^\circ$ in (a) and (d), $\theta = 45^\circ$ in (b) and (e), and $\theta = 0^\circ$ in (c) and (f).

From the combined valence band spectra and XANES measurements, the band structure around the top of the valence band and bottom of the conduction band for both as-received and H-doped ZnO crystals are shown in Figure 4.27. The position of the Fermi level was found from the XPS measurements while the separation of the conduction band and valence band was found using the value of the band gap energy obtained from the free exciton energy measured by CL.

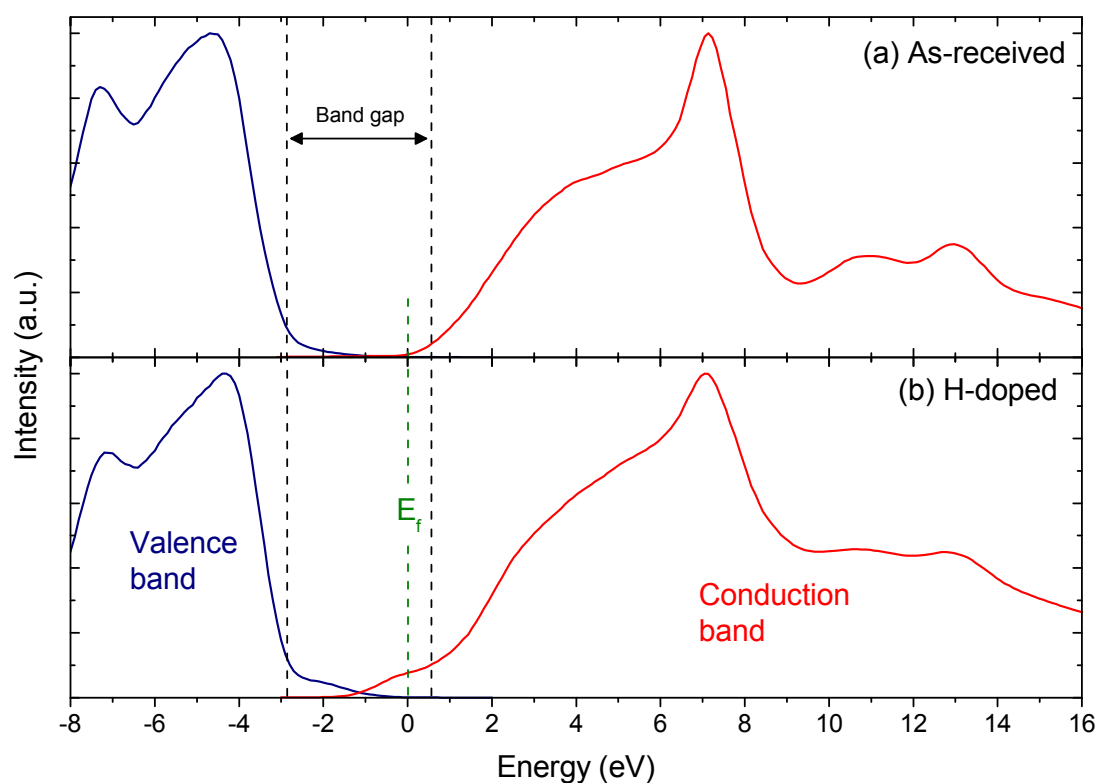


Figure 4.27: Band structure of (a) as-received and (b) H-doped ZnO crystals obtained from XPS and XANES measurements.

4.7 Summary

Hydrogen dopants were introduced in ZnO at low temperatures following RF plasma exposure. Hydrogen can be incorporated in ZnO crystals at temperatures below 435 °C. It was found that at 200 °C, hydrogen diffused to at least a depth of 1.5 μm , while it was more concentrated in the near-surface region for lower plasma temperatures. XRD and Raman results showed that no damage was caused to the bulk of the crystal.

The carrier concentration increases from $2.1 \times 10^{14} \text{ cm}^{-3}$ to $2.8 \times 10^{16} \text{ cm}^{-3}$ after hydrogen plasma. This increase in carrier concentration is attributed to the formation of shallow hydrogen donors. The intensity of the donor bound exciton was also increased following hydrogen plasma while the intensity of the free exciton was unchanged. This further supports the formation of shallow hydrogen donors. PL analysis of the bound exciton spectral region reveals that intensity of both the I_4 and $I_{4a,b}$ increases after hydrogen incorporation, suggesting that hydrogen dopants introduced by the plasma are in a different chemical state to those incorporated during the hydrothermal growth. PL also showed that the intensity of the peak at 3.3363 eV increases after plasma incorporation. This peak is at the position of the Y line and is associated to extended structural defects which have been created at the surface during plasma treatment.

The green luminescence was also quenched after hydrogen plasma while the yellow luminescence was slightly increased. The green luminescence is thought to originate from a transition involving zinc vacancies. The passivation of the green luminescence is attributed to hydrogen forming neutral $V_{\text{Zn}}\text{-H}_2$ complexes. This complex is made up of two hydrogen bonding to oxygen at the zinc vacancy site. XPS results show an increase in hydrogenated oxygen after plasma, consistent with the formation of $V_{\text{Zn}}\text{-H}_2$ complexes, with the enhancement higher near the surface of the crystals. XPS also showed that the efficiency of introducing hydrogen in ZnO is higher at lower sample temperature.

XANES results show that hydrogen interacts only with oxygen atoms in the lattice and not zinc. This indicates that most of the interstitial hydrogen incorporated by plasma treatment sit at the anti-bonding site of the oxygen atom, with the hydrogen attached to a host oxygen atom and pointing away from the ZnO bond.

Chapter 5

Hydrogen States and Recombination Kinetics in ZnO

5.1 Introduction

Optical properties of semiconductors are most often reported at ~ 4 K. In this chapter the temperature dependence of the luminescence of ZnO from 10 K to 300 K and the various mechanisms of thermal quenching are investigated. Negative thermal quenching of the NBE emission in hydrogen doped ZnO will be introduced and a model involving shallow traps presented.

The recombination processes of excited electron-hole pairs by examining the relationship between excitation density and luminescence emitted and temperature dependence of emitted bands is also investigated.

The yellow luminescence in ZnO is often attributed to lithium impurities occupying zinc sites (Li_{Zn}). It will be shown that the yellow luminescence in the ZnO crystals used in this work can be attributed to radiative recombinations involving Li_{Zn} . The interaction of hydrogen with lithium impurities leading to the formation of hydrogen-lithium complexes is also investigated.

Finally the stability and electro-migration of hydrogen dopants under the electron beam in ZnO will be investigated.

5.2 Temperature Dependence of the Luminescence

Figure 5.1 shows the CL spectra of both the doped and H-doped ZnO crystals. The H-doped crystal has been exposed to the hydrogen plasma for 120s while the crystal was being kept at 200 °C. These conditions were used because at that temperature hydrogen is still being incorporated in the lattice and the temperature is enough to anneal out some of the damage caused by the plasma (See Section 4.4 for a more in-depth discussion).

The CL for both as-received and H-doped crystals show similar features namely the neutral donor bound exciton (D^0X) and the first two phonon replicas of the free exciton luminescence: FX-1LO and FX-2LO. The FX emission is virtually unchanged at low temperatures while the D^0X emission increases considerably. The intensity of the H-doped crystal is higher than that of the as-received one for all temperatures. This is consistent with the formation of new shallow donor levels after hydrogen incorporation. With increasing temperature, the emission peaks get broader and red-shift. The intensity of the D^0X emission decreases with increasing temperature and the D^0X peak is not present at temperatures above 120 K. This is consistent with the neutral donors responsible for that luminescence being thermally ionised with increasing temperature. The red shift of the D^0X peak can be attributed to successive ionisation of bound exciton. Bound exciton emissions have localisation energies ranging from 3 meV to 27 meV [27]. Emissions with low localisation energies (e.g. I_4) will be thermally ionised first while emissions with higher localisation energies (e.g. I_9) are still present

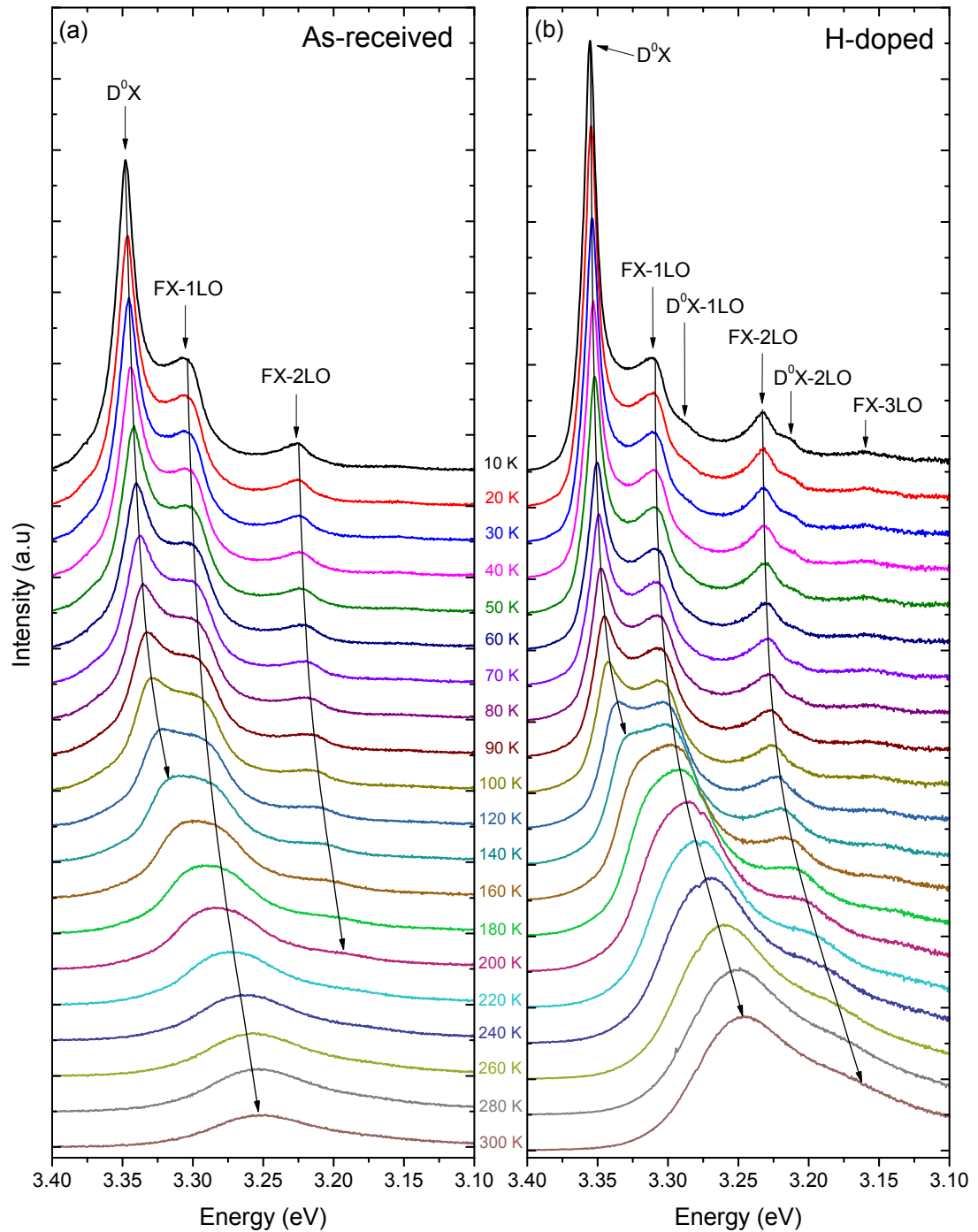


Figure 5.1: Temperature dependent CL spectra of the NBE region of (a) as-received and (b) H-doped ZnO taken from 10 K to 300 K. The arrows show the shifts in the CL peaks with increasing temperature. The plots are vertically shifted for clarity. All spectra were collected with a beam energy of 15 keV and beam current of 5.7 nA.

unionised at higher temperatures. This then leads to a red-shift of the whole D⁰X peak.

It was also found that the dominant luminescence peak in the CL spectra is the FX-1LO at temperatures above ~ 200 K. As the average kinetic energy of free excitons increases with rising temperature, the thermal redistribution leads to a smaller number of free excitons near the centre of the Brillouin zone, thus enhancing the participation of LO phonons in the radiative recombination. The strong LO-phonon-exciton coupling is consistent with the reported PL data of ZnO at elevated temperatures [176, 177].

The energy separation between the FX and phonon replica (FX-1LO and FX-2LO) emission peaks exhibit strong temperature dependence. Considering the spectral line shape of the phonon replicas, the spectral line shape F for the first LO phonon replica of the free exciton has the form [177–179]:

$$F(\varepsilon) \sim \varepsilon^{\frac{1}{2}} \exp\left(\frac{-\varepsilon}{k_B T}\right) W(\varepsilon) \quad (5.1)$$

where ε is defined as $h\nu - E_{\text{FX}} - h\omega_{\text{LO}}$ and $W(\varepsilon)$ is the transition probability for the phonon-assisted emission. The form assumed for the probability $W(\varepsilon)$ then determines the energy separation between the FX and the phonon replica. Let $W(\varepsilon)$ vary as ε^p , where p is a constant. The peak energy of the phonon replica are then shifted by $(p+1/2)k_B T$ to higher energy. At low temperatures, the probability rate $W(\varepsilon)$ for the FX-1LO is assumed to be proportional to ε , implying $p = 1$ [178]. The peak of the FX-1LO will then be shifted by $(1 + 1/2)k_B T = 3/2 k_B T$ to higher energies. The energy position of the peak of the FX-1LO can then be written as:

$$E_{\text{FX-1LO}} = E_g(T) - E_{\text{ex}} - h\omega_{\text{LO}} + \frac{3}{2} k_B T \quad (5.2)$$

where $E_g(T)$ is the bandgap at temperature T , E_{ex} is the temperature independent exciton binding energy with a value of 60 meV [180] and $h\omega_{\text{LO}}$ is the LO phonon energy of 72 meV.

For the FX-2LO, the transition probability is a constant, implying that $W(\varepsilon)$ varies as ε^0 . Thus $p = 0$ and the peak energy of the FX-2LO emission is shifted by $(0 + 1/2)k_B T = 1/2 k_B T$ to higher energies. The energy position of the peak of the FX-2LO can then be written as:

$$E_{\text{FX-2LO}} = E_g(T) - E_{\text{ex}} - 2h\omega_{\text{LO}} + \frac{1}{2}k_B T \quad (5.3)$$

The energy shifts of the FX-1LO and FX-2LO at a temperature T are illustrated in Figure 5.2.

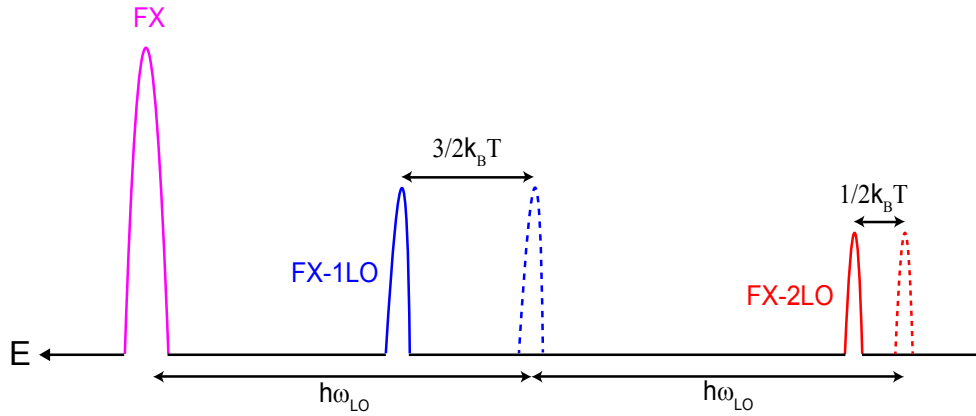


Figure 5.2: Temperature dependence of the peak energy position of the phonon replica. The dashed lines are the predicted energy and the full lines are the actual measured energies.

The position of the free exciton peaks for both the as-received and H-doped crystals were determined from the positions of the FX-1LO and FX-2LO using Equations 5.2 and 5.3. The energy position of the FX is given by the following relation:

$$E_{\text{FX}} = E_g - E_{\text{ex}} \quad (5.4)$$

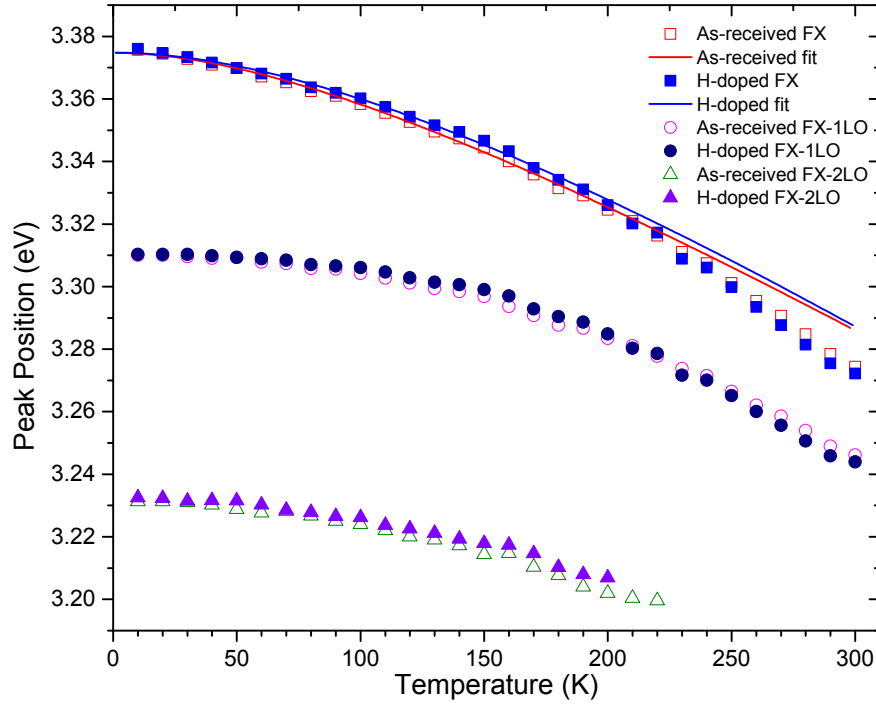


Figure 5.3: Temperature dependence of the FX, FX-1LO and FX-2LO of the as-received and H-doped ZnO crystals. The lines are Varshni fits to the experimental data based on Equation 5.5.

The Varshni relation was then used to fit the temperature dependence of the peak position of the FX and has the form [29]:

$$E_g(T) = E_g(0) - \frac{\alpha T^2}{T + \beta} \quad (5.5)$$

where $E_g(T)$ is the energy gap at temperature T , $E_g(0)$ is the energy gap at 0 K, α and β are empirically measured constants. Typical values of α and β for ZnO are 5×10^{-4} eV/K and 900 K respectively [30].

The calculated energy position of the FX was found to be 3.375 eV for the as-received ZnO and 3.376 eV for the H-doped one. These energy positions of the FX emission match those of 3.375 eV to 3.378 eV reported in the literature very well [27, 58, 181]. The temperature variation of the FX peak energy also follows the Varshni relation. The Varshni parameters α and β obtained from the fits are reported in Table 5.1. The parameters for both the as-received and H-doped

Table 5.1: Varshni fit parameters for the NBE luminescence peaks

| Peak | α (eV/K) | β (K) |
|----------------------------|-----------------------|-------------|
| Free exciton from Ref [30] | 5.05×10^{-4} | 900 |
| As-received FX | 7.19×10^{-4} | 776 |
| Doped FX | 6.75×10^{-4} | 790 |

ZnO are similar with α being 7.19×10^{-4} eV/K and 6.75×10^{-4} eV/K for the as-received and H-doped ZnO respectively; and values of β being 776 K and 790 K for the as-received and H-doped ZnO respectively as is expected from the similar positions of the FX and the phonon replica. A slight deviation from the fit is observed above 200 K due to the uncertainty in determining the peak position resulting from temperature broadening and overlap of the LO phonon replicas.

The measured energy positions of the D⁰X and FX emissions are presented in Figure 5.4. The energy separation between the D⁰X and the FX is constant. This is expected as the bound excitons follow the following energy relation:

$$E_{\text{DX}} = E_g - E_{ex} - E_{\text{loc}} \quad (5.6)$$

where E_{loc} is the localisation energy of the bound exciton. The localisation energy is the energy separation between the D⁰X emission and the free exciton emission. The average localisation energy of the bound exciton is calculated to be 23 meV for the as-received crystals and 19 meV for the H-doped one. The shift is consistent with the PL measurements which found a blue-shift of the main bound exciton peak following hydrogen doping (see Figure 4.6). The increase in the energy separation at higher temperatures can be explained by thermal ionisation of bound excitons of localisation energy lower than the thermal energy e.g. I_4 to form free excitons. The bound excitons with higher localisation energies e.g. I_9 will still be bound and this explains the increase in the energy separation between the FX and BX peak with increasing temperature.

The intensities of the various NBE peaks as well as for the DLE were extracted

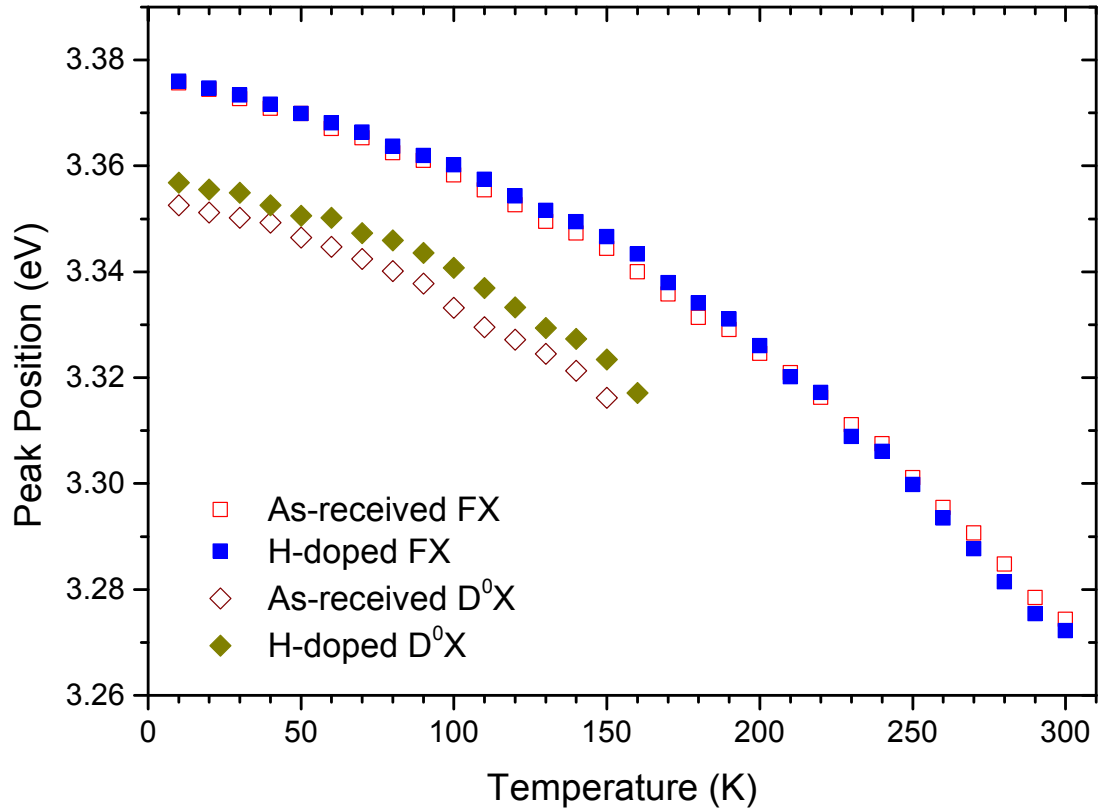


Figure 5.4: Temperature dependence FX and D⁰X for both the as-received and H-doped crystals.

from the temperature dependent CL spectra. Figure 5.5 shows the intensity of the D⁰X, FX-1LO and FX-2LO emission peaks as a function of temperature for both the as-received and H-doped ZnO crystals. The intensity of the FX could not be extracted accurately due to its small intensity. The broadening of the peaks with increasing temperature makes finding the peak position for the FX-2LO, and hence its intensity, accurately difficult after 200 K. For the as-received crystal, the intensities of all three peaks decrease with increasing temperature, with the D⁰X peak being annealed out at 150 K and merging with the FX-1LO peak, which is the main peak at room temperature as can be seen in Figure 5.1. The H-doped crystal shows a different temperature dependence to the as-received one. The intensity of the D⁰X peak decreases from 10 K to 120 K. The intensity however increases for temperatures higher than 120 K until the emission disappears because of the thermal ionisation of the donors. A similar behaviour

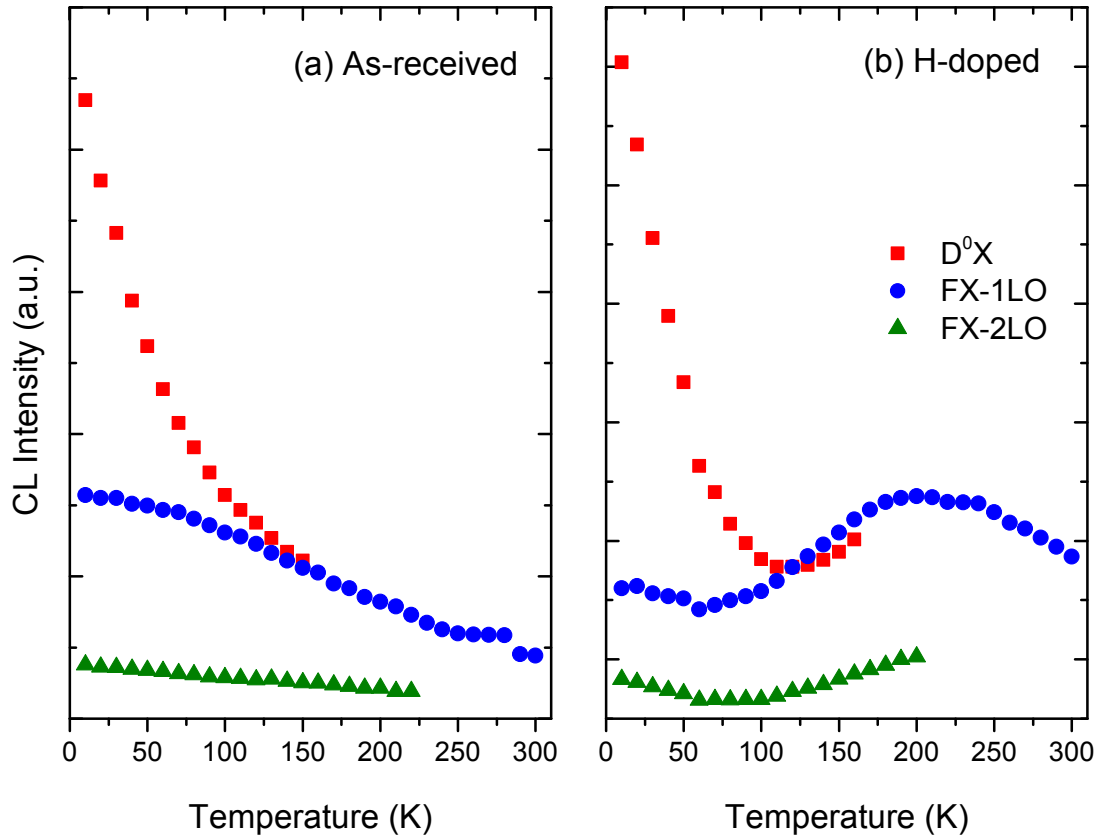


Figure 5.5: Temperature dependence of the D⁰X, FX-1LO and FX-2LO peak intensities for (a) the as-received and (b) H-doped crystals. The H-doped sample exhibits a negative thermal quenching behaviour.

is seen for both the FX-1LO and FX-2LO. The intensity of those luminescence peaks decrease with increasing temperature in the range $10 \text{ K} \leq T \leq 90 \text{ K}$, the intensity then increases in the range $90 \text{ K} < T \leq 220 \text{ K}$ and the intensity decreases for temperatures above 220 K. This behaviour is a unusual and often called a negative thermal quenching (NTQ) behaviour. This NTQ effect will be discussed further in the following section (Section 5.3).

A similar investigation of the temperature dependence of the DLE was made. Figure 5.6 shows the integrated intensities of the yellow and green luminescences for both the as-received and H-doped crystals. Both the yellow and green luminescence follow the normal thermal quenching behaviour for both the as-received and H-doped crystals. This behaviour is similar to the NBE luminescence of the

as-received crystal.

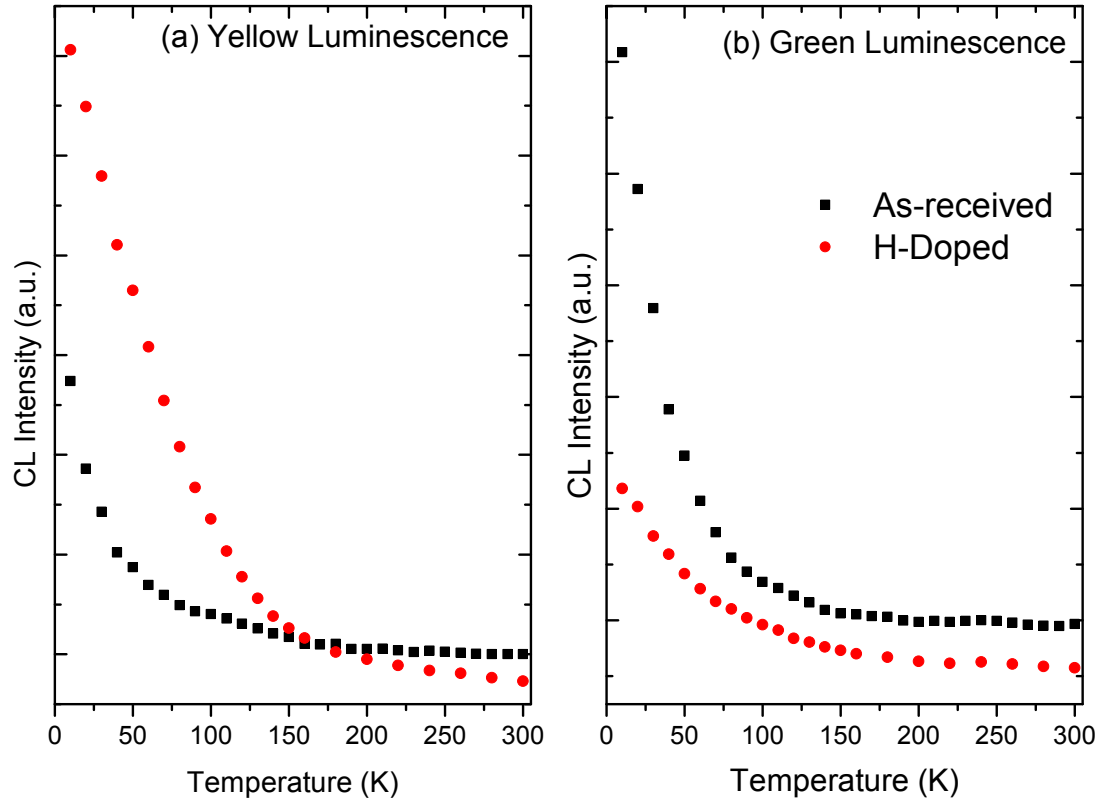


Figure 5.6: Temperature dependence of the CL intensity of the (a) yellow and (b) green luminescence for the as-received and H-doped crystal. The H-doped crystal does not exhibit a NTQ behaviour in the DLE.

5.3 Negative Thermal Quenching of the NBE Luminescence

The intensity of the luminescence (e.g. from PL and CL) in solids, such as semiconductors and ionic crystals, is normally expected to decrease with increasing temperature. This phenomenon is known as “thermal quenching” of the luminescence. The basic mechanism behind the thermal quenching phenomenon is that non-radiative recombination probability of electrons and holes increase with increasing temperature [182, 183].

It has been reported that for GaAs, in a moderately high temperature range, the intensity of the luminescence increases with increasing temperature [184]. This abnormal phenomenon is called “negative thermal quenching” (NTQ). The physical origin of NTQ is thought to be due to the thermal activation of electrons from the levels with energy smaller than that of the initial state of the radiative transition or by the release of carriers or excitons from trap states with increasing temperature. Shibata (1998) has proposed an analytical formula to describe the temperature dependence of the luminescence intensity of a system which exhibits the NTQ phenomenon [185]:

$$I(T) = I(0) \left[\frac{1 + \sum_{q=1}^w D_q \exp(-E'_q/k_b T)}{1 + \sum_{j=1}^m C_j \exp(-E_j/k_b T)} \right] \quad (5.7)$$

where $I(T)$ is the intensity of the luminescence at temperature T , w is total number of intermediate states responsible for the NTQ behaviour, each having the activation energy E'_q , m is the total number of non-radiative recombination processes, each having the activation energy E_j and C and D are constants which describe the relative contributions of the different activation processes. This formula enables quantitative analysis of the mechanisms of the NTQ and allows determining the activation energies associated with intermediate states as well as non-radiative states.

Recently this negative thermal quenching behaviour has been observed in both as-grown and doped ZnO crystals and nanostructures. Watanabe et al. (2006) reported on this NTQ behaviour in hydrothermal grown ZnO crystals from CrysTec, EaglePicher, and TOKYO DENPA, and in as-received epitaxial ZnO single crystals grown by radical-source molecular beam epitaxy [186]. While no mechanism was proposed, a series of activation energies for the different processes was calculated by using Equation 5.7. Wu et al. (2012) reported on the NTQ of the 3.338 eV emission in ZnO nanorods [187]. They proposed a transition from the

3.338 eV emission to the surface exciton recombination at 3.368 eV via trap states which are activated with temperature. While not a NTQ of the luminescence, Singh et al. (2013) reported a similar increase in the conductivity of hydrogen doped ZnO thin films with increasing temperature [188]. They have attributed this behaviour to metal-semiconductor transitions. Above the transition temperature, the ZnO film acts as a degenerate semiconductor because of the high hydrogen doping levels. With increasing hydrogen doping, the defect band eventually overlaps with the conduction band creating a degenerate semiconductor. This leads to delocalisation of electrons and consequently metallic conductivity and an increase of the measured conductivity.

The activation energy of the non-radiative traps for the as-received crystal was calculated by applying a non-linear least square fit to the integrated NBE luminescence data using Equation 5.7 in the following form:

$$I(T) = \frac{I(0)}{1 + C \exp(-E/k_bT)} \quad (5.8)$$

This equation represents the formula commonly used to analyse the thermal quenching phenomenon in systems which do not exhibit NTQ behaviours. Fitting this equation to the integrated NBE region of the as-received ZnO crystal, an activation energy, E , of 11.6 meV was extracted and the fit shown in Figure 5.7. This activation energy matches well with reported binding energies of excitons to defects or traps which are in the range of 10 meV to 20 meV [135, 189].

To analyse the temperature dependence for the NBE luminescence of the H-doped sample, Equation 5.7 was rearranged in the following forms for different temperature ranges:

$$I(T) = I(0) \left[\frac{1 + D \exp(-E'/k_bT)}{1 + C_1 \exp(-E_1/k_bT)} \right] \quad \text{or} \quad I(T) = \frac{I(0)}{1 + C_2 \exp(-E_2/k_bT)}$$

for $10 \text{ K} \leq T \leq 320 \text{ K}$ for $T > 320 \text{ K}$

(5.9)

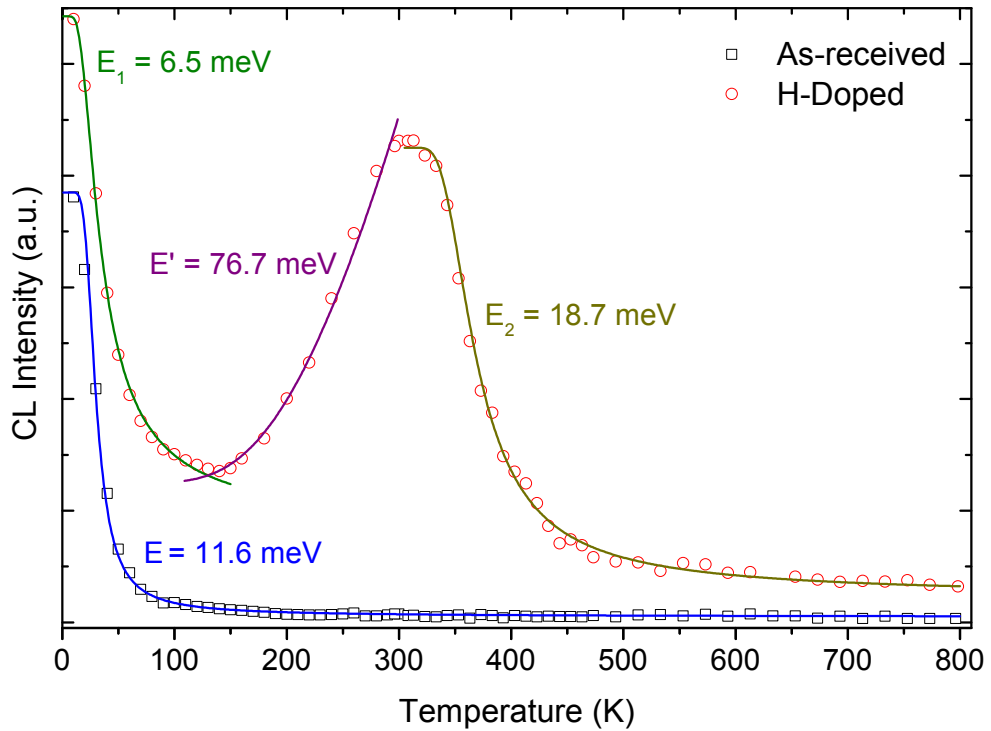


Figure 5.7: CL intensity of the integrated NBE luminescence from 10 K to 800 K for the as-received and H-doped crystals. The H-doped crystals exhibits a clear NTQ behaviour in the range 140 K to 320 K. The lines show the fits of the luminescence based on Equation 5.7.

In this case, the NTQ behaviour is taken into account in the formula. The numerator part of the formula contains the activation energy of the intermediate states E' while the denominator contains the activation energy E of the non-radiative traps. Two energies E_1 and E_2 were used to determine the activation energies of the non-radiative processes for $10 \text{ K} < T \leq 140 \text{ K}$ and $T > 320 \text{ K}$. The fits in Figure 5.7 resulted in values of activation energies of $E_1 = 6.54 \text{ meV}$ for the temperature range $10 \text{ K} < T \leq 140 \text{ K}$, $E_2 = 18.7 \text{ meV}$ for temperature $T > 320 \text{ K}$, and $E' = 76.7 \text{ meV}$ for the range $140 \text{ K} < T \leq 320 \text{ K}$ for the H-doped crystal. While the values of E_1 and E_2 are still in the range of activation energies of excitons binding to defects or traps, the different energies however indicate a different thermal quenching mechanism or trap. The high activation energy of 76.7 meV indicates that the NTQ mechanism is not solely a thermal process and must involve other intermediate states.

The negative thermal quenching behaviour of the NBE following hydrogen incorporation might be attributed to the following mechanisms:

1. introduction of additional recombination channels via neutral donor bound exciton emission at H-related shallow donor states, known as the I_4 line.
2. elimination of the competitive radiative recombination channel by the formation of H complexes with the green luminescence centre.
3. release of electrons from H-related traps which then bind with holes to form excitons.
4. release of electrons from shallow traps which are then captured by deep traps, eliminating this pathway.

Introduction of additional recombination channels, e.g. enhancement of the I_4 line, and elimination of competitive radiative channels are unlikely causes for the NTQ behaviour. No new peaks were found in high resolution low temperature PL measurements (see Section 4.4.1). Moreover, passivation of competitive radiative channels is also unlikely because shallow donors in ZnO would likely have already been thermally ionised at 150 K and not be able to take part in radiative recombinations. This is because of their localisation energies in the range of 10 meV to 15 meV which is lower than the thermal energy at 150 K. This leaves the possibility of H-related traps or other shallow traps releasing carriers with increase in temperature as a possible explanation for the NTQ behaviour.

5.4 Shallow Carrier Traps in ZnO

Q-DLTS was performed on the as-received and H-doped crystals to investigate the creation and activation energies of shallow carrier traps. Gold was used to make Schottky contact on one side of the crystal and indium was used to make Ohmic contact on the other. Figure 5.8 shows the characteristic $I - V$ curve of the Au Schottky contact on the H-doped a -plane ZnO crystal. The forward bias was obtained by applying a positive bias to the Au contact. A rectifying behaviour is achieved even though there is a relatively large reverse current. This reverse current is characteristic of Au Schottky contacts on ZnO and has been attributed to tunneling conduction [190].

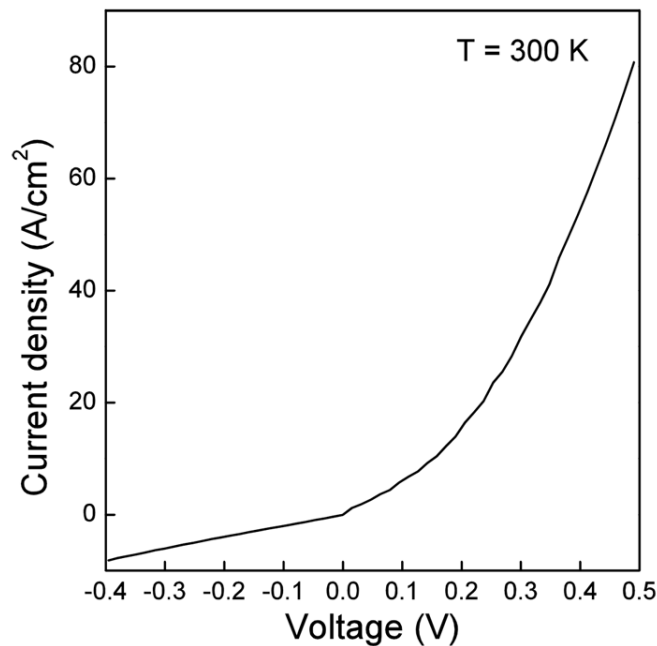


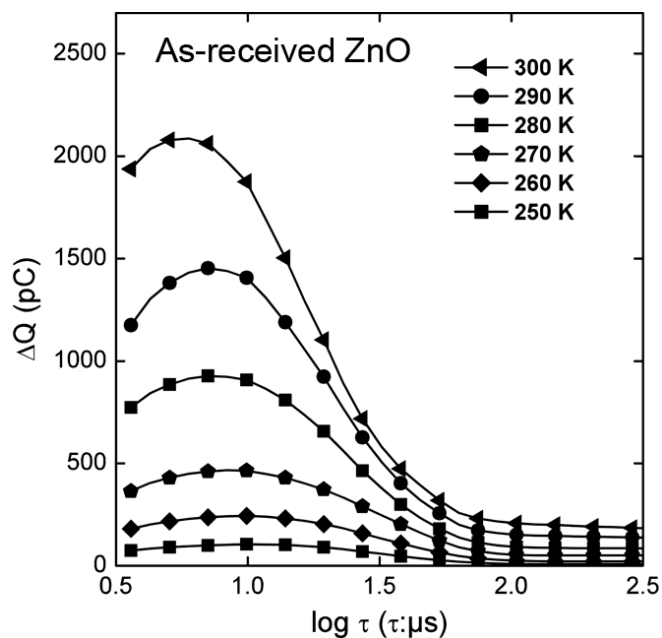
Figure 5.8: $I - V$ characteristic curve of Au Schottky contacts deposited on the H-doped ZnO crystals measured at 300 K.

The Q-DLTS traces for the as-received ZnO crystal at temperatures ranging from 250 K to 290 K are shown in Figure 5.9(a). The spectra were obtained using a charging voltage $\Delta V = 1$ V and charging time $t_c = 1$ s. The Q-DLTS signal of the as-received ZnO becomes negligible at temperatures below 250 K. The peak of the spectra gradually shifts from a longer emission rate to a shorter

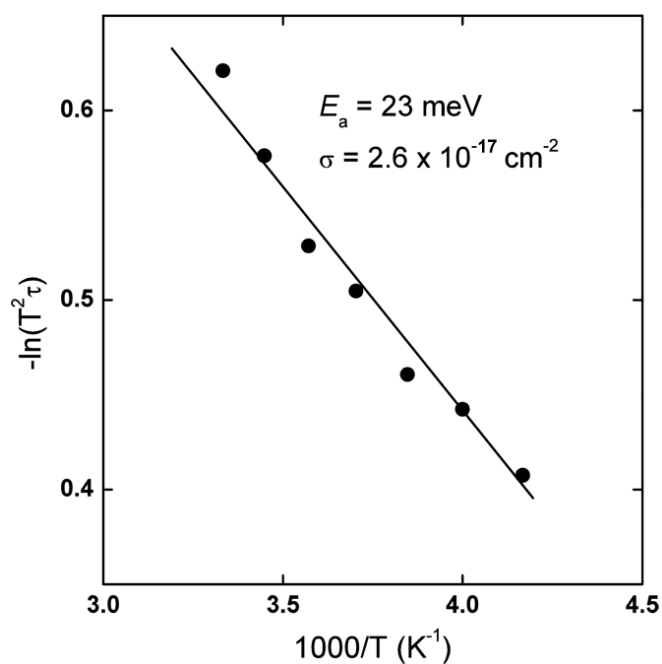
one with increasing temperature. More charge is emitted from the as-received ZnO crystal, which is attributable to the addition of charge being trapped as the free carrier concentration increases with rising temperature. Figure 5.9(b) shows an Arrhenius plot derived from the Q-DLTS spectra. Analysis of the Arrhenius plot using the effective mass $m_e^* = 0.24m_e$ [27] reveals a trap position of $E_a = (23 \pm 2)$ meV and a capture cross section, $\sigma = 2.6 \times 10^{-17} \text{ cm}^{-2}$.

Q-DLTS spectra recorded on the H-doped ZnO crystal at temperatures from 130 K to 290 K are shown in Figure 5.10(a). The traces have a similar shape to those obtained on the as-received ZnO. However, while no Q-DLTS signal was obtained for the as-received crystal at temperatures below 250 K, Q-DLTS spectra were collected at temperatures down to 130 K for the H-doped crystal. The corresponding Arrhenius plot for the H-doped crystal is given in Figure 5.10(b). The Arrhenius plot shows the presence of two linear regions with different slopes, with a distinct break occurring at ~ 220 K which is approximately the same temperature at which the Q-DLTS signal in the as-grown crystal completely disappears. Two defect states can be determined from the slopes of the Arrhenius plot with activation energies E_a of (22 ± 4) meV and (11 ± 2) meV with capture cross sections σ of $4.3 \times 10^{-17} \text{ cm}^{-2}$ and $3.9 \times 10^{-17} \text{ cm}^{-2}$ respectively.

To index Q-DLTS peaks, the subscript of E is used to indicate the energy level of a trap in meV. The activation energy of the E_{22} state is within the experimental error of the state energy for the as-grown crystal (E_{23}); both can therefore be assigned to the same trap. The slight increase in the capture cross section of the E_{23} trap after hydrogen plasma might be due to the reduction in the number of competitive traps as the ZnO crystals surface is passivated by hydrogen. The lower energy state at 11 meV in the H-doped ZnO crystal is attributed to a sub-surface state introduced by the hydrogen plasma. While Q-DLTS itself cannot determine whether carriers in this trap are thermally activated to the valence band or conduction band, the coincidence of the H-related shallow state formation and the increase in electron density as revealed by the Hall effect measurement (see



(a) Q-DLTS spectra



(b) Arrhenius plot

Figure 5.9: (a) Q-DLTS spectra obtained from the as-received ZnO crystal in the temperature range of 250 K to 300 K using charging voltage $\Delta V = 1 \text{ V}$ and charging time $t_c = 1 \text{ s}$ (b) Arrhenius plot derived from the data in (a) indicating a state with an average energy of $(23 \pm 2) \text{ meV}$.

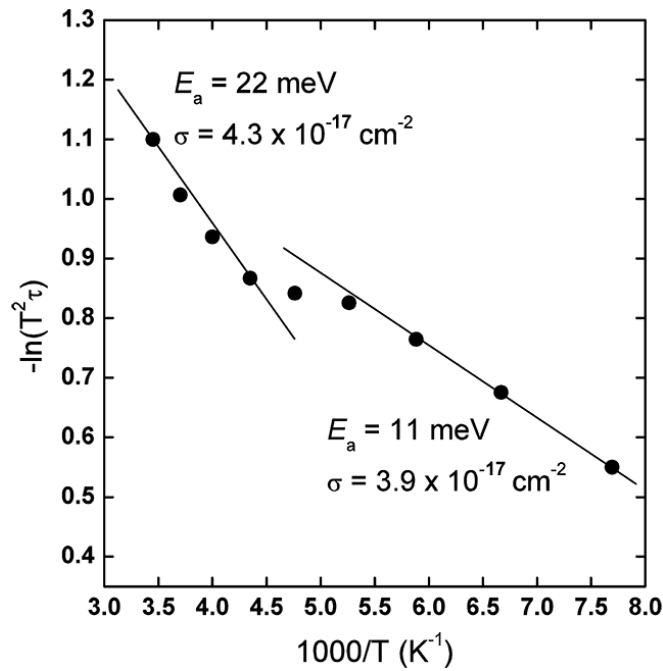
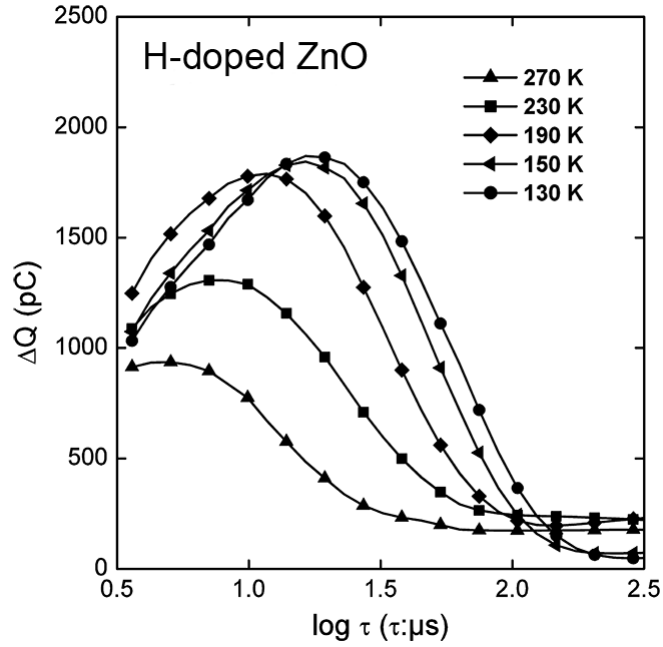


Figure 5.10: (a) Q-DLTS spectra obtained from the H-doped ZnO crystal in the temperature range of 130 K to 290 K using charging voltage $\Delta V = 1$ V and charging time $t_c = 1$ s (b) Arrhenius plot derived from the data in (a) two states with energies of (22 ± 4) meV and (11 ± 2) meV.

Section 4.3) clearly indicate the donor state being responsible for the increased n -type conductivity. It is expected that the Q-DLTS signal in the H-doped ZnO crystal in the temperature range from 130 K to 220 K arises predominantly from the 11 meV trap since the charge released from the deeper trap is negligibly small in this temperature range as shown in Figure 5.9(a).

The Q-DLTS signal can be the result of combination of bulk traps from crystal defects as well as surface states induced by gaseous adsorption. The dominant electron trap in H-doped ZnO is significantly shallower than those detected previously by C-DLTS (20 and 55 meV [191]) but the trap depth is compared favourably to the activation of Y lines associated with structural defects in the near-surface region of ZnO crystals. The activation energy of the Y line obtained from temperature resolved PL measurements on the H-doped crystal is calculated to be 10.2 meV from Figure 5.11. This energy value matches very well with reported activation values of 10 meV to 11 meV for Y lines [137, 192]. The E_{11}

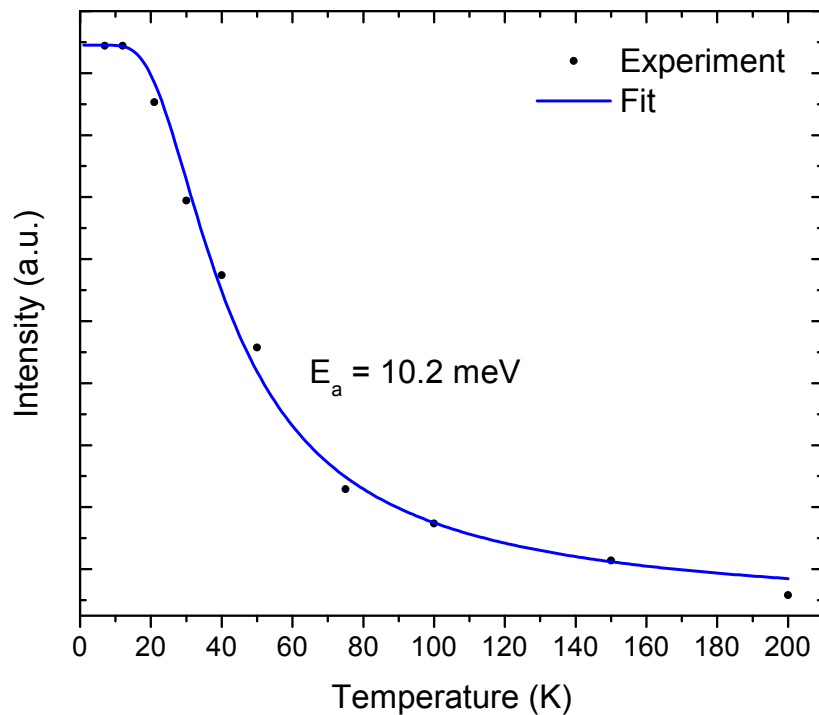


Figure 5.11: Temperature dependence of the PL intensity of the Y line. An activation energy of 10.2 meV was obtained by fitting Equation 5.8 to the data.

trap energy also matches the activation energy of the Y lines well and is much smaller than the ionisation energy of H shallow state ($E_i(H) = 47 \text{ meV}$ to 53 meV [98, 147]) or the localisation energy of Y lines ($E_{loc} \sim 47 \text{ meV}$ [27, 137]).

Both hydrogen and Y line structural defects can introduce additional shallow donor states in ZnO. In highly doped semiconductors, effects such as Burstein-Moss and free-carrier screening could have a prominent influence on the NBE emission. However, these effects are negligible since there is no spectral shift of the BX and FX peaks after H incorporation. Since hydrogen can diffuse up to $1.5 \mu\text{m}$ in the crystal (see Section 4.4.5.2), and the activation energy of the E_{11} trap matches that of the Y lines, the E_{11} can be attributed to Y line structural defects in the near-surface region of the crystal caused by hydrogen plasma. The negative thermal quenching behaviour of the H-doped ZnO (see Section 5.3) can well be explained by a model in which electrons released from the 11 meV trap at temperatures above $\sim 130 \text{ K}$ readily bind with holes to form free excitons, leading to a large enhancement in radiative recombination of FX and its phonon replicas. The proposed mechanism is illustrated in Figure 5.12.

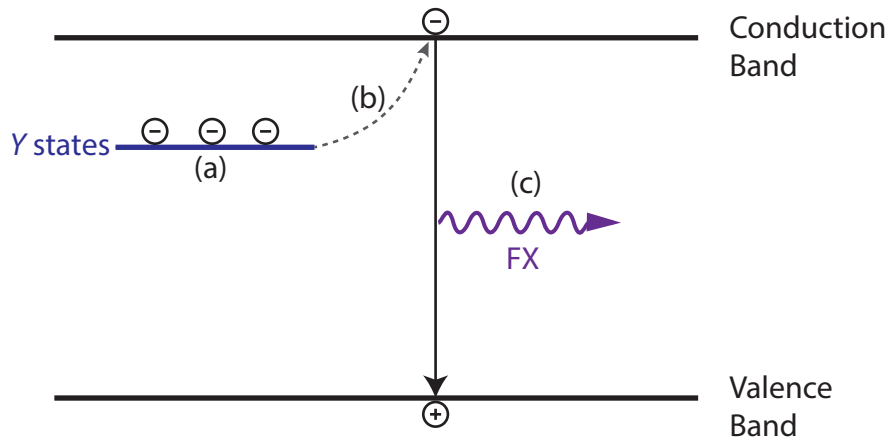


Figure 5.12: Proposed mechanism for the NTQ effect. (a) electrons are trapped at the Y states, (b) electrons are released from the Y states to the conduction band with increasing temperature, (c) the released electron recombines with free holes to form FX luminescence.

5.5 Recombination Kinetics

In addition to simple spectral collection or depth-resolved analysis (see Section 4.4.5), CL can also be used to perform power density dependent measurements. Before doing such measurements, it is necessary to ensure that the electron beam itself does not damage the samples.

Exposing samples to high flux electron beams can lead to electron beam induced damage in the form of atomic displacement arising from elastic collisions (knock-on damage) [193]. There will be a minimum displacement energy, E_d , required to dislodge an ion in the lattice to form a vacancy-interstitial pair. Those displacement energies for Zn and O are 18.5 eV and 41.4 eV respectively [194]. The threshold energy, E_{th} , required for a particle to dislodge an ion from the lattice is [195]:

$$E_{th} = mc^2 \left(\sqrt{1 + \frac{E_d}{2mc^2} \cdot \frac{M}{m}} - 1 \right) \quad (5.10)$$

where m is the mass of the incoming particle, M is the mass of the ion being dislodged, c is the speed of light in vacuum.

From Equation 5.10 and using the appropriate masses for the electron, zinc and oxygen ions, the minimum energy of the electron beam necessary to cause knock on damage is 400 keV for Zn ions and 250 keV for O ions. This energy is much higher than those used in this project and as such direct damage to the samples from the electron beam is not expected to happen.

In power density measurements, the beam energy (hence the CL generation depth) is kept constant while the beam current is varied. By increasing the beam current, a higher number of electron-hole pairs are created as per Equation 4.1. This provides information on the recombination kinetics. Excitons have a typical recombination lifetimes of the order of ps to ns [58, 196], while deep level emissions have recombination times of the order of hundreds of ns to μ s [197, 198].

The CL intensity, I_{CL} , follows a power dependency on the beam current I_b in the following way [199, 200]:

$$I_{CL} \propto I_b^m \quad (5.11)$$

The exponent m can be found by taking the log of Equation 5.11 to obtain:

$$\log I_{CL} \propto m \cdot \log I_b \quad (5.12)$$

A plot of the logarithm of the CL intensity versus the logarithm of the beam current would then be expected to be linear with slope m . This slope is representative of each emission type and gives information about the recombination kinetics and nature of the emission.

For fast recombinations, such as band-to-band or excitonic emission, the value of m is expected to be ≥ 1 [201], while defect related recombination tend to have $m < 1$, with $\frac{1}{2}$ being typical [202, 203]. Furthermore, if the incident electron beam power is producing electron-hole pairs faster than the recombination rate, the emission channel may show saturation effects by exhibiting a non-linear response at higher beam currents.

Figure 5.13 shows the luminescence of the as-received ZnO crystal in the DLE region collected at two different beam currents. At the lower current of 13 pA, the only observable luminescence was the yellow luminescence centered at 1.96 eV and with a FWHM of 0.56 eV; the NBE and green luminescence were completely quenched. The peak parameters of that luminescence are identical to the yellow luminescence in ZnO intentionally doped with lithium (see Section 4.4.4) and show that the yellow luminescence in the as-received crystals are due to lithium impurities. At higher beam currents, the DLE is made up of both the yellow and green components. This can be explained by the difference in recombination lifetimes of the yellow luminescence and green luminescence. The yellow luminescence centres, while being present in higher concentrations than those responsible for the green luminescence, have longer recombination lifetimes in the range of μs

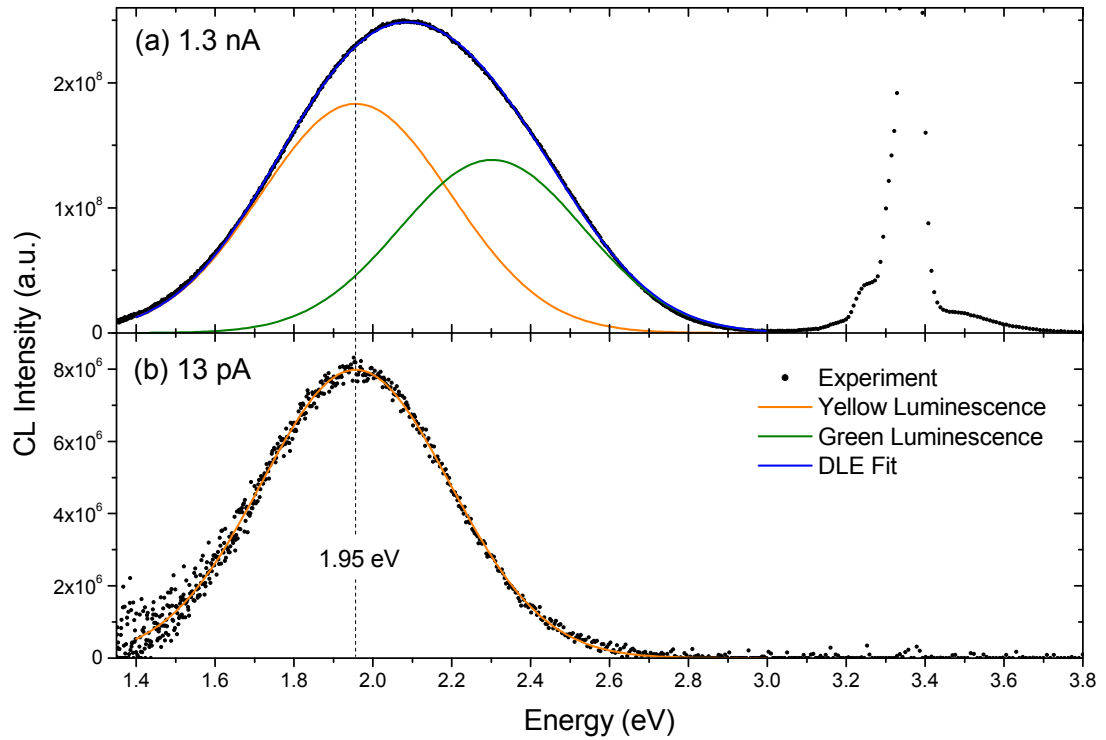


Figure 5.13: Comparison of the DLE of the as-received crystal at a beam current of (a) 1.3 nA and (b) 13 pA taken at 80 K. Fits to the yellow luminescence and green luminescence are also shown for both beam currents. The beam energy was kept at 15 keV.

[198] when compared to the green which is around ~ 100 ns [197]. At lower beam currents, the high concentration of the yellow luminescence centres (typical concentration in hydrothermal grown ZnO $\sim 1 \times 10^{17} \text{ cm}^{-3}$ [204]) makes it the only detected luminescence. While increasing the beam current, the higher recombination lifetime of the yellow luminescence makes it show more saturation effects when compared to the green luminescence. This can explain the luminescence properties of the DLE at higher beam currents.

A series of power dependent CL measurements were also performed on both the as-received and H-doped samples at 10 K, 80 K and 300 K. In all measurements, the beam energy was kept fixed at 15 keV while the beam current was varied from 12 pA to 10 nA. The power dependency of the NBE, yellow and green luminescence peaks was modeled by an $I_{CL} \propto I_b^m$ relationship. Figure 5.14 shows the power dependency of the NBE, yellow luminescence and green luminescence.

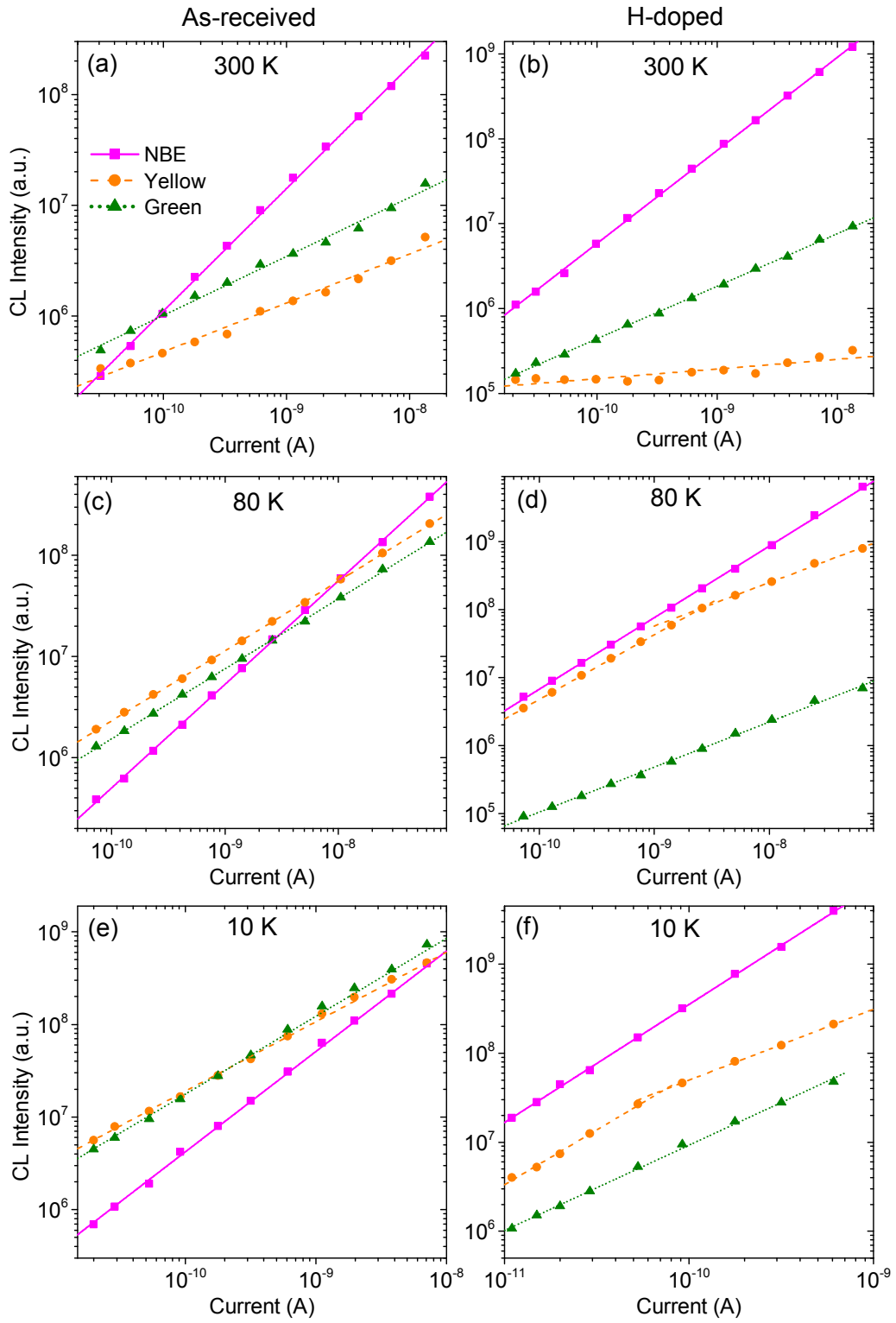


Figure 5.14: Power density measurements of the as-received (a, c, e) and H-doped (b, d, f) crystals at 10 K, 80 K and 300 K. The lines show the power law fit, $I_{CL} \propto I_b^m$, of the data according to Equation 5.11.

The lines are the linear fits to the data with the slope of the lines being the exponent m . The values of m extracted from the fits are summarised in Table 5.2. It can be seen that the NBE luminescence is increased in the H-doped crystal compared to the as-received one and is the most intense luminescence at all temperatures. This result is in accordance to hydrogen forming new shallow donors while passivating defects.

The NBE luminescence for both as-received and H-doped crystals exhibits a linear to super-linear ($m \geq 1$) dependence on the beam power at all temperatures. This behaviour is expected and is typical of radiative transitions involving excitons [201]. The power density behaviour of the yellow and green luminescences however shows high dependencies on temperature.

For the as-received crystals at 300 K, both the yellow and green luminescences show strong sub-linear power dependencies ($m \approx 0.5$). This behaviour is not uncommon and is characteristic of radiative transitions involving deep levels. Such behaviour was observed in other semiconductors and explained through saturation dynamics [200]. Deep-level centres are present in a fixed concentration and have typical recombination times of the order of hundreds of ns to μ s as compared to excitonic recombinations which are of the order of ps. The long recombination time of the DLE is caused by their high coupling to the lattice. Increasing the beam current therefore leads to a saturation of the DLE because they do not depopulate fast enough to respond to the increase of carriers being injected. This is reflected in a sub-linear slope ($m < 1$) of the yellow and green luminescences, confirming that they originate from radiative recombinations involving deep level defects.

In the case of the H-doped crystal at 300 K, the green luminescence still shows a strong sub-linear relationship with $m = 0.62$, while the yellow luminescence is quenched. The quenching of the yellow luminescence is displayed more clearly in Figure 5.15 which shows CL spectra of the as-received and H-doped ZnO taken

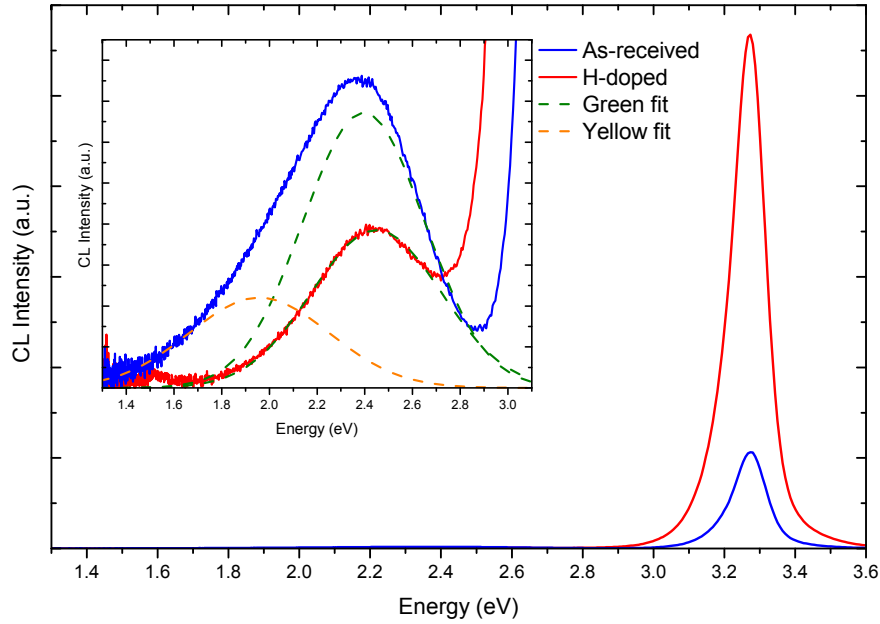


Figure 5.15: CL spectra of the as-received and H-doped crystals taken at 300 K with a beam energy of 15 keV and beam current of 2 nA. Inset shows the DLE with fits for the yellow and green luminescences.

at 300 K. While the low temperature CL did not show any direct interaction between hydrogen species and Li_{Zn} (see Section 4.4.2), it has been reported that hydrogen can form neutral complexes with Li impurities in ZnO crystals with high Li impurity concentration. This can lead to the passivation of Li_{Zn} centres by the formation of neutral $\text{Li}_{\text{Zn}}\text{-H}$ complexes [204–206]. The quenching of the yellow luminescence is therefore attributed to the formation of neutral $\text{Li}_{\text{Zn}}\text{-H}$ complexes.

At 80 K, both the yellow and green luminescence of the as-received crystal show sub linear relationship with beam current. However, the slopes m increase when compared to those at 300 K. After hydrogen doping, the slope of the green luminescence is unchanged while the yellow luminescence exhibits two slopes. At lower beam currents ($I_B < 1$ nA), the yellow luminescence responds linearly with increasing beam current, while at higher beam current ($I_B > 1$ nA), the slope is sub-linear and similar to that of the green luminescence. Hydrogen plasma introduces donors in the ZnO crystals. Since the yellow luminescence

originates from a DAP recombination involving Li_{Zn} , the increase in the donor concentration reduces the distance between the donor and the Li_{Zn} acceptors. This increases the recombination probability and gives rises to a linear slope. At higher beam currents, the yellow luminescence starts to saturate owing to the high recombination time and the slope is sub-linear and comparable to that of the green luminescence.

At 10 K, both the yellow and green luminescence of the as-received crystal again show sub linear relationship with beam current. The increase in the slope when compared to both 300 K and 80 K can be attributed to less donors being ionised, making the recombination more efficient. It is also possible that the DLE at 10 K differs in mechanism to the one at higher temperatures. Namely being of a DAP recombination nature at 10 K while it is a free to bound at higher temperatures. However, after hydrogen doping, the yellow luminescence exhibits two slopes similar to what is observed at 80 K. The green luminescence exhibits a single linear slope after hydrogen doping. The linear slopes after hydrogen doping can be explained by a higher number of donors being introduced in the vicinity of both Li_{Zn} and V_{Zn} , increasing the recombination rate. The two slopes of the yellow luminescence can again be explained in terms of saturation effects with increasing beam currents.

Table 5.2: Coefficients of the power density fit of the NBE, yellow and green luminescences for the as-received and H-doped samples.

| Temperature (K) | | NBE | Yellow | Green |
|-----------------|-------------|-----------------|------------------------------------------------------------------------|-----------------|
| 10 K | As-received | 1.10 ± 0.06 | 0.75 ± 0.03 | 0.84 ± 0.04 |
| | H-doped | 1.32 ± 0.07 | 1.17 ± 0.03 ($I_b < 0.1$ nA) 0.79 ± 0.03 ($I_b > 0.1$ nA) | 1.00 ± 0.04 |
| 80 K | As-received | 1.02 ± 0.05 | 0.69 ± 0.04 | 0.68 ± 0.03 |
| | H-doped | 1.05 ± 0.06 | 0.95 ± 0.03 ($I_b < 1$ nA) 0.64 ± 0.03 ($I_b > 1$ nA) | 0.66 ± 0.04 |
| 300 K | As-received | 1.10 ± 0.04 | 0.44 ± 0.03 | 0.53 ± 0.04 |
| | H-doped | 1.09 ± 0.05 | – ^a | 0.62 ± 0.04 |

^aThe yellow luminescence was quenched after H plasma.

5.6 Characteristics of the Yellow Luminescence

The coupling of electrons to phonon in the yellow luminescence was also studied. Peak position and full width half maximum (FWHM) values for the yellow luminescence of the as-received crystal were found at lower beam powers in the temperature range of 10 K to 250 K. Lower currents were chosen because the yellow luminescence is the dominant emission present at those low current values (see Figure 5.13). Figure 5.16 shows the variation of the FWHM of the yellow luminescence peak with temperature. The experimental FWHM data of the yellow luminescence was fitted to find the Huang-Rhys parameter S using the relationship [207, 208]:

$$\text{FWHM} = 2.36S\hbar\omega\sqrt{\coth\left(\frac{\hbar\omega}{2kT}\right)} \quad (5.13)$$

where $\hbar\omega$ is the mean local photon energy. In the case of strong electron-phonon coupling ($S \gg 1$), S represents the mean number of the emitted phonons for each photon emitted [134]. The larger the value of S , the wider the band and the less resolved are transitions corresponding to different vibration levels. Fitting Equation 5.13 to the data in Figure 5.16 yielded values of $S = 8$ and $\hbar\omega = 31$ meV. Using the peak energy of the yellow luminescence peak at 1.99 eV measured by CL, the calculated Huang-Rhys parameter and local phonon energy, the zero phonon transition for the yellow emission was determined to be at 2.20 eV.

It is believed that the yellow luminescence is dominated by a donor-acceptor pair (DAP) recombination of a shallow donor to a deep Li_{Zn} acceptor at low temperature or a free to bound recombination at high temperatures. The energy of such a DAP transition, E_{DAP} , which is equivalent to the zero phonon line, is given by:

$$E_{DAP} = E_g - E_A - E_D + \frac{e^2}{4\pi\epsilon_0\epsilon_r r} \quad (5.14)$$

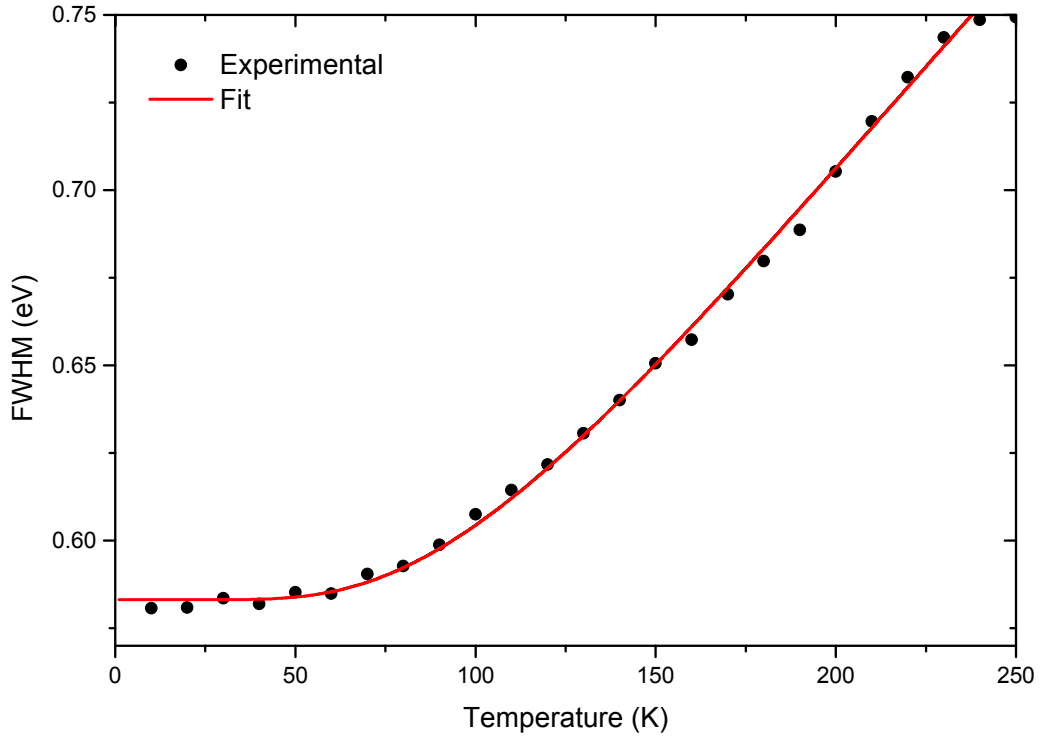


Figure 5.16: Temperature dependence of the FWHM of the yellow luminescence peak of the as-received crystal. The data was fit with Equation 5.13 and yielded a value of $S = 8$.

where E_g is the band gap energy, E_A is the acceptor level energy with respect to the top of the valence band, E_D is the donor level energy with respect to the bottom of the conduction band and the term $e^2/4\pi\epsilon_0\epsilon_r r$ arises from the Coulomb type attraction between ionised acceptor and donor cores.

In ZnO, the band gap energy is 3.437 eV and donors have a mean binding energy, E_D , of 50 meV [27]. In highly n -type materials, the distance r between the donor and acceptor in the DAP can be estimated from the number of donors N_D according to [209]:

$$r^3 \sim \frac{3}{4\pi N_D} \quad (5.15)$$

For the as-received crystal, the donor concentration, N_D , was measured by Hall measurements (see Section 4.3) to be $2.1 \times 10^{14} \text{ cm}^{-3}$ and consequently the mean

distance between the donor-acceptor pair was calculated to be ~ 50 nm. The acceptor binding energy, E_A , for the yellow luminescence was then calculated to be 1.18 eV above the conduction band maximum. This energy is comparable to acceptor energies of Li_{Zn} found by first principle calculations [210] and experimentally through electron spin resonance measurements [50]. This shows that the yellow luminescence in the crystals originates from a radiative transition involving Li_{Zn} centres.

A similar analysis for the green luminescence was not achieved because it was not possible to isolate the green luminescence owing to overlaps with the yellow luminescence and the tail from the NBE luminescence with increasing temperature.

5.7 Stability of Hydrogen Under the Electron Beam in ZnO

The stability of hydrogen dopants and defect complexes involving hydrogen under the electron beam was investigated in this work. As-received and H-doped ZnO crystals were exposed to a low energy electron beam irradiation (LEEBI) while simultaneously monitoring the CL from the crystals.

LEEBI runs were performed on the as-received and H-doped ZnO crystals with doping done at 200 °C to investigate the stability of the luminescence centres under the electron beam. To maximise the effect of LEEBI, a high electron beam power density was used. The electron beam energy was set at 30 keV while the beam current was set to a high injection rate of 250 nA, with the beam stationary during irradiation. These beam conditions are much harsher than those used in the power density CL measurements in Section 5.5 by about two orders of magnitude.

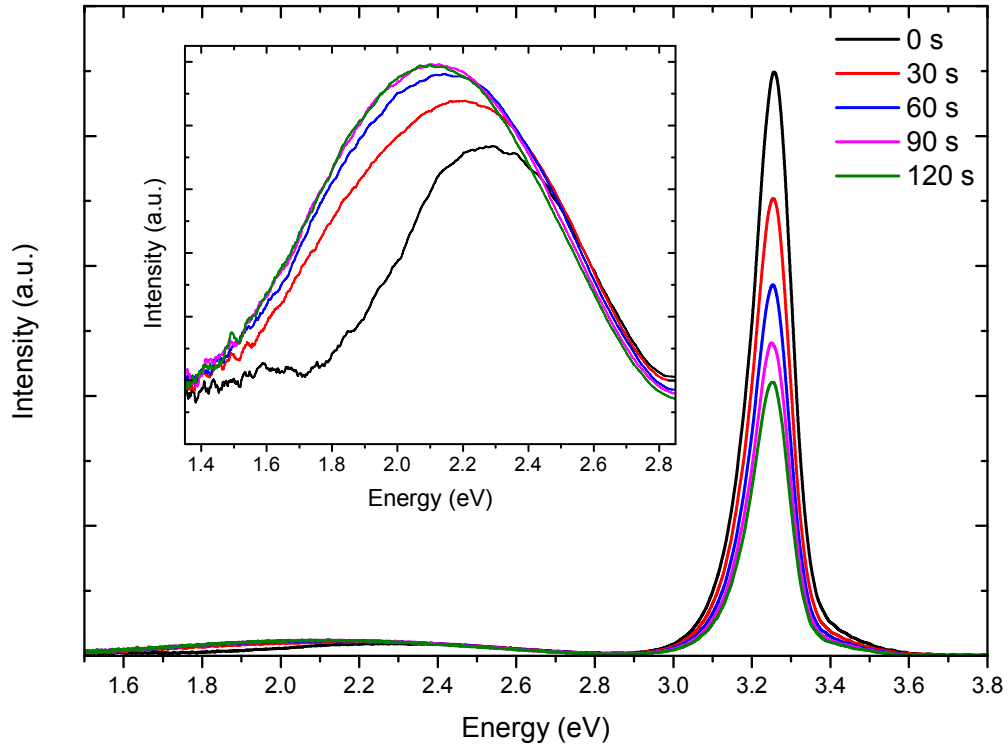


Figure 5.17: CL spectra of the H-doped ZnO crystal at irradiation time ranging from 0 s to 120 s. The inset shows a magnified view of the DLE. Spectra were taken at 300 K with beam energy 30 kV and beam current 250 nA while the beam was stationary.

Figure 5.17 shows CL spectra taken on the H-doped crystal under electron beam irradiation at 30 s intervals at 300 K. The NBE luminescence is significantly reduced after 120 s of irradiation. The DLE red-shifts from 2.32 eV to 2.10 eV after the same irradiation time.

To further analyse and quantify the LEEBI effect, the integrated intensities of the NBE and those of the deconvolved yellow and green luminescences were extracted from the spectra taken at 100 ms intervals and are presented in Figure 5.18. It can be seen that LEEBI has a significant effect on all three luminescences investigated. The NBE luminescence is reduced by 40 %, the green luminescence is halved while the yellow luminescence is nearly tripled after 120 s of irradiation. To be able to explain the LEEBI results, it must be considered that hydrogen is

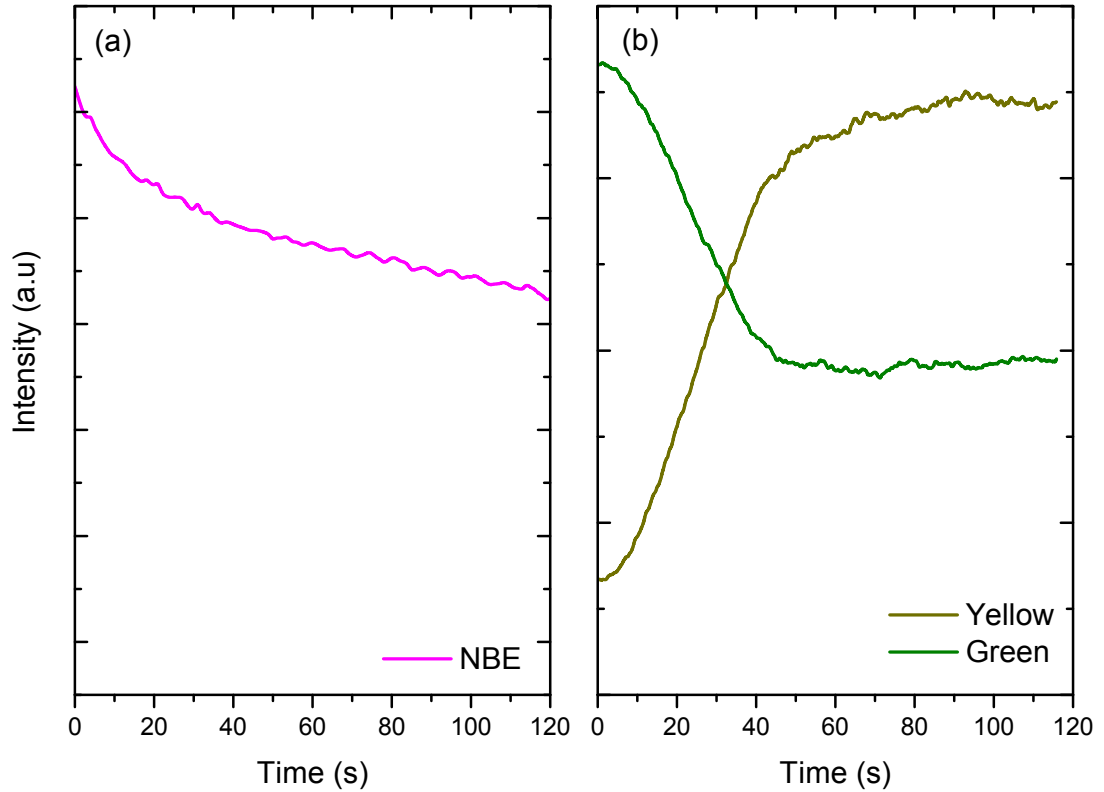


Figure 5.18: Integrated intensities of (a) the NBE luminescence and (b) the yellow and green luminescences of the H-doped ZnO crystal as a function of LEEBI time taken at 300 K. Data points were taken at 100 ms interval.

present in the crystal in possibly three configurations, hydrogen interstitial (H_i), hydrogen complexing with zinc vacancies ($V_{Zn}-H_2$), and hydrogen attached to lithium on a zinc site ($Li_{Zn}-H$). The diffusion barrier for H_i has been reported to be in the range of 0.1 eV to 0.5 eV [123–125], the dissociation energy of the $V_{Zn}-H_2$ complex has been reported to be 1.8 eV [64], and the dissociation energy of the $Li_{Zn}-H$ complex has been reported to be 2.5 eV [211]. There are several mechanisms by which these binding energies may be overcome during LEEBI:

1. elastic collisions and momentum transfer between injected electrons and H impurities.
2. re-absorption of band edge emission (3.37 eV at 300 K) [212].
3. electromigration of species under localised electric field.

4. localised beam heating.

Re-absorption of the band edge emission can be ruled out because no sign of such effects was seen in depth-resolved CL measurements. The decrease in the NBE luminescence can be attributed to mobile H_i being removed from the interaction volume from the electric fields in the crystal's surface induced by the beam [213]. While the carrier concentration of the H-doped crystals increases after hydrogen plasma, the bulk of the crystals have lower carrier concentrations. It is known that electron irradiation of semi- or insulating materials can lead to the formation of a charged double layer [214]. In the near surface region, electrons generated within the secondary electron escape depth are emitted from the surface, leaving behind a positively charged thin layer. Deeper in the sample, excess electrons from the main beam are trapped and this region develops a negative charge. The two regions set up a strong dipole field capable of facilitating electromigration of mobile defects such as H_i .

The increase in the yellow luminescence can be explained by the dissociation of Li_{Zn} -H complexes under the electron beam. Thermally assisted processes under the influence of electron beams in SEM on ZnO have been reported [215]. It was found that at room temperature, the yellow luminescence is quenched in H-doped ZnO crystals, consistent with the formation of neutral Li_{Zn} -H complexes (see Section 5.5). The dissociation of Li_{Zn} -H complexes to Li_{Zn} impurities can explain the increase in the yellow luminescence. On the other hand, the decrease of the green luminescence can be explained in terms of competition for carriers. The Li_{Zn} centre is a more efficient recombination pathway, therefore the yellow luminescence increases at the expense of the green luminescence. This explanation is further supported because both the intensities of the yellow luminescence and green luminescence reach equilibrium after 40 s of beam irradiation. The increase in the yellow luminescence and the decrease of the green luminescence is also consistent with the red-shift of the DLE from 2.32 eV to 2.10 eV observed from Figure 5.17.

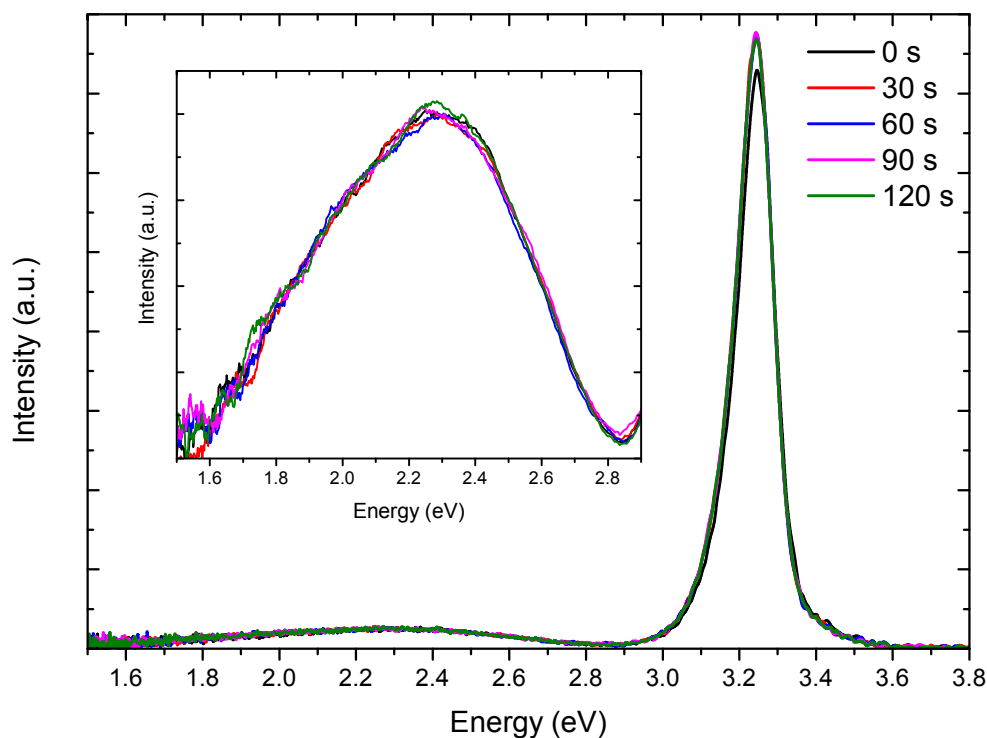


Figure 5.19: CL spectra of the as-received ZnO crystal at irradiation time ranging from 0 s to 120 s. The inset shows a magnified view of the DLE. Spectra were taken at 300 K with beam energy 30 kV and beam current 250 nA and the beam stationary.

To confirm that the LEEBI effects are caused by the migration of hydrogen or dissociation of complexes involving hydrogen, the experiments were repeated on an as-received crystal. Figure 5.19 shows the CL spectra taken on the as-received crystal under electron beam irradiation at 30 s intervals at 300 K. LEEBI does not have such a significant effect on the luminescence of the as-received crystal when compared to the H-doped one. The NBE luminescence is slightly increased while the DLE does not change.

To further analyse the LEEBI data, integrated intensities of the NBE, yellow and green luminescences were extracted from the spectra taken at 100 ms intervals and are presented in Figure 5.20. The NBE luminescence was increased slightly by 4% during the first 30 s and did not change under further irradiation. The slight increase in the NBE luminescence can be explained by localised thermally assisted effects which could be equivalent to a localised annealing of the crystal

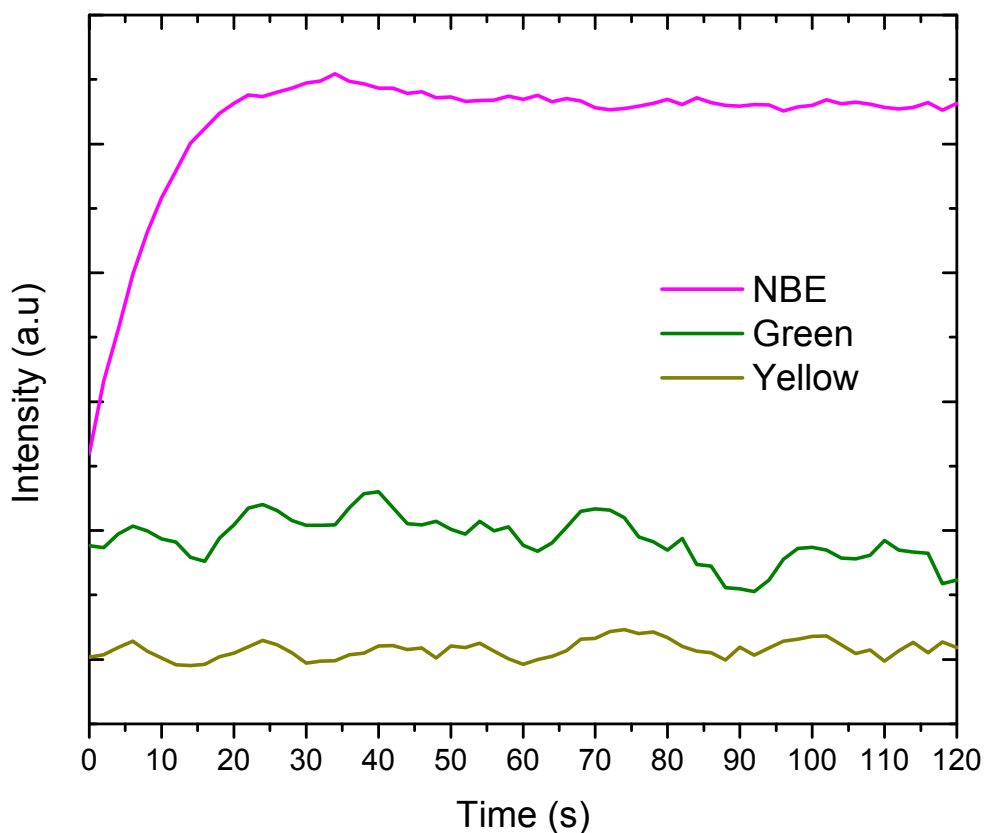


Figure 5.20: Integrated intensities of the NBE luminescence and the yellow and green luminescences of the as-received ZnO crystal as a function of LEEBI time taken at 300 K. Data points were taken at 100 ms interval.

in the interaction volume. Such effects can lead to an improvement in the crystal quality and consequently an increase in the NBE luminescence. The yellow and green luminescence were however practically unchanged over the whole 120 s of irradiation. The variation in the intensities is attributed to the electron beam power not being properly stable over the course of the irradiation run.

To confirm the mechanisms taking place during LEEBI, the irradiation experiments on both the as-received and H-doped ZnO crystals were repeated at 10 K. The evolution of the NBE luminescence for the as-received and H-doped ZnO crystals at both 10 K and 300 K is shown in Figure 5.21. The NBE luminescence of the as-received crystal does not show any change throughout the whole 120 s of irradiation at 10 K. The NBE of the H-doped crystal decreases by 70 % after 120 s of irradiation at 10 K compared to the 40 % decrease at 300 K. By lowering

the temperature, the thermally assisted effects are completely removed. This is evidenced by the near constant intensity of the as-received crystal. Lowering the temperature also reduces scattering of hydrogen species while they are removed from the interaction volume. This is consistent with the intensity of the NBE of the H-doped crystal decreasing faster at lower temperatures.

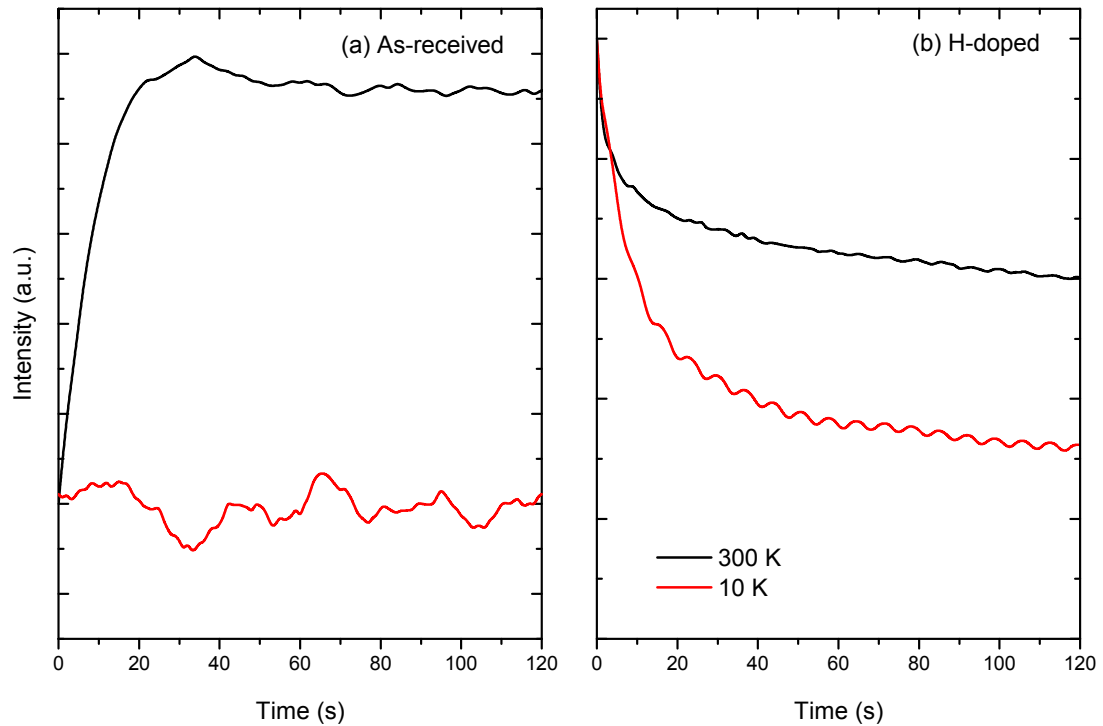


Figure 5.21: Integrated intensities of the NBE luminescence of the (a) H-doped and (b) as-received as a function of LEEBI time taken at 10 K and 300 K. Data points were taken at 100 ms interval.

The intensities of both the yellow and green luminescence remain constant under LEEBI at 10 K as can be seen in Figure 5.22. This indicates that the changes seen in the DLE at 300 K involve thermally assisted processes. At 10 K the beam heating effects are negligible and hence the intensities of the DLE components do not show any changes over time.

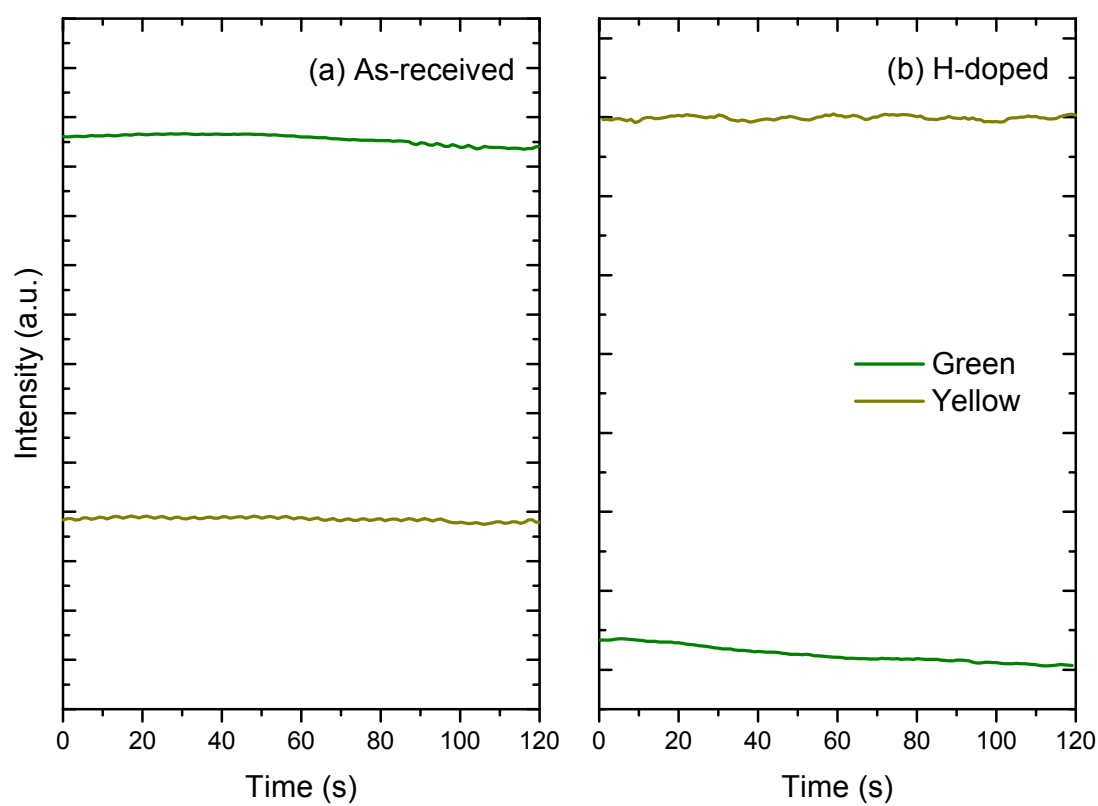


Figure 5.22: Integrated intensities of the yellow and green luminescence of the (a) as-received and (b) H-doped crystals as a function of LEEBI time taken at 10 K. Data points were taken at 100 ms interval.

5.8 Summary

It was found that the main luminescence at high temperature is dominated by the phonon replica of the free exciton and not the free exciton luminescence itself. Moreover, while the as-received crystals show a normal thermal quenching of the intensity of the NBE luminescence with increasing temperature, the H-doped crystal exhibits a so-called negative thermal quenching from 130 K to 320 K. In samples showing this NTQ behaviour, the intensity of the luminescence tends to increase with increasing temperature.

An analysis of shallow carrier traps in the as-received ZnO revealed only one charge trap with activation energy of 23 meV. The H-doped crystal exhibits two carrier traps, one with activation energy of 22 meV and another at 11 meV. Moreover, the activation energy of the *Y* lines was found to be 10.2 meV from temperature resolved PL measurements. The mechanism for the NTQ is attributed to hydrogen introducing charge traps at the *Y* lines which then get thermally ionised at 130 K, releasing electrons which then bind with holes to form free excitons. This leads to the increase in the NBE luminescence.

The recombination kinetics of the luminescence were also investigated. The NBE emission shows the expected linear to super-linear relation to beam current in both the as-received and H-doped crystals. The recombination kinetics of the yellow and green luminescences however show strong temperature dependencies. They exhibit a sub-linear relationship at 300 K which then becomes linear with decreasing temperature. This is explained by more shallow donors available at lower temperatures to take part in radiative recombination.

The characteristics of the yellow luminescence was analysed by temperature resolved CL. The peak properties of the yellow luminescence in the as-received ZnO crystals are identical to the yellow luminescence observed in lithium doped ZnO.

The origin of the yellow luminescence is then attributed to radiative recombinations involving Li_{Zn} impurities.

Finally, the stability of hydrogen species under high current electron beam irradiation was investigated. Electromigration of hydrogen donors was observed which leads to a decrease in the intensity of the NBE emission in H-doped ZnO. Dissociation of neutral $\text{Li}_{\text{Zn}}\text{-H}$ complexes to form Li_{Zn} was also observed and this was detected by an increase in the yellow luminescence at the expense of the green. At 10 K only the electromigration of hydrogen donors is observed.

Chapter 6

Conclusions and Future Directions

6.1 Conclusions

The overall aim of this project was to elucidate the role of hydrogen as a shallow donor and defect passivator in ZnO. This was achieved by assessing the key objectives of the research project which were to investigate:

- the effects of hydrogen on the luminescence and electronic properties of ZnO.
- the interaction of hydrogen with native defects and impurities.
- the spatial distribution of luminescence centres and defect related emissions in ZnO and their origins.
- the stability of hydrogen in ZnO.

The work reported in the previous chapters addressed these objectives and can be summarised as follows.

Incorporation of hydrogen dopants into *a*-plane ZnO crystals at low temperature was achieved through exposure of the crystals to a hydrogen RF plasma source. The low temperature at which the sample is kept during the hydrogen incorporation ensures minimal native defect creation in the crystals. Incorporation of hydrogen in the crystals was confirmed by XPS measurements which revealed an increase in hydrogenated oxygen ions. Penetration and diffusion depths of hydrogen was estimated from depth-resolved cathodoluminescence. Hydrogen was found to diffuse to at least a depth of 1.5 μm .

The carrier concentration was increased from $2.1 \times 10^{14} \text{ cm}^{-3}$ to $2.8 \times 10^{16} \text{ cm}^{-3}$ following hydrogen incorporation and was attributed to the formation of H-related shallow donors. Consequently, the intensity of the donor bound exciton was also increased following hydrogen plasma while the intensity of the free exciton remained unchanged. High resolution PL analysis of the BX spectral region reveals that the intensity of both the I_4 and $I_{4a,b}$ emissions increase after hydrogen incorporation suggesting that hydrogen dopants introduced by the plasma are in a different chemical state to those incorporated during the hydrothermal growth. PL also showed that the intensity of the peak at 3.3363 eV increases after plasma incorporation. This peak called the *Y* line, is associated to extended structural defects which have been created at the surface during plasma treatment. Temperature dependent PL measurements determined the activation energy of the *Y* line to be $\sim 10.2 \text{ meV}$.

The NBE luminescence of the H-doped crystal exhibits negative thermal quenching from 130 K to 320 K, whereby the intensity of the emission increases with increasing temperature. An analysis of shallow carrier traps in the as-received ZnO revealed only one charge trap with activation energy of 23 meV. The H-doped crystal showed the presence of two carrier traps, one with activation energy of 22 meV and another at 11 meV. The mechanism for the NTQ is attributed to hydrogen introducing charge traps at the *Y* lines which then get thermally ionised at 130 K, releasing electrons which then bind with holes to form free excitons.

The defect luminescence commonly found in ZnO was also highly affected by hydrogen incorporation. The green luminescence was quenched after hydrogen plasma while the yellow luminescence was slightly increased. The green luminescence is thought to originate from a transition involving zinc vacancies. The passivation of the green luminescence is attributed to hydrogen forming neutral $V_{\text{Zn}}\text{-H}_2$ complexes. This complex is made up of two hydrogen bonding to oxygen at the zinc vacancy site. XPS results show an increase in hydrogenated oxygen after plasma, consistent with the formation of $V_{\text{Zn}}\text{-H}_2$ complexes. The yellow luminescence in the as-received crystals is identical to that in lithium doped ZnO and is attributed to a radiative recombination involving Li_{Zn} impurities.

The recombination kinetics of the luminescence were also investigated. The NBE emission shows the expected linear to super-linear relation to beam current in both the as-received and H-doped crystals. The recombination kinetics of the yellow and green luminescences however show strong temperature dependencies. They exhibit a sub-linear relationship at 300 K which then becomes linear with decreasing temperature. This is explained by more shallow donors available at lower temperatures to take part in radiative recombination.

XANES results showed that hydrogen interacts only with oxygen atoms in the lattice and not zinc. This indicates that most of the interstitial hydrogen incorporated by plasma treatment sit at the anti-bonding site of the oxygen atom, with the hydrogen attached to a host oxygen atom and pointing away from the Zn–O bond.

Finally, the stability of hydrogen species under high current electron beam irradiation was investigated. Electromigration of hydrogen donors was observed which leads to a decrease in the intensity of the NBE emission in H-doped ZnO. Dissociation of neutral $\text{Li}_{\text{Zn}}\text{-H}$ complexes to form Li_{Zn} was also observed and this was detected by an increase in the yellow luminescence at the expense of the green. At 10 K only the electromigration of hydrogen donors is observed while

the yellow and green luminescence remained constant throughout the irradiation time. This indicates that dissociation of the $\text{Li}_{\text{Zn}}\text{-H}$ complexes at 300 K involves thermally assisted processes.

6.2 Future Directions

There are some areas touched on during the course of this work that could be the focus for further research. Nanostructures, such as nanoparticles and nanowires, are known to have significantly different optical properties to bulk material owing to their high surface to volume ratio. As plasma treatment is primarily a surface modification technique, it would be interesting to investigate the optical properties of nanostructured ZnO following plasma treatments in hydrogen or other gaseous environments.

It is thought that hydrogen is the cause of the intrinsic *n*-type character of as-grown ZnO. LEEBI experiments have shown that hydrogen dopants are not stable under electron irradiation. This property can be used to control and modify the concentration of hydrogen impurities in ZnO. Intentional co-doping with hydrogen could possibly stabilise acceptors in the lattice and subsequent removal of the hydrogen can lead to successful *p*-type doping, similar to what is done in GaN with Mg-H complexes.

From an experimental point of view, studying the incorporation of hydrogen and its effects on the optical and electrical properties in-situ would be an advantage. It is possible that changes to the optical and electrical properties are affected by exposure to air due to surface adsorption of impurities. Doing the incorporation and characterisation without breaking vacuum in a scanning microscope would be an interesting project in itself.

6.3 Closing Remarks

ZnO remains a material with potential application in various optoelectronic devices and technologies. The ultimate goal is to develop high quality devices based on ZnO. The main hurdle to achieving those devices is the challenge of manufacturing high quality *p*-type ZnO. However, the work done in this thesis shows that hydrogen doped ZnO offers improved optical properties over as-grown ZnO. This could be used in high quality optical devices. I believe that it is only a matter of time before ZnO emerges as one of most important solid state lighting materials. I hope that work done throughout this thesis has contributed to the understanding of the hurdles holding back ZnO.

Bibliography

- [1] Becheri, A., Durr, M., Lo Nostro, P., and Baglioni, P. Synthesis and characterization of zinc oxide nanoparticles: application to textiles as UV-absorbers. *Journal of Nanoparticle Research*, 10(4):679–689, 2008.
- [2] Serpone, N., Dondi, D., and Albin, A. Inorganic and organic UV filters: Their role and efficacy in sunscreens and sun care products. *Inorganica Chimica Acta*, 360(3):794–802, 2007.
- [3] Carcia, P. F., McLean, R. S., Reilly, M. H., and Nunes, G. Transparent ZnO thin-film transistor fabricated by rf magnetron sputtering. *Appl. Phys. Lett.*, 82(7):1117, 2003.
- [4] Hoffman, R. L., Norris, B. J., and Wager, J. F. ZnO-based transparent thin-film transistors. *Appl. Phys. Lett.*, 82(5):733, 2003.
- [5] Lim, J.-H., Kang, C.-K., Kim, K.-K., Park, I.-K., Hwang, D.-K., and Park, S.-J. UV Electroluminescence Emission from ZnO Light-Emitting Diodes Grown by High-Temperature Radiofrequency Sputtering. *Advanced Materials*, 18(20):2720, 2006.
- [6] Choi, Y.-S., Kang, J.-W., Hwang, D.-K., and Park, S.-J. Recent Advances in ZnO-Based Light-Emitting Diodes. *Electron Devices, IEEE Transactions on*, 57(1):26–41, 2010.
- [7] Huang, M. H., Mao, S., Feick, H., Yan, H., Wu, Y., Kind, H., Weber, E., Russo, R., and Yang, P. Room-temperature ultraviolet nanowire nanolasers. *Science*, 292(5523):1897–9, 2001.
- [8] Li, H.-Y., Rühle, S., Khedoe, R., Koenderink, A. F., and Vanmaekelbergh, D. Polarization, microscopic origin, and mode structure of luminescence and lasing from single ZnO nanowires. *Nano letters*, 9(10):3515–20, 2009.
- [9] Kavitha, R. and Jayaram, V. Band-Gap Engineering in ZnO-MgO Films Prepared by Combustion Flame Pyrolysis of Solution Precursors. *Journal of Electronic Materials*, 36(10):1326–1332, 2007.

- [10] Ku, C. H., Chiang, H. H., and Wu, J. J. Bandgap engineering of well-aligned Zn_{1-x}Mg_xO nanorods grown by metalorganic chemical vapor deposition. *Chemical Physics Letters*, 404(1-3):132–135, 2005.
- [11] Santana, G., Morales-Acevedo, A., Vigil, O., Vaillant, L., Cruz, F., and Contreras-Puente, G. Structural and optical properties of (ZnO)_x(CdO)_{1-x} thin films obtained by spray pyrolysis. *Thin Solid Films*, 373(1-2):235–238, 2000.
- [12] Fuller, M. L. A method of determining the axial ratio of a crystal from x-ray diffraction data: the axial ratio and lattice constants of zinc oxide. *Science*, 70(1808):196–8, 1929.
- [13] Dierre, B., Yuan, X. L., Yao, Y. Z., Yokoyama, M., and Sekiguchi, T. Impact of electron beam irradiation on the cathodoluminescence intensity for ZnO and GaN. *Journal of Materials Science: Materials in Electronics*, 19(S1):307–310, 2008.
- [14] Yan, H., Johnson, J., Law, M., He, R., Knutsen, K., McKinney, J., Pham, J., Saykally, R., and Yang, P. ZnO Nanoribbon Microcavity Lasers. *Advanced Materials*, 15(22):1907–1911, 2003.
- [15] Chu, S., Wang, G., Zhou, W., Lin, Y., Chernyak, L., Zhao, J., Kong, J., Li, L., Ren, J., and Liu, J. Electrically pumped waveguide lasing from ZnO nanowires. *Nature nanotechnology*, 6(8):506–10, 2011.
- [16] Zhang, Y., Russo, R. E. R., and Mao, S. S. S. Quantum efficiency of ZnO nanowire nanolasers. *Applied Physics Letters*, 87(4):043106, 2005.
- [17] Coskun, C., Look, D. C., Farlow, G. C., and Szelove, J. R. Radiation hardness of ZnO at low temperatures. *Semiconductor Science and Technology*, 19(6):752–754, 2004.
- [18] Polyakov, a. Y., Smirnov, N. B., Govorkov, a. V., Kozhukhova, E. a., Vdovin, V. I., Ip, K., Overberg, M. E., Heo, Y. W., Norton, D. P., Pearton, S. J., Zavada, J. M., and Dravin, V. a. Proton implantation effects on electrical and recombination properties of undoped ZnO. *Journal of Applied Physics*, 94(5):2895, 2003.
- [19] Kim, A., Won, Y., Woo, K., Kim, C.-h., and Moon, J. Highly Transparent Low Resistance ZnO/Ag Nanowire/ZnO Composite Electrode for Thin Film Solar Cells. *ACS nano*, 7(2):1081–91, 2013.
- [20] Matsubara, K., Fons, P., Iwata, K., Yamada, a., Sakurai, K., Tampo, H., and Niki, S. ZnO transparent conducting films deposited by pulsed laser deposition for solar cell applications. *Thin Solid Films*, 431-432:369–372, 2003.

- [21] Jaffe, J. E. and Hess, A. C. Hartree-Fock study of phase changes in ZnO at high pressure. *Physical review. B, Condensed matter*, 48(11):7903–7909, 1993.
- [22] Wang, Z. L. Zinc oxide nanostructures: growth, properties and applications. *Journal of Physics: Condensed Matter*, 16(25):R829–R858, 2004.
- [23] Woll, C. The chemistry and physics of zinc oxide surfaces. *Progress in Surface Science*, 82(2-3):55–120, 2007.
- [24] Du, M. H., Zhang, S. B., Northrup, J. E., and Erwin, S. C. Stabilization mechanisms of polar surfaces: ZnO surfaces. *Phys. Rev. B*, 78(15):155424–155427, 2008.
- [25] Laskowski, R. and Christensen, N. Ab initio calculation of excitons in ZnO. *Physical Review B*, 73(4):045201, 2006.
- [26] Cobet, M., Cobet, C., Wagner, M. R., Esser, N., Thomsen, C., and Hoffmann, A. Polariton effects in the dielectric function of ZnO excitons obtained by ellipsometry. *Applied Physics Letters*, 96(3):031904, 2010.
- [27] Meyer, B. K., Alves, H., Hofmann, D. M., Kriegseis, W., Forster, D., Bertram, F., Christen, J., Hoffmann, A., Straßburg, M., Dworzak, M., Habocek, U., and Rodina, A. V. Bound exciton and donor-acceptor pair recombinations in ZnO. *Phys. Status Solidi B*, 241(2):231–260, 2004.
- [28] Janotti, A. and Van de Walle, C. G. Fundamentals of zinc oxide as a semiconductor. *Reports on Progress in Physics*, 72(12):126501, 2009.
- [29] Varshni, Y. Temperature dependence of the energy gap in semiconductors. *Physica*, 34(1):149–154, 1967.
- [30] Jagadish, C. and Pearton, S. J. *Zinc Oxide Bulk, Thin Films and Nanostructures: Processing, Properties, and Applications*. Elsevier Science, 1 edition, 2006.
- [31] Janotti, A. and Van de Walle, C. G. Oxygen vacancies in ZnO. *Applied Physics Letters*, 87(12):122102, 2005.
- [32] Pfisterer, D., Sann, J., Hofmann, D. M., Meyer, B., Frank, T., Pensl, G., Tena-Zaera, R., Zúñiga Pérez, J., Martínez-Tomas, C., and Muñoz Sanjosé, V. Negative U-properties of the oxygen-vacancy in ZnO. *Physica Status Solidi (C)*, 3(4):997–1000, 2006.
- [33] Erhart, P., Klein, A., and Albe, K. First-principles study of the structure and stability of oxygen defects in zinc oxide. *Physical Review B*, 72(8):085213, 2005.

- [34] Paudel, T. and Lambrecht, W. First-principles calculation of the O vacancy in ZnO: A self-consistent gap-corrected approach. *Physical Review B*, 77(20):205202, 2008.
- [35] Erhart, P., Albe, K., and Klein, A. First-principles study of intrinsic point defects in ZnO: Role of band structure, volume relaxation, and finite-size effects. *Physical Review B*, 73(20):205203, 2006.
- [36] Oba, F., Togo, A., and Tanaka, I. Defect energetics in ZnO: A hybrid Hartree-Fock density functional study. *Physical Review B*, 77(24):245202, 2008.
- [37] Janotti, A. and Van de Walle, C. G. Hydrogen multicentre bonds. *Nat. Mater.*, 6(1):44–47, 2007.
- [38] Lany, S. and Zunger, A. Dopability, Intrinsic Conductivity, and Nonstoichiometry of Transparent Conducting Oxides. *Physical Review Letters*, 98(4):045501, 2007.
- [39] Janotti, A. and Van De Walle, C. Native point defects in ZnO. *Phys. Rev. B*, 76(16):165202, 2007.
- [40] Vanheusden, K., Warren, W. L., Seager, C. H., Tallant, D. R., Voigt, J. A., and Gnade, B. E. Mechanisms behind green photoluminescence in ZnO phosphor powders. *J. Appl. Phys.*, 79(10):7983, 1996.
- [41] Vlasenko, L. and Watkins, G. Optical detection of electron paramagnetic resonance in room-temperature electron-irradiated ZnO. *Physical Review B*, 71(12):125210, 2005.
- [42] Hofmann, D., Pfisterer, D., Sann, J., Meyer, B., Tena-Zaera, R., Munoz-Sanjose, V., Frank, T., and Pensl, G. Properties of the oxygen vacancy in ZnO. *Applied Physics A*, 88(1):147–151, 2007.
- [43] Kohan, A. F., Ceder, G., Morgan, D., Van De Walle, C., and de Walle, C. G. V. First-principles study of native point defects in ZnO. *Phys. Rev. B*, 61(22):15019–15027, 2000.
- [44] Evans, S. M., Giles, N. C., Halliburton, L. E., and Kappers, L. a. Further characterization of oxygen vacancies and zinc vacancies in electron-irradiated ZnO. *Journal of Applied Physics*, 103(4):043710, 2008.
- [45] Sekiguchi, T., Ohashi, N., and Terada, Y. Effect of Hydrogenation on ZnO Luminescence. *Jpn. J. Appl. Phys.*, 36(Part 2, No. 3A):L289–L291, 1997.
- [46] Look, D., Farlow, G., Reunchan, P., Limpijumnong, S., Zhang, S., and Nordlund, K. Evidence for Native-Defect Donors in n-Type ZnO. *Physical Review Letters*, 95(22):225502, 2005.

- [47] Sann, J., Stehr, J., Hofstaetter, a., Hofmann, D., Neumann, a., Lerch, M., Haboek, U., Hoffmann, a., and Thomsen, C. Zn interstitial related donors in ammonia-treated ZnO powders. *Physical Review B*, 76(19):195203, 2007.
- [48] Sun, Y. and Wang, H. The electronic properties of native interstitials in ZnO. *Physica B: Condensed Matter*, 325:157–163, 2003.
- [49] Dingle, R. Luminescent Transitions Associated With Divalent Copper Impurities and the Green Emission from Semiconducting Zinc Oxide. *Phys. Rev. Lett.*, 23(11):0, 1969.
- [50] Schirmer, O. and Zwingel, D. The yellow luminescence of zinc oxide. *Solid State Commun.*, 8(19):1559–1563, 1970.
- [51] Van de Walle, C. G. Defect analysis and engineering in ZnO. *Physica B: Condensed Matter*, 308-310:899–903, 2001.
- [52] Yacobi, B. G. *Semiconductor Materials: An Introduction to Basic Principles*. Microdevices Series. Kluwer Academic Pub, 2003. ISBN 9780306473616.
- [53] Chemla, D., Miller, D., Smith, P., Gossard, A., and Wiegmann, W. Room temperature excitonic nonlinear absorption and refraction in GaAs/AlGaAs multiple quantum well structures. *IEEE Journal of Quantum Electronics*, 20(3):265–275, 1984.
- [54] Mang, A., Reimann, K., and Rübenacke, S. Band gaps, crystal-field splitting, spin-orbit coupling, and exciton binding energies in ZnO under hydrostatic pressure. *Solid state communications*, 94(4):251–254, 1995.
- [55] Toropov, A. A., Nekrutkina, O. V., Shubina, T. V., Gruber, T., Kirchner, C., Waag, a., Karlsson, K. F., and Monemar, B. Temperature-dependent polarized luminescence of exciton polaritons in a ZnO film. *Physica Status Solidi (a)*, 202(3):392–395, 2005.
- [56] Calleja, J. and Cardona, M. Resonant Raman scattering in ZnO. *Physical Review B*, 16(8):3753–3761, 1977.
- [57] Reynolds, D., Litton, C., and Collins, T. Zeeman Effects in the Edge Emission and Absorption of ZnO. *Physical Review*, 140(5A):A1726–A1734, 1965.
- [58] Teke, A., Özgür, U., Doan, S., Gu, X., Morkoç, H., Nemeth, B., Nause, J., and Everitt, H. Excitonic fine structure and recombination dynamics in single-crystalline ZnO. *Physical Review B*, 70(19):195207, 2004.
- [59] Boemare, C., Monteiro, T., Soares, M., Guilherme, J., and Alves, E. Photoluminescence studies in ZnO samples. *Physica B: Condensed ...*, 310:985–988, 2001.

- [60] Ewles, J. Resolution and interpretation of the luminescent spectra of some solids at low temperatures. *Proceedings of the Royal Society of . . .*, 167 (928):34–52, 1938.
- [61] Broser, I., Podlowski, L., Thurian, P., Heitz, R., and Hoffmann, A. Calorimetric absorption spectroscopy of copper centers in IIVI semiconductors at mK temperatures. *Journal of Luminescence*, 60-61:588–591, 1994.
- [62] Vanheusden, K., Seager, C. H., Warren, W. L., Tallant, D. R., and Voigt, J. A. Correlation between photoluminescence and oxygen vacancies in ZnO phosphors. *Appl. Phys. Lett.*, 68(3):403, 1996.
- [63] Leiter, F. H., Alves, H. R., Hofstaetter, A., Hofmann, D. M., and Meyer, B. K. The Oxygen Vacancy as the Origin of a Green Emission in Undoped ZnO. *Phys. Status Solidi B*, 226(1):R4–R5, 2001.
- [64] Wardle, M., Goss, J., and Briddon, P. Theory of Fe, Co, Ni, Cu, and their complexes with hydrogen in ZnO. *Physical Review B*, 72(15):155108, 2005.
- [65] Wang, D., Seo, H. W., Tin, C.-C. C., Bozack, M. J., Williams, J. R., Park, M., Sathitsuksanoh, N., Cheng, A.-j., and Tzeng, Y. H. Effects of postgrowth annealing treatment on the photoluminescence of zinc oxide nanorods. *J. Appl. Phys.*, 99(11):113509, 2006.
- [66] Studenikin, S. a., Golego, N., and Cocivera, M. Fabrication of green and orange photoluminescent, undoped ZnO films using spray pyrolysis. *Journal of Applied Physics*, 84(4):2287, 1998.
- [67] Kwok, W. M., Djuricic, a. B., Leung, Y. H., Chan, W. K., and Phillips, D. L. Time-resolved photoluminescence study of the stimulated emission in ZnO nanoneedles. *Applied Physics Letters*, 87(9):093108, 2005.
- [68] Liu, M., Kitai, a. A., and Mascher, P. Point defects and luminescence centres in zinc oxide and zinc oxide doped with manganese. *Journal of Luminescence*, 54(1):35–42, 1992.
- [69] Greene, L. E., Law, M., Goldberger, J., Kim, F., Johnson, J. C., Zhang, Y., Saykally, R. J., and Yang, P. Low-temperature wafer-scale production of ZnO nanowire arrays. *Angewandte Chemie (International ed. in English)*, 42(26):3031–4, 2003.
- [70] Ohashi, N., Ebisawa, N., Sekiguchi, T., Sakaguchi, I., Wada, Y., Takenaka, T., and Haneda, H. Yellowish-white luminescence in codoped zinc oxide. *Applied Physics Letters*, 86(9):091902, 2005.
- [71] LAUDISE, R. A., KOLB, E. D., and CAPORASO, A. J. Hydrothermal Growth of Large Single Crystals of Zinc Oxide. *Journal of the American Ceramic Society*, 47(1):9–12, 1964.

- [72] Sekiguchi, T., Miyashita, S., Obara, K., Shishido, T., and Sakagami, N. Hydrothermal growth of ZnO single crystals and their optical characterization. *Journal of Crystal Growth*, 214-215:72–76, 2000.
- [73] Demyanets, L. and Lyutin, V. Status of hydrothermal growth of bulk ZnO: Latest issues and advantages. *Journal of Crystal Growth*, 310(5):993–999, 2008.
- [74] Ehrentraut, D., Sato, H. H., Kagamitani, Y., Yoshikawa, A., and Fukuda, T. Solvothermal growth of ZnO. *Progress in Crystal Growth and Characterization of Materials*, 52(4):280–335, 2006.
- [75] Rauch, C., Gehlhoff, W., Wagner, M. R., Malguth, E., Callsen, G., Kirste, R., Salameh, B., Hoffmann, a., Polarz, S., Aksu, Y., and Driess, M. Lithium related deep and shallow acceptors in Li-doped ZnO nanocrystals. *J. Appl. Phys.*, 107(2):024311, 2010.
- [76] Cox, R., Block, D., Hervé, A., Picard, R., Santier, C., and Helbig, R. Exchange broadened, optically detected ESR spectra for luminescent donor-acceptor pairs in Li doped ZnO. *Solid State Communications*, 25(2):77–80, 1978.
- [77] Ehret, W. and Greenstone, A. Red Zinc Oxide. *Journal of the American Chemical Society*, 65(5):872–877, 1943.
- [78] de la Cruz RM, Pareja, R., González, R., Boatner, L., and Chen, Y. Effect of thermochemical reduction on the electrical, optical-absorption, and positron-annihilation characteristics of ZnO crystals. *Physical review. B, Condensed matter*, 45(12):6581–6586, 1992.
- [79] Halliburton, L. E., Giles, N. C., Garces, N. Y., Luo, M., Xu, C., Bai, L., and Boatner, L. a. Production of native donors in ZnO by annealing at high temperature in Zn vapor. *Applied Physics Letters*, 87(17):172108, 2005.
- [80] Selim, F., Weber, M., Solodovnikov, D., and Lynn, K. Nature of Native Defects in ZnO. *Physical Review Letters*, 99(8):085502, 2007.
- [81] Pearton, S. J., Norton, D. P., Ip, K., Heo, Y. W., and Steiner, T. Recent advances in processing of ZnO. *Journal of Vacuum Science & Technology B: Microelectronics and Nanometer Structures*, 22(3):932, 2004.
- [82] Lommens, P., Smet, P. F., de Mello Donega, C., Meijerink, A., Piraux, L., Michotte, S., Mátéfi-Tempfli, S., Poelman, D., and Hens, Z. Photoluminescence properties of Co²⁺-doped ZnO nanocrystals. *Journal of Luminescence*, 118(2):245–250, 2006.
- [83] Weber, M., Parmar, N., Jones, K., and Lynn, K. Oxygen Deficiency and Hydrogen Turn ZnO Red. *Journal of Electronic Materials*, 39(5):573–576, 2010.

- [84] Thomas, D. G. and Lander, J. J. Hydrogen as a Donor in Zinc Oxide. *The Journal of Chemical Physics*, 25(6):1136, 1956.
- [85] Ip, K., Overberg, M. E., Heo, Y. W., Norton, D. P., Pearton, S. J., Stutz, C. E., Luo, B., Ren, F., Look, D. C., and Zavada, J. M. Hydrogen incorporation and diffusivity in plasma-exposed bulk ZnO. *Appl. Phys. Lett.*, 82(3):385, 2003.
- [86] Van De Walle, C. G. Hydrogen as a cause of doping in zinc oxide. *Phys. Rev. Lett.*, 85(5):1012–5, 2000.
- [87] Hofmann, D., Hofstaetter, A., Leiter, F., Zhou, H., Henecker, F., Meyer, B., Orlinskii, S., Schmidt, J., and Baranov, P. Hydrogen: A Relevant Shallow Donor in Zinc Oxide. *Physical Review Letters*, 88(4):045504, 2002.
- [88] McCluskey, M. D. and Jokela, S. J. Sources of n-type conductivity in ZnO. *Physica B: Condensed Matter*, 401-402:355–357, 2007.
- [89] Herklotz, F., Lavrov, E. V., and Weber, J. Photoluminescence study of hydrogen donors in ZnO. *Physica B: Condensed Matter*, 404(22):4349–4353, 2009.
- [90] Lavrov, E. V., Herklotz, F., and Weber, J. Identification of Hydrogen Molecules in ZnO. *Phys. Rev. Lett.*, 102(18):185502, 2009.
- [91] Chan, K. S., Vines, L., Johansen, K. M., Monakhov, E. V., Ye, J. D., Parkinson, P., Jagadish, C., Svensson, B. G., and Wong-Leung, J. Defect formation and thermal stability of H in high dose H implanted ZnO. *Journal of Applied Physics*, 114(8):083111, 2013.
- [92] Zhang, Z., Look, D. C., Schifano, R., Johansen, K. M., Svensson, B. G., and Brillson, L. J. Process dependence of H passivation and doping in H-implanted ZnO. *Journal of Physics D: Applied Physics*, 46(5):055107, 2013.
- [93] Strzhemechny, Y. M., Nemergut, J., Smith, P. F., Bae, J., Look, D. C., and Brillson, L. J. Remote hydrogen plasma processing of ZnO single crystal surfaces. *J. Appl. Phys.*, 94(7):4256, 2003.
- [94] Van de Walle, C. G., Neugebauer, J., and de Walle, C. V. Universal alignment of hydrogen levels in semiconductors, insulators and solutions. *Nature*, 423(June):626–628, 2003.
- [95] Strzhemechny, Y. M., Mosbacher, H. L., Look, D. C., Reynolds, D. C., Litton, C. W., Garces, N. Y., Giles, N. C., Halliburton, L. E., Niki, S., and Brillson, L. J. Remote hydrogen plasma doping of single crystal ZnO. *Appl. Phys. Lett.*, 84(14):2545–2547, 2004.

- [96] Zhou, Z., Kato, K., Komaki, T., Yoshino, M., Yukawa, H., Morinaga, M., and Morita, K. Effects of dopants and hydrogen on the electrical conductivity of ZnO. *Journal of the European Ceramic Society*, 24(1):139–146, 2004.
- [97] McCluskey, M. D., Jokela, S. J., Zhuravlev, K. K., Simpson, P. J., and Lynn, K. G. Infrared spectroscopy of hydrogen in ZnO. *Applied Physics Letters*, 81(20):3807, 2002.
- [98] Shi, G. A., Stavola, M., Pearton, S. J., Thieme, M., Lavrov, E. V., and Weber, J. Hydrogen local modes and shallow donors in ZnO. *Phys. Rev. B*, 72(19):195211, 2005.
- [99] Lavrov, E. V., Weber, J., Börrnert, F., Van De Walle, C., and Helbig, R. Hydrogen-related defects in ZnO studied by infrared absorption spectroscopy. *Phys. Rev. B*, 66(16):165205, 2002.
- [100] Dangbégnon, J. K., Talla, K., and Botha, J. R. Effect of annealing and hydrogen plasma treatment on the luminescence of hydrothermally grown bulk ZnO. *Optical Materials*, 34(5):920–925, 2012.
- [101] Dev, A., Niepelt, R., Richters, J. P., Ronning, C., and Voss, T. Stable enhancement of near-band-edge emission of ZnO nanowires by hydrogen incorporation. *Nanotechnology*, 21(6):065709, 2010.
- [102] McCluskey, M. D. and Jokela, S. J. Defects in ZnO. *J. Appl. Phys.*, 106(7):071101, 2009.
- [103] Jokela, S. and McCluskey, M. Structure and stability of O-H donors in ZnO from high-pressure and infrared spectroscopy. *Physical Review B*, 72(11):113201, 2005.
- [104] Shimomura, K., Nishiyama, K., and Kadono, R. Electronic Structure of the Muonium Center as a Shallow Donor in ZnO. *Physical Review Letters*, 89(25):255505, 2002.
- [105] Bang, J. and Chang, K. J. Atomic Structure and Diffusion of Hydrogen in ZnO. *Journal of the Korean Physical Society*, 55(1):98–102, 2009.
- [106] Wardle, M., Goss, J., and Briddon, P. First-Principles Study of the Diffusion of Hydrogen in ZnO. *Physical Review Letters*, 96(20):205504, 2006.
- [107] Cai, P. F., You, J. B., Zhang, X. W., Dong, J. J., Yang, X. L., Yin, Z. G., and Chen, N. F. Enhancement of conductivity and transmittance of ZnO films by post hydrogen plasma treatment. *J. Appl. Phys.*, 105(8):83713, 2009.

- [108] Seager, C. H. and Myers, S. M. Quantitative comparisons of dissolved hydrogen density and the electrical and optical properties of ZnO. *Journal of Applied Physics*, 94(5):2888, 2003.
- [109] Ohashi, N., Ishigaki, T., Okada, N., Sekiguchi, T., Sakaguchi, I., and Haneda, H. Effect of hydrogen doping on ultraviolet emission spectra of various types of ZnO. *Appl. Phys. Lett.*, 80(16):2869, 2002.
- [110] Kanaya, K. and Okayama, S. Penetration and energy-loss theory of electrons in solid targets. *Journal of Physics D: Applied Physics*, 43(1):43, 1972.
- [111] Drouin, D., Couture, A. R., Joly, D., Tastet, X., Aimez, V., and Gauvin, R. CASINO V2.42: a fast and easy-to-use modeling tool for scanning electron microscopy and microanalysis users. *Scanning*, 29(3):92–101, 2007.
- [112] van der Pauw, L. J. A Method of Measuring Specific Resistivity and Hall Effect of Discs of Arbitrary Shapes. *Philips Research Reports*, 13:1–9, 1958.
- [113] Cowie, B. C. C., Tadich, A., Thomsen, L., Garrett, R., Gentle, I., Nugent, K., and Wilkins, S. The Current Performance of the Wide Range (90-2500 eV) Soft X-ray Beamline at the Australian Synchrotron. *AIP Conference Proceedings*, 1234(1):307–310, 2010.
- [114] Sincrotrone Trieste SCpA. Atomic Calculation of Photoionization Cross-Sections and Asymmetry Parameters, 2013. URL <http://ulisse.elettra.trieste.it/services/elements/WebElements.html>.
- [115] Loudon, R. The Raman effect in crystals. *Advances in Physics*, 13(52):423–482, 1964.
- [116] Cuscó, R., Alarcón-Lladó, E., Ibáñez, J., Artús, L., Jiménez, J., Wang, B., and Callahan, M. Temperature dependence of Raman scattering in ZnO. *Physical Review B*, 75(16):165202, 2007.
- [117] Klingshirn, C. C. F. and Waag, A. *Zinc Oxide: From Fundamental Properties Towards Novel Applications*. Springer Series in Materials Science, 120. Springer Berlin Heidelberg, 2010. ISBN 9783642105777.
- [118] Arora, B. M., Chakravarty, S., Subramanian, S., Polyakov, V. I., Ermakov, M. G., Ermakova, O. N., and Perov, P. I. Deep-level transient charge spectroscopy of Sn donors in Al_xGa_{1-x}As. *Journal of Applied Physics*, 73(4):1802, 1993.
- [119] Lang, D. V. Deep-level transient spectroscopy: A new method to characterize traps in semiconductors. *Journal of Applied Physics*, 45(7):3023, 1974.

- [120] Thurzo, I., Beyer, R., and Zahn, D. R. T. Experimental evidence for complementary spatial sensitivities of capacitance and charge deep-level transient spectroscopies. *Semiconductor Science and Technology*, 15(4):378–385, 2000.
- [121] Fukumasa, O., Italani, R., and Saeki, S. Numerical simulation of hydrogen ion species in the steady-state plasma of a low-pressure ion source. *Journal of Physics D: Applied Physics*, 18(12):2433–2449, 1985.
- [122] Lide, D. R. *CRC Handbook of Chemistry and Physics*. CRC Press, 72 edition, 1991.
- [123] Ip, K., Overberg, M. E., Heo, Y. W., Norton, D. P., Pearton, S. J., Stutz, C. E., Kucheyev, S. O., Jagadish, C., Williams, J. S., Luo, B., Ren, F., Look, D. C., and Zavada, J. M. Hydrogen incorporation, diffusivity and evolution in bulk ZnO. *Solid-State Electronics*, 47(12):2255–2259, 2003.
- [124] Lavrov, E. V., Börrnert, F., and Weber, J. Hydrogen motion in ZnO. *Physica B: Condensed Matter*, 401-402:366–369, 2007.
- [125] Nickel, N. Hydrogen migration in single crystal and polycrystalline zinc oxide. *Phys. Rev. B*, 73(19):195204, 2006.
- [126] Park, Y. R., Kim, J., and Kim, Y. S. Effect of hydrogen doping in ZnO thin films by pulsed DC magnetron sputtering. *Applied Surface Science*, 255(22):9010–9014, 2009.
- [127] Groenen, R., Creatore, M., and Sanden, M. V. D. Dry etching of surface textured zinc oxide using a remote argonhydrogen plasma. *Applied Surface Science*, 241(3-4):321–325, 2005.
- [128] Look, D. C. Model for thickness dependence of mobility and concentration in highly conductive zinc oxide. *Optical Engineering*, 52(3):033801, 2013.
- [129] Look, D. C., Claffin, B., and Smith, H. E. Origin of conductive surface layer in annealed ZnO. *Applied Physics Letters*, 92(12):122108, 2008.
- [130] Look, D., Mosbacher, H., Strzhemechny, Y., and Brillson, L. Effects of surface conduction on Hall-effect measurements in ZnO. *Superlattices and Microstructures*, 38(4-6):406–412, 2005.
- [131] Reynolds, D., Look, D., Jogai, B., Jones, R., Litton, C., Harsch, W., and Cantwell, G. Optical properties of ZnO crystals containing internal strains. *Journal of Luminescence*, 82(2):173–176, 1999.
- [132] Morkoc, H. and Özgür, U. *Zinc Oxide: Fundamentals, Materials and Device Technology*. Wiley, 2008. ISBN 9783527623952.

- [133] Garces, N. Y., Wang, L., Bai, L., Giles, N. C., Halliburton, L. E., and Cantwell, G. Role of copper in the green luminescence from ZnO crystals. *Appl. Phys. Lett.*, 81(4):622, 2002.
- [134] Jaros, M. *Deep Levels in Semiconductors*. Taylor & Francis, 1st edition, 1982.
- [135] Klingshirn, C. ZnO: material, physics and applications. *ChemPhysChem*, 8(6):782–803, 2007.
- [136] Lander, J. J. Reactions of Lithium as a donor and an acceptor in ZnO. *Journal of Physics and Chemistry of Solids*, 1(4):324–334, 1960.
- [137] Wagner, M., Callsen, G., Reparaz, J., Schulze, J.-H., Kirste, R., Cobet, M., Ostapenko, I., Rodt, S., Nenstiel, C., Kaiser, M., Hoffmann, A., Rodina, A., Phillips, M., Lautenschläger, S., Eisermann, S., and Meyer, B. Bound excitons in ZnO: Structural defect complexes versus shallow impurity centers. *Phys. Rev. B*, 84(3):035313, 2011.
- [138] Yacobi, B. G. and Holt, D. B. *Cathodoluminescence microscopy of inorganic solids*. Plenum Press, New York, 1990. ISBN 0306433141.
- [139] Hoffmann, A., Meyer, B. K., and Malguth, E. Deep Centres in ZnO. In *Zinc Oxide: From Fundamental Properties Towards Novel Applications*, volume 120 of *Springer Series in Materials Science*, pages 233–266. Springer Berlin Heidelberg, 2010. ISBN 978-3-642-10577-7.
- [140] Gelhausen, O., Phillips, M. R., and Toth, M. Depth-resolved cathodoluminescence microanalysis of near-edge emission in III-nitride thin films. *Journal of Applied Physics*, 89(6):3535, 2001.
- [141] Mass, J., Avella, M., Jiménez, J., Callahan, M., Grant, E., Rakes, K., Bliss, D., and Wang, B. Cathodoluminescence characterization of hydrothermal ZnO crystals. *Superlattices and Microstructures*, 38(4-6):223–230, 2005.
- [142] Du, M.-H. and Biswas, K. Anionic and Hidden Hydrogen in ZnO. *Physical Review Letters*, 106(11):1–4, 2011.
- [143] Wang, R., Xu, G., and Jin, P. Size dependence of electron-phonon coupling in ZnO nanowires. *Phys. Rev. B*, 69(11):5–8, 2004.
- [144] Arguello, C., Rousseau, D., and Porto, S. First-Order Raman Effect in Wurtzite-Type Crystals. *Physical Review*, 181(3):1351–1363, 1969.
- [145] Umar, a. and Hahn, Y. B. Aligned hexagonal coaxial-shaped ZnO nanocolumns on steel alloy by thermal evaporation. *Applied Physics Letters*, 88(17):173120, 2006.

- [146] Cao, B., Cai, W., Zeng, H., and Duan, G. Morphology evolution and photoluminescence properties of ZnO films electrochemically deposited on conductive glass substrates. *Journal of Applied Physics*, 99(7):073516, 2006.
- [147] Lavrov, E. V., Herklotz, F., and Weber, J. Identification of two hydrogen donors in ZnO. *Phys. Rev. B*, 79(16):165210, 2009.
- [148] Albrecht, a. C. On the Dependence of Vibrational Raman Intensity on the Wavelength of Incident Light. *The Journal of Chemical Physics*, 55(9):4438, 1971.
- [149] Jeanmaire, D. L. and Van Duyne, R. P. Surface raman spectroelectrochemistry. *Journal of Electroanalytical Chemistry and Interfacial Electrochemistry*, 84(1):1–20, 1977.
- [150] Weber, J., Lavrov, E. V., and Herklotz, F. Hydrogen shallow donors in ZnO and rutile TiO₂. *Physica B: Condensed Matter*, 407(10):1456–1461, 2012.
- [151] Wagner, C. D., Davis, L. E., Zeller, M. V., Taylor, J. A., Raymond, R. H., and Gale, L. H. Empirical atomic sensitivity factors for quantitative analysis by electron spectroscopy for chemical analysis. *Surface and Interface Analysis*, 3(5):211–225, 1981.
- [152] Hecht, E. and Zajac, A. *Optics*. Addison Wesley Publishing Company, 3rd editio edition, 1997.
- [153] Somorjai, G. A. and Li, Y. *Introduction to Surface Chemistry and Catalysis*. John Wiley & Sons, 2010. ISBN 9780470508237.
- [154] DelaRosa, E., Sepulveda-Guzman, S., Reeja-Jayan, B., Torres, A., Salas, P., Elizondo, N., and Yacaman, M. Controlling the Growth and Luminescence Properties of Well-Faceted ZnO Nanorods. *Journal of Physical Chemistry C*, 111(24):8489–8495, 2007.
- [155] Ramgir, N. S., Late, D. J., Bhise, A. B., More, M. a., Mulla, I. S., Joag, D. S., and Vijayamohanan, K. ZnO multipods, submicron wires, and spherical structures and their unique field emission behavior. *The journal of physical chemistry. B*, 110(37):18236–42, 2006.
- [156] Allen, M. W., Durbin, S. M., and Metson, J. B. Silver oxide Schottky contacts on n-type ZnO. *Applied Physics Letters*, 91(5):053512, 2007.
- [157] Bastin, D., Lavrov, E., and Weber, J. Metastable state of the V-_{Zn}H-₂ defect in ZnO. *Phys. Rev. B*, 83(19):1–5, 2011.

- [158] Chiou, J. W., Jan, J. C., Tsai, H. M., Bao, C. W., Pong, W. F., Tsai, M.-H., Hong, I.-H., Klauser, R., Lee, J. F., Wu, J. J., and Liu, S. C. Electronic structure of ZnO nanorods studied by angle-dependent x-ray absorption spectroscopy and scanning photoelectron microscopy. *Applied Physics Letters*, 84(18):3462, 2004.
- [159] Allen, M. W., Zemlyanov, D. Y., Waterhouse, G. I. N., Metson, J. B., Veal, T. D., McConville, C. F., and Durbin, S. M. Polarity effects in the x-ray photoemission of ZnO and other wurtzite semiconductors. *Applied Physics Letters*, 98(10):101906, 2011.
- [160] Center for X-Ray Optics. X-Ray Attenuation Length, 2010. URL http://henke.lbl.gov/optical_constants/atten2.html.
- [161] Henke, B., Gullikson, E., and Davis, J. X-Ray Interactions: Photoabsorption, Scattering, Transmission, and Reflection at $E = 50\text{--}30,000$ eV, $Z = 1\text{--}92$. *Atomic Data and Nuclear Data Tables*, 54(2):181–342, 1993.
- [162] Chen, J. G. Near-edge x-ray absorption fine structure characterization of compositions and reactivities of transition metal oxides. *Journal of Vacuum Science & Technology A: Vacuum, Surfaces, and Films*, 14(3):1668, 1996.
- [163] Chen, J. NEXAFS investigations of transition metal oxides, nitrides, carbides, sulfides and other interstitial compounds. *Surface Science Reports*, 30(1-3):1–152, 1997.
- [164] Guo, J., Vayssieres, L., Persson, C., Ahuja, R., and Johansson, B. Polarization-dependent soft-x-ray absorption of highly oriented ZnO microrod arrays. *Journal of Physics: Condensed Matter*, 14(28):6969–6974, 2002.
- [165] Endo, O., Nakamura, M., Sumii, R., and Amemiya, K. 1D Hydrogen Bond Chain on Pt(211) Stepped Surface Observed by O K-NEXAFS Spectroscopy. *The Journal of Physical Chemistry C*, 116(26):13980–13984, 2012.
- [166] Bergmann, U., Wernet, P., Glatzel, P., Cavalleri, M., Pettersson, L., Nilsson, a., and Cramer, S. X-ray Raman spectroscopy at the oxygen K edge of water and ice: Implications on local structure models. *Physical Review B*, 66(9):092107, 2002.
- [167] Parent, P., Laffon, C., Mangeney, C., Bournel, F., and Tronc, M. Structure of the water ice surface studied by x-ray absorption spectroscopy at the O K-edge. *The Journal of Chemical Physics*, 117(23):10842, 2002.
- [168] Grunes, L. L., Leapman, R., Wilker, C. C., Hoffmann, R., and Kunz, a. Oxygen K near-edge fine structure: An electron-energy-loss investigation with comparisons to new theory for selected 3d Transition-metal oxides. *Physical Review B*, 25(12):7157–7173, 1982.

- [169] Ton-That, C., Phillips, M. R., Foley, M., Moody, S. J., and Stampfl, A. P. J. Surface electronic properties of ZnO nanoparticles. *Applied Physics Letters*, 92(26):261916, 2008.
- [170] Krishnamurthy, S., McGuinness, C., Dorneles, L. S., Venkatesan, M., Coey, J. M. D., Lunney, J. G., Patterson, C. H., Smith, K. E., Learmonth, T., Glans, P. a., Schmitt, T., and Guo, J. H. Soft-x-ray spectroscopic investigation of ferromagnetic Co-doped ZnO. *Journal of Applied Physics*, 99(8):08M111, 2006.
- [171] Lagarde, P. Surface X-ray absorption spectroscopy principles and some examples of applications. *Ultramicroscopy*, 86(3-4):255–263, 2001.
- [172] Schröer, P., Krüger, P., and Pollmann, J. First-principles calculation of the electronic structure of the wurtzite semiconductors ZnO and ZnS. *Physical review. B, Condensed matter*, 47(12):6971–6980, 1993.
- [173] Ray, S. C., Low, Y., Tsai, H. M., Pao, C. W., Chiou, J. W., Yang, S. C., Chien, F. Z., Pong, W. F., Tsai, M.-H., Lin, K. F., Cheng, H. M., Hsieh, W. F., and Lee, J. F. Size dependence of the electronic structures and electron-phonon coupling in ZnO quantum dots. *Applied Physics Letters*, 91(26):262101, 2007.
- [174] Horwat, D., Jullien, M., Capon, F., Pierson, J.-F., Andersson, J., and Endrino, J. L. On the deactivation of the dopant and electronic structure in reactively sputtered transparent Al-doped ZnO thin films. *Journal of Physics D: Applied Physics*, 43(13):132003, 2010.
- [175] Mosquera, A. a., Horwat, D., Rashkovskiy, A., Kovalev, A., Miska, P., Wainstein, D., Albella, J. M., and Endrino, J. L. Exciton and core-level electron confinement effects in transparent ZnO thin films. *Scientific reports*, 3:1714, 2013.
- [176] Sturm, C., Hilmer, H., Schmidt-Grund, R., and Grundmann, M. Observation of strong excitonphoton coupling at temperatures up to 410K. *New Journal of Physics*, 11(7):073044, 2009.
- [177] Wang, L. and Giles, N. C. Temperature dependence of the free-exciton transition energy in zinc oxide by photoluminescence excitation spectroscopy. *Journal of Applied Physics*, 94(2):973, 2003.
- [178] Willardson, R. K. and Beer, A. C. *Semiconductors and Semimetals Volume 8: Transport and optical phenomena*. Academic Press, 1972.
- [179] Giles, N. C., Xu, C., Callahan, M. J., Wang, B., Neal, J. S., and Boatner, L. a. Effects of phonon coupling and free carriers on band-edge emission at room temperature in n-type ZnO crystals. *Applied Physics Letters*, 89(25):251906, 2006.

- [180] Chen, Y., Bagnall, D. M., Koh, H.-j., Park, K.-t., Hiraga, K., Zhu, Z., and Yao, T. Plasma assisted molecular beam epitaxy of ZnO on c-plane sapphire: Growth and characterization. *Journal of Applied Physics*, 84(7):3912, 1998.
- [181] Hamby, D. W. D., Lucca, D. a., Klopstein, M. J. M., and Cantwell, G. Temperature dependent exciton photoluminescence of bulk ZnO. *Journal of Applied Physics*, 93(6):3214, 2003.
- [182] Pankove, J. I. *Optical processes in semiconductors*. Dover Publications Inc, 1975.
- [183] Willardson, R. and Beer, A. C. *Semiconductors and Semimetals, Vol. 16: Defects, (HgCd) Se, (HgCd) Te*. Academic Press, 1981.
- [184] Bogardus, E. and Bebb, H. Bound-Exciton, Free-Exciton, Band-Acceptor, Donor-Acceptor, and Auger Recombination in GaAs. *Physical Review*, 176(3):993–1002, 1968.
- [185] Shibata, H. Negative Thermal Quenching Curves in Photoluminescence of Solids. *J. Appl. Phys.*, 37(Part 1, No. 2):550–553, 1998.
- [186] Watanabe, M., Sakai, M., Shibata, H., Satou, C., Satou, S., Shibayama, T., Tampo, H., Yamada, a., Matsubara, K., Sakurai, K., Ishizuka, S., Niki, S., Maeda, K., and Niikura, I. Negative thermal quenching of photoluminescence in ZnO. *Physica B: Condensed Matter*, 376-377:711–714, 2006.
- [187] Wu, K., He, H., Lu, Y., Huang, J., and Ye, Z. Negative thermal quenching of the 3.338eV emission in ZnO nanorods. *Solid State Communications*, 152(18):1757–1760, 2012.
- [188] Singh, A., Chaudhary, S., and Pandya, D. K. Hydrogen incorporation induced metal-semiconductor transition in ZnO:H thin films sputtered at room temperature. *Applied Physics Letters*, 102(17):172106, 2013.
- [189] Hauser, M., Hepting, A., Hauschild, R., Zhou, H., Fallert, J., Kalt, H., and Klingshirm, C. Absolute external luminescence quantum efficiency of zinc oxide. *Applied Physics Letters*, 92(21):211105, 2008.
- [190] Fang, Z.-Q., Claffin, B., Look, D. C., Dong, Y. F., Mosbacher, H. L., and Brillson, L. J. Surface traps in vapor-phase-grown bulk ZnO studied by deep level transient spectroscopy. *Journal of Applied Physics*, 104(6):063707, 2008.
- [191] Vines, L., Monakhov, E. V., Schifano, R., Mtangi, W., Auret, F. D., and Svensson, B. G. Lithium and electrical properties of ZnO. *J. Appl. Phys.*, 107(10):103707, 2010.

- [192] Alves, H., Pfisterer, D., Zeuner, a., Riemann, T., Christen, J., Hofmann, D., and Meyer, B. Optical investigations on excitons bound to impurities and dislocations in ZnO. *Optical Materials*, 23(1-2):33–37, 2003.
- [193] Look, D. C., Reynolds, D. C., Hemsley, J. W., Jones, R. L., and Sizelove, J. R. Production and annealing of electron irradiation damage in ZnO. *Applied Physics Letters*, 75(6):811, 1999.
- [194] Vechten, J. A. V. Handbook on Semiconductors Vol. 3: Materials and Preparation. North-Holland, 1980.
- [195] Braäunig, D. and Wulf, F. Atomic displacement and total ionizing dose damage in semiconductors. *Radiation Physics and Chemistry*, 43(1-2):105–127, 1994.
- [196] Serevičius, T., Miasojedovas, S., Gavryushin, V., and Jursėlnas, S. Luminescence of ZnO crystals under surface and bulk excitation regimes. *Physica Status Solidi (C)*, 6(12):2671–2673, 2009.
- [197] Djurišić, A. B., Leung, Y. H., Tam, K. H., Hsu, Y. F., Ding, L., Ge, W. K., Zhong, Y. C., Wong, K. S., Chan, W. K., Tam, H. L., Cheah, K. W., Kwok, W. M., Phillips, D. L., and Djuricic, A. B. Defect emissions in ZnO nanostructures. *Nanotechnology*, 18(9):95702, 2007.
- [198] van Dijken, A., Meulenkaamp, E. A., Vanmaekelbergh, D., and Meijerink, A. The Kinetics of the Radiative and Nonradiative Processes in Nanocrystalline ZnO Particles upon Photoexcitation. *The Journal of Physical Chemistry B*, 104(8):1715–1723, 2000.
- [199] Phillips, M. R., Telg, H., Kucheyev, S. O., Gelhausen, O., and Toth, M. Cathodoluminescence efficiency dependence on excitation density in n-type gallium nitride. *Microscopy and microanalysis : the official journal of Microscopy Society of America, Microbeam Analysis Society, Microscopical Society of Canada*, 9(2):144–51, 2003.
- [200] Kucheyev, S. O., Toth, M., Phillips, M. R., Williams, J. S., and Jagadish, C. Effects of excitation density on cathodoluminescence from GaN. *Appl. Phys. Lett.*, 79(14):2154, 2001.
- [201] Müllhäuser, J., Brandt, O., Yang, H., and Ploog, K. Exciton Luminescence of Single-Crystal GaN. *MRS Proceedings*, 395:607, 2011.
- [202] Singh, R., Molnar, R. J., Unlu, M. S., and Moustakas, T. D. Intensity dependence of photoluminescence in GaN thin films. *Applied Physics Letters*, 64(3):336, 1994.
- [203] Reshchikov, M. and Korotkov, R. Analysis of the temperature and excitation intensity dependencies of photoluminescence in undoped GaN films. *Physical Review B*, 64(11):115205, 2001.

- [204] Johansen, K., Zubiaga, A., Tuomisto, F., Monakhov, E., Kuznetsov, a. Y., and Svensson, B. H passivation of Li on Zn-site in ZnO: Positron annihilation spectroscopy and secondary ion mass spectrometry. *Phys. Rev. B*, 84(11):115203, 2011.
- [205] Halliburton, L. E., Wang, L., Bai, L., Garces, N. Y., Giles, N. C., Callahan, M. J., and Wang, B. Infrared absorption from OH⁺ ions adjacent to lithium acceptors in hydrothermally grown ZnO. *Journal of Applied Physics*, 96(12):7168, 2004.
- [206] Shi, G., Stavola, M., and Fowler, W. Identification of an OH-Li center in ZnO: Infrared absorption spectroscopy and density functional theory. *Physical Review B*, 73(8):081201, 2006.
- [207] Manasreh, M. O. and Fischer, D. W. Infrared absorption of electron irradiation induced deep defects in semi-insulating GaAs. *Applied Physics Letters*, 53(24):2429, 1988.
- [208] Reshchikov, M., Shahedipour, F., Korotkov, R., Ulmer, M., and Wessels, B. Deep acceptors in undoped GaN. *Physica B: Condensed Matter*, 273-274: 105–108, 1999.
- [209] Bhattacharya, P., Mahajan, S., and Kamimura, H. *Comprehensive Semiconductor Science and Technology: Online version*. Comprehensive semiconductor science and technology. Elsevier Science, 2011. ISBN 9780080932286.
- [210] Carvalho, A., Alkauskas, A., Pasquarello, A., Tagantsev, A. K., and Setter, N. A hybrid density functional study of lithium in ZnO: Stability, ionization levels, and diffusion. *Phys. Rev. B*, 80(19):195205, 2009.
- [211] Johansen, K. M., Haug, H., Lund, E., Monakhov, E. V., and Svensson, B. G. Thermal stability of the OHLi complex in hydrothermally grown single crystalline ZnO. *Appl. Phys. Lett.*, 97(21):211907, 2010.
- [212] Gelhausen, O., Phillips, M., Goldys, E., Paskova, T., Monemar, B., Strassburg, M., and Hoffmann, a. Dissociation of H-related defect complexes in Mg-doped GaN. *Physical Review B*, 69(12):125210, 2004.
- [213] Weston, L., Ton-That, C., and Phillips, M. Doping properties of hydrogen in ZnO. *Journal of Materials Research*, 27(17):2220–2224, 2012.
- [214] Cazaux, J. e-Induced secondary electron emission yield of insulators and charging effects. *Nuclear Instruments and Methods in Physics Research Section B: Beam Interactions with Materials and Atoms*, 244(2):307–322, 2006.

-
- [215] Phillips, M. R., Gelhausen, O., and Goldys, E. M. Cathodoluminescence properties of zinc oxide nanoparticles. *Physica Status Solidi (a)*, 201(2): 229–234, 2004.